Doctoral Thesis ETH No. 16289

The PILATUS 1M Detector
A Novel Large Area Pixel Detector

A dissertation submitted to the

SWISS FEDERAL INSTITUTE OF TECHNOLOGY ZURICH

for the degree of

DOCTORAL OF NATURAL SCIENCES

presented by

Gregor Hülsen–Bollier

Diplom Physik, University of Erlangen–Nürnberg

born April 16th, 1971

citizen of Germany

accepted on the recommendation of

Prof. Dr. Ralph A. Eichler, examiner

Prof. Dr. Fritz K. Winkler, second examiner

Dr. Roland Horisberger, third examiner

PSI, Villigen, 2005

Contents

1 Summary **1**
- 1.1 Summary . . . 1
- 1.2 Zusammenfassung . . . 3

2 Introduction **5**
- 2.1 Introduction to Protein Crystallography . . . 6
- 2.2 The Ideal Detector . . . 15
- 2.3 CCDs and Hybrid Pixel Area Detectors . . . 16
  - 2.3.1 Large Area CCD Detectors . . . 17
  - 2.3.2 Hybrid Pixel Array Detectors . . . 21
  - 2.3.3 Performance of CCDs and PADs . . . 31

3 The PILATUS 1M Detector **35**
- 3.1 The PILATUS 1M Detector and its Building Blocks . . . 35
  - 3.1.1 Sensor . . . 36
  - 3.1.2 Bump Bonding . . . 36
  - 3.1.3 CMOS Chip . . . 36
  - 3.1.4 Radiation Tolerance, Chip Technology and Defects . . . 39
  - 3.1.5 Detector Assembly . . . 41
- 3.2 Detector Control . . . 44
  - 3.2.1 Read–out Sequence . . . 44
  - 3.2.2 Hardware . . . 44
  - 3.2.3 Software . . . 46

4 Calibration of the PILATUS 1M Detector **49**
- 4.1 Threshold Equalization Procedure . . . 49
- 4.2 Flatfield Calibration . . . 51
  - 4.2.1 Experiment . . . 51
  - 4.2.2 Calculation . . . 52
  - 4.2.3 Results . . . 54
- 4.3 Distortion Calibration of the PILATUS 1M Detector . . . 57

5 Detector Performance **59**
- 5.1 Counting Statistics of Flatfield Images . . . 59
  - 5.1.1 Theoretical Counting Statistics for an Ideal Detector . . . 59

5.1.2 Statistics of Flatfield Measurements with the PILATUS 1M Detector . . 60
5.2 Defect Reduction 62
5.2.1 Permanent Dead Pixels 62
5.2.2 Counting Errors 62
5.2.3 Results 63
5.3 Protein Crystallography with the PILATUS 1M Detector 67

6 Discussion **69**

A Variance of Convoluted Probabilities **73**

B Abbreviations **75**

C List of Symbols **77**

Bibliography **79**

List of Images **83**

List of Tables **85**

Curriculum Vitae and List of Publications **87**

Acknowledgments **89**

Chapter 1

Summary

1.1 Summary

For the Protein Crystallography beamline X06SA of the Swiss Light Source a new X–ray detector was developed, the PILATUS 1M detector. The goal of this thesis was to participate to its fabrication, to calibrate the detector and to investigate its performance in protein crystallographic data collection.

The PILATUS 1M detector is the largest hybrid X–ray pixel detector currently in use at a synchrotron. It is a modular system consisting of 18 multi–chip modules covering a total area of 243×210 mm^2. This prototype consists of one million pixels with a size of 217×217 μm^2. The silicon sensors have a thickness of 300 μm. The readout electronics, with an amplifier, a comparator and a digital counter in each pixel, enables single photon counting. All modules are read out in parallel, leading to a full frame readout time of 5.9 ms.

The first step of the detector calibration was to equalize the thresholds of all pixels. The threshold distribution of the detector is 42 electrons. The individual pixel response to X–rays was adjusted by a flatfield calibration. An algorithm for distortion correction of CCD detector data was adapted to correct the data of the PILATUS 1M detector. Images from this detector are spatially distorted by the influence of three factors. First, the absorption properties of the silicon lead to parallax broadening by a fraction of a pixel. Second, the modular architecture causes a mechanical displacement of the modules from their assumed positions. To reduce the dead area, the modules are tilted by 6° with respect to the mounting frame and are overlapping each other. A third correction step accounts for this tilt and projects the data onto a virtual plane.

The prototype detector suffered from a high number of non–responding or unreliable counting pixels within the active area. Therefore, defect reducing procedures were developed to compensate for these pixel defects. With their use protein crystallographic experiments could be performed. Conventional coarse ϕ–sliced datasets were recorded at the protein crystallography beamline X06SA of the Swiss Light Source. The data were processed and an electron density map was calculated. The results were compared with the performance of a reference CCD detector: the pixel detector is superior in speed but showed higher reliability–factors because of a flaw in the X–ray counter. Due to the short readout time and the noise–free readout, fine ϕ–sliced datasets could be recorded in continuous data collection mode. With the analysis of these data, the theoretically predicted advantages of this technique could be verified.

By eliminating the defects of this prototype detector a significant increase in data qual-

ity is expected for macromolecular crystallography experiments. Small anomalous intensity differences, important for phasing in multiple- or single–wavelength anomalous diffraction experiments, will be measured with higher accuracy. Therefore more protein structures than today could be solved using a hybrid pixel detector for these types of experiments.

1.2 Zusammenfassung

Für die Protein–Kristallographie Strahllinie X06SA der Synchrotron Lichtquelle Schweiz wurde ein neuer Röntgen Detektor entwickelt, der PILATUS 1M Detektor. Die Zielsetzung dieser Dissertation war die Mitwirkung in der Fabrikation, die Kalibrierung des Detektors und die Untersuchung seiner Funktionalität mit kristallographischen Experimenten.

Der PILATUS 1M Detektor ist der grösste Hybrid Pixel Detektor der zur Zeit an einem Synchrotron eingesetzt wird. Dieses modulare System mit 18 Modulen, die wiederum aus mehreren Chips bestehen, bedeckt eine Fläche von 243×200 mm^2. Der Prototyp besteht aus einer Matrix von mehr als 10^6 Bildpunkten (Pixel) die eine Grösse von 217×217 μm^2 haben. Die Silizium Sensoren habe eine Dicke von 300 μm. Die Ausleseelektronik mit einem Verstärker, einem Komparator und einem digitalem Zähler in jedem Pixel erlaubt es einzelne Photonen zu zählen. Alle Module werden gleichzeitig ausgelesen, was zu einer Auslesezeit von 5.9 ms für ein Bild führt.

Der erste Schritt bei der Kalibration des Detektors besteht darin, die Schwellen von allen Pixeln auf einen einheitlichen Wert abzugleichen. Die Schwellenverteilung des Detektors ist 42 Elektronen. Die individuelle Reaktion jedes Pixels auf Röntgen Photonen wurde durch eine Flatfield–Kalibration ausgeglichen. Ein Algorithmus für die Verzerrungskorrektur von CCD Detektoren wurde angepasst, um die Daten des PILATUS 1M Detektors korrigieren zu können. Die Bilder des Detektors sind durch den Einfluss von drei Faktoren verzerrt. Erstens führen die Absorptionseigenschaften von Silizium zu einem Parallaxefehler von einem Bruchteil eines Pixels. Zweitens verursacht die modulare Architektur Ungenauigkeiten in der Positionierung der einzelnen Module. Die Module sind um 6° verkippt und überlappen sich, um die tote Fläche zwischen ihnen zu reduzieren. Eine dritter Korrekturschritt berücksichtigt diese Architektur und projiziert die Daten auf eine virtuelle Fläche.

Der Prototyp–Detektor leidet unter einer relativ grossen Zahl von toten oder unzuverlässig zählenden Pixeln. Es wurden zwei Verfahren entwickelt, um diese Anzahl an defekten Pixeln zu reduzieren. Durch ihre Anwendung konnten Protein–Kristallographische Experimente durchgeführt werden. Konventionelle Datensätze wurden an der Protein Kristallographie Strahllinie X06SA an der Synchrotron Lichtquelle Schweiz aufgenommen. Die Daten wurden ausgewertet und eine Elektronendichteverteilung errechnet. Die Ergebnisse wurden mit der Leistung eines CCD Detektors verglichen: Der Pixel Detektor ist bezüglich der Auslesegeschwindigkeit überlegen weist aber wegen eines Fehlers des digitalen Zählers höhere Zuverlässigkeits–Faktoren (R–Faktoren) auf. Auf Grund der schnellen Auslesezeit und der rauschfreien Auslese konnten Datensätze mit höherer ϕ–Auflösung in einem kontinuierlichem Datenerfassungs–Modus aufgenommen werden. Mit der Analyse der Daten konnten die theoretisch vorhergesagten Vorteile dieser Technik verifiziert werden.

Eine deutliche Verbesserung der Datenqualität in Protein kristallographischen Experimenten ist zu erwarten, wenn die Defekte dieses Prototyp Detektors behoben sind. Kleine anomale Intensitätsdifferenzen, die wichtig bei der Phasierung in MAD (multiple-wavelength anomalous Dispersion) oder SAD (single–wavelength anomalous Dispersion) Experimenten sind, werden dann mit einer höheren Genauigkeit gemessen. Durch den Einsatz eines Hybrid Pixel Detektors in diesen Experimenten könnten deshalb mehr Proteinstrukturen als bisher gelöst werden.

Seite Leer /
Blank leaf

Chapter 2

Introduction

One of the most outstanding projects in biology was to resolve the code of the human DNA. This project could be successfully finished in the year 2003. The DNA code defines the primary structure of proteins — the sequences of the amino acid chains. This chain is the backbone of a protein and coils up in a unique three dimensional structure, which is defined by the amino acid chain and the environmental conditions around the protein [1].

The properties of proteins — defining their special functionality — are ruled by the three dimensional structure. The main technique to resolve this three dimensional structure down to atomic resolution is X–ray crystallography. By using this technique the structures of thousands of proteins, viruses and nucleic acids have been solved [2]. The importance of X–ray crystallography cannot be underestimated. The knowledge of the three dimensional structure is of great importance for the design of drugs in pharmaceutical medicine. A prominent example is the small HIV–1 protease. Its function is to cut the HIV polyprotein into individual proteins to form the mature virus, which can then infect a new cell. The structure of this protein was solved within one year [3, 4]. Small molecule inhibitors have been designed to bind tightly to the protease. The HIV virus is destroyed because it is unable to mature into its infectious form.

A practical protein crystallographic experiment consists of an X–ray source, a protein crystal and an imaging detector. The X–ray source has developed from small laboratory X–ray tubes to large synchrotrons during the last five decades. The brilliance of X–ray sources has been increased by several orders of magnitude. The growth of protein crystals for X–ray experiments is still a challenging task in biochemistry. Modern X–ray detectors fit most of the requirements for protein crystallography. Image plate scanners are currently the most widely used detectors because of their large size, high sensitivity and high dynamic range [5]. At high intensity synchrotron facilities large area charge–coupled device X–ray detectors (hereafter called CCDs) are more popular in view of their faster read–out times. Still, these detectors do not take full advantage of the brilliance of 3^{rd} generation synchrotrons. Furthermore detector noise is always added to the data.

In parallel with the design of the Protein Crystallography beamline X06SA of the Swiss Light Source (SLS) the building blocks for an X–ray pixel detector were developed. The construction of the first large area hybrid pixel detector, the PILATUS 1M detector, was finished in fall 2003. Since then the detector was calibrated and its performance was investigated. 'PILATUS 1M' is an acronym for 'Pixel Apparatus for the Swiss Light Source, 1 million pixels'. The name is taken from Mt. Pilatus, located in central Switzerland.

This detector was especially designed for protein crystallography experiments at the SLS at the Paul Scherrer Institute (PSI) in Villigen, Switzerland. The task was to overcome the limitations of currently available detectors: the demand for faster, higher quality detectors is increasing with the availability of high brilliance synchrotrons. Macromolecular beamlines of these facilities are overbooked by several times because of the rising number of experiments done both in fundamental science and in pharmaceutical industry. In fundamental science the functionality of important proteins is investigated. Industrial research deals mainly with proteins which are potential targets for drugs.

The fundamental developments of the new detector generation lie in the domain of High Energy Physics. For the Large Hadron Collider (LHC) at CERN[1] two detectors are being built [6, 7]. The central parts of these detectors are two dimensional hybrid pixel detectors which have to track the paths of millions of particles per second. One of these central detectors for the Compact Muon Solenoid (CMS) detector is currently in development at PSI. Therefore both the know–how and the technological means needed to build these types of detectors are available at PSI, which enabled the construction of the PILATUS 1M detector as a spin off project of the international CMS project.

2.1 Introduction to Protein Crystallography

Protein X–ray crystallography is an imaging method that can resolve the three dimensional structure of molecules down to atomic resolution [8]. An example is the protein thaumatin shown in Figure 2.1. The size of macromolecules can be very large. For example, the structure of the rhinovirus, the causative agent of the common cold, has been solved. This virus has a molecular weight of $8.5 \cdot 10^6$ Daltons[2] [9–11]. Since the first protein structure solved with X–ray crystallography (myoglobin, 1958) the instrumentation and computer methods of structure determination and refinement have been continually improved. Today the structure determination from well diffracting crystals can be done routinely.

The principle of structure determination is shown in Figure 2.2a. An object scatters light, which represents a transformation from the *real space* into the so called *reciprocal space*. An objective lens can perform a back–transformation and by an eyepiece lens the observer sees a virtually magnified image of the object. The resolution of a microscope is limited by the wavelength of the used light. Visible light has a wavelength of 4000 to 7000 Å. For resolving the structure down to atomic precision (1 Å) X–ray light with a wavelength of 0.1 to 100 Å is needed.

The refractive index for lenses depends on the wavelength and, as there are no effective lenses for X–rays, the indirect method shown in Figure 2.2b is used. With a calculated back-transformation from the diffraction pattern, a real space image of the object is obtained.

In a crystal the atoms are well ordered in a crystal lattice (Fig. 2.3). The lattice is a regular repetition of a fundamental unit cell which consists of one or more macromolecules. Every unit

[1] Conseil Européen pour la Recherche Nucléaire (European Organization for Nuclear Research), Geneva, Switzerland

[2] The unit Dalton is the immediate predecessor of the atomic mass unit u ($1\ u \approx 1.66053886 \cdot 10^{-27}$kg) which is defined as 1/12 of the mass of an atom of ^{12}C.

Figure 2.1: The three dimensional structure of the protein thaumatin. The thin lines show the bonds between the individual atoms and the thick line follows the amino acid chain backbone schematically. This protein is used in food industry (sweetener) and in pharmaceutical industry (taste masker) because it is rated as being 2000 to 10000 times sweeter than sucrose.

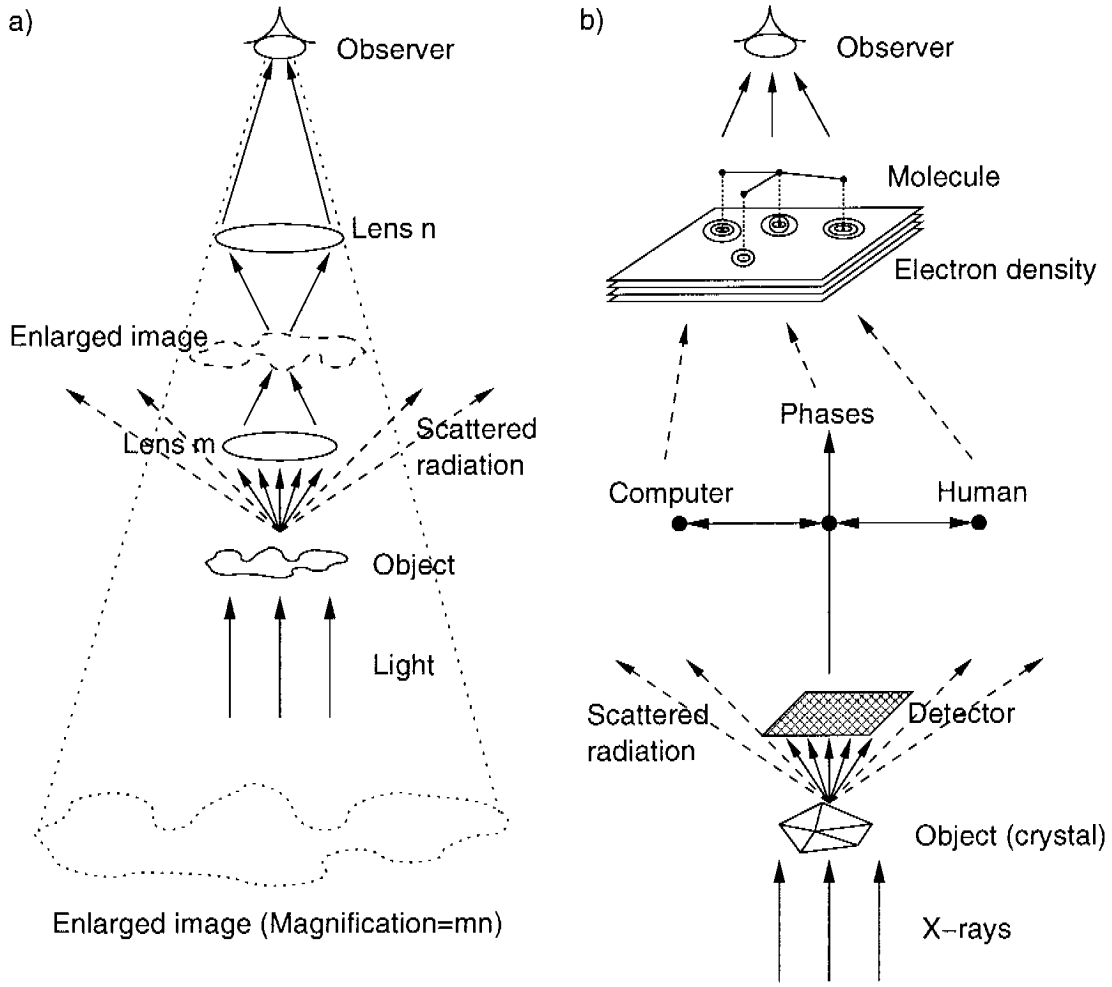

Figure 2.2: Light Microscope and X–ray crystallography. a) Scattered visible light of an object is magnified by two lenses with magnification m and n. The observer can view the enlarged image with magnification mn. b) Scattered X–rays of the electrons around atoms in a protein crystal are not reassembled by a lens but directly imaged by a detector. With the help of computers the crystallographer can calculate the positions of the atoms in the protein (Fourier synthesis), represented by regions of high electron density.

cell can be reached by a vector $\vec{R}_n$, which is defined as

$$\vec{R}_n = n_1\vec{a}_1 + n_2\vec{a}_2 + n_3\vec{a}_3 \ , \tag{2.1}$$

where $\vec{a}_1$, $\vec{a}_2$ and $\vec{a}_3$ are the lattice vectors, and n_1, n_2 and n_3 are integer numbers. A lattice has a characteristic symmetry which is defined by symmetry operators and can be assigned to one of seven *crystal systems*. The position of lattice points of the unit cell define 14 possible space lattices (*Bravais lattices*), which were first listed by A. Bravais in 1850. Combinations of simple rotation or inversion axes lead to 32 *point groups* which are compatible with the periodic nature of a crystal. The combination of the 14 Bravais lattices and the 32 point groups define 73 *space groups*. By considering screw axes and mirror planes as additional symmetry operators one obtains the 230 possible space groups, derived by mathematicians Fedorov (1890) and Schoenflies (1891) [12, 13]. Within a lattice, families of planes with a regular spacing d can be defined by the Miller indices (h, k, l). The plane closest to the origin intersects with the lattice axes $(\vec{a}_1, \vec{a}_2, \vec{a}_3)$ at $(\vec{a}_1/h, \vec{a}_2/k, \vec{a}_3/l)$.

A qualitative method for obtaining the condition and direction for diffraction from a crystal was introduced by W.L. Bragg. The incident wavevector $\vec{k}$ diffracts at crystal planes of one family, shown in Figure 2.4. The scattering angle θ leads to a difference in 'path' between the waves scattered in D and B. From the Figure it can be derived that this difference is equal to $AB + BC = 2d\sin\theta$. The two waves combine themselves with positive interference if the path difference is a multiple of the wavelength λ, which gives the Bragg equation

$$2d\sin\theta = n\lambda \ . \tag{2.2}$$

For $n = 1, 2, ...$ one obtains reflections with indices (h, k, l) of first order second order, etc. The beam is diffracted by the angle of 2θ (Fig. 2.4). Equation 2.2 can be simplified to

$$2\frac{d}{n}\sin\theta = 2d'\sin\theta = \lambda \ , \tag{2.3}$$

where d' can be interpreted as interplanar spacing of a lattice plane family with indices $(h' = nh, k' = nk, l' = nl)$. The maximum resolution obtained in a diffraction experiment can be derived by rewriting equation 2.3 to

$$d' = \frac{\lambda}{2\sin\theta} \ . \tag{2.4}$$

To resolve small structures, which is equivalent to recording reflections diffracted from planes with small interplanar spacing, a small wavelength is required and a large angular range must be covered by a detector. Reflections belonging to the low resolution are diffracted close to the incident X–ray beam direction. To obtain atomic resolution of 1 Å one can use X–rays with $\lambda = 1$ Å and reflections must be recorded at $2\theta \leq 60°$ from the primary beam direction (Eq. 2.4: $\sin\theta = 0.5$ with $d = \lambda = 1$ Å).

Electromagnetic radiation with a wavelength λ stimulates the electrons of an atom to oscillate and re–emit photons in all directions. The incident radiation wavevector $\vec{k}$ has an amplitude $|\vec{k}| = 2\pi/\lambda$. Scattering of atoms is observed along the direction $\vec{k}'$ with a phase difference φ. For elastic scattering the amplitude of $|\vec{k}'|$ equals the amplitude of $|\vec{k}|$. The wavevector transfer $\vec{Q}$ is defined as

$$\vec{Q} = \vec{k}' - \vec{k} \ . \tag{2.5}$$

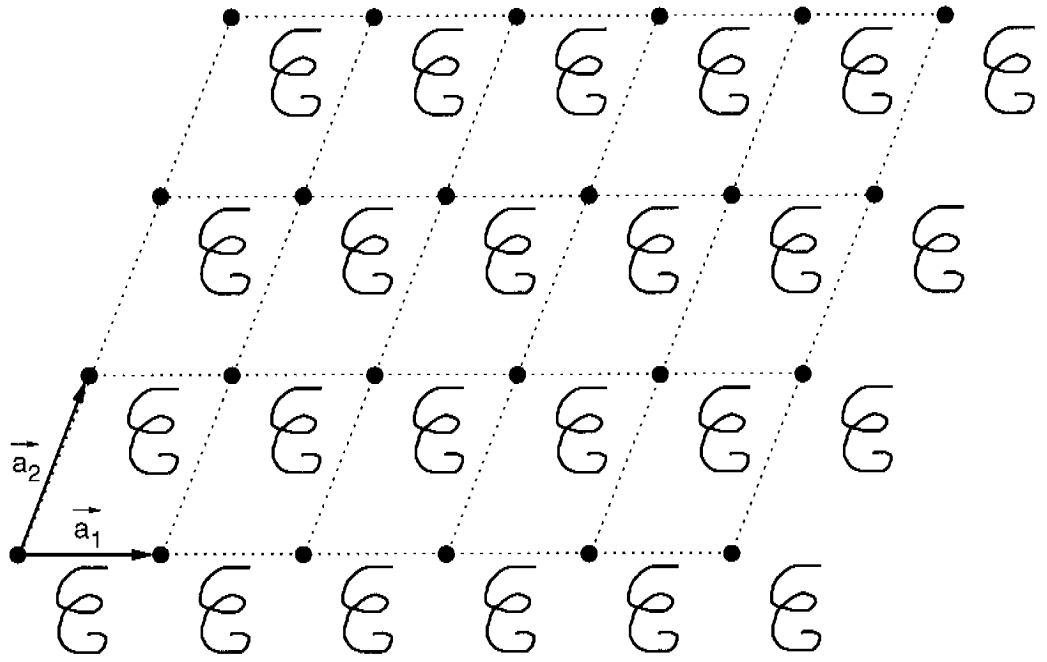

Figure 2.3: A protein crystal is formed by the fundamental unit cell which is repeated in a regular lattice. The fundamental unit cell is built by one or more macromolecules. The lattice (here shown only in two dimensions) is defined by the unit cell vectors $\vec{a}_1$ and $\vec{a}_2$.

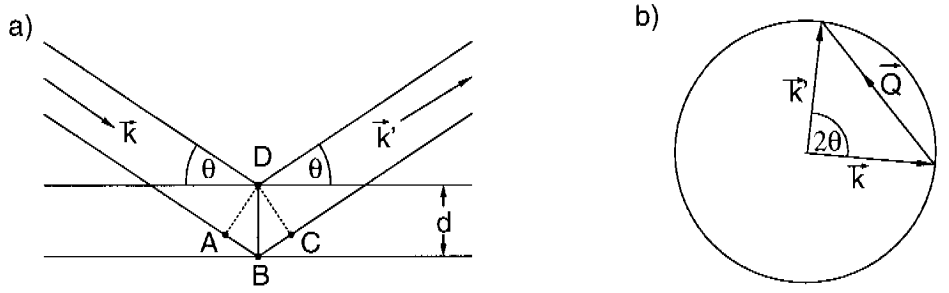

Figure 2.4: a) Reflection of an incident wave $\vec{k}$ from two lattice planes belonging to the family (h, k, l) with a interplanar spacing d. b) The scattered wavevector $\vec{k}'$ ends at a position on a circle with radius $|\vec{k}|$ depending on the scattering angle 2θ.

Figure 2.4 shows this scattering triangle; any wavevector $\vec{k}'$ terminates on a sphere of radius $|\vec{k}|$. The magnitude of the scattering vector $\vec{Q}$ is related to the scattering angle θ by

$$|\vec{Q}| = \left(\frac{4\pi}{\lambda}\right) \sin\theta \,. \tag{2.6}$$

Scattering of a molecule is the sum of scattering events of all atoms of this molecule in the unit cell. The distribution of electrons is described by the electron density of the unit cell $\rho_c(xyz)$. The periodic repetition of the lattice in one dimension can be translated to the electron density by $\rho_c(x) = \rho_c(x + n_1\vec{a}_1)$. All contributions of the lattice can be described as an expansion into a Fourier series

$$\rho(x) = \sum_n \rho_n e^{2\pi i(n_1/a_1)x} \,, \tag{2.7}$$

which is invariant against translation of a lattice vector $x_n = n_1\vec{a}_1$. The corresponding expansion in three dimensions is

$$\rho(\vec{r}) = \sum_{\vec{G}} \rho_{\vec{G}} e^{i\vec{G}\cdot\vec{r}} \,, \tag{2.8}$$

where the vector $\vec{G}$ has to meet the following conditions so that the invariance against translation symmetry of all lattice vectors $\vec{R}_n$ (Eq. 2.1) is fulfilled:

$$\vec{G}\cdot\vec{R}_n = 2\pi m \,, \tag{2.9}$$

with an integer number m for all values of n_1, n_2, n_3. The vector $\vec{G}$ can be factored, analogous to $\vec{R}_n$ (Eq. 2.1),

$$\vec{G}_{\mathrm{hkl}} = h\vec{a}_1^* + k\vec{a}_2^* + l\vec{a}_3^* \,, \tag{2.10}$$

with integer numbers h, k, l. The condition 2.9 defines the basis vectors $\vec{a}_1^*, \vec{a}_2^*, \vec{a}_3^*$ of the *reciprocal lattice* (Fig. 2.5a) which must fulfill $\vec{a}_i\vec{a}_j^* = 2\pi\delta_{ij}$[3]. The lattice points are described by the numbers h, k, l which are equivalent to the Miller indices defining the real lattice planes.

The amplitude of scattered waves is the integral over the scattering volume, i.e. all atoms in the crystal and can be written as

$$A \propto \int_S \rho(\vec{r}) e^{i\left(\vec{k}-\vec{k}'\right)\cdot\vec{r}} d^3r \,. \tag{2.11}$$

With the Fourier expansion for $\rho(\vec{r})$ (Eq. 2.8) and equation 2.5 we get

$$A \propto \int_S \sum_{\vec{G}} \rho_{\vec{G}} e^{i\vec{G}\cdot\vec{r}} e^{-i\vec{Q}\cdot\vec{r}} d^3r \tag{2.12}$$

$$\propto \sum_{\vec{G}} \rho_{\vec{G}} \int_S e^{i\left(\vec{G}-\vec{Q}\right)\cdot\vec{r}} d^3r \,. \tag{2.13}$$

[3]The Kronecker delta is defined so that $\delta_{ij} = 1$ if $i = j$ and is otherwise zero.

For crystals with many unit cells the integral is equal to zero for most scattering vectors $\vec{Q}$, but for $\vec{G} = \vec{Q}$ the integral is equal to the volume of the crystal. This is known as the *Laue condition*

$$\vec{Q} = \vec{G}. \tag{2.14}$$

Figure 2.5b visualizes the Laue condition by superposing the definition of the scattering vector $\vec{Q}$ (Fig. 2.4b) with the reciprocal lattice (Fig. 2.5a). Diffraction occurs if a reciprocal lattice point is on the so called Ewald sphere and the Figure illustrates that only few points fulfill the Laue condition. By rotating the crystal, which is identical to the rotation of the reciprocal lattice about the origin, other reciprocal lattice points cross the Ewald sphere. The limiting sphere, defined by the X–ray wavelength, surrounds all points where diffraction is possible.

The diffraction condition 2.14 defines where reflections occur. The intensity of a particular reflection (h, k, l) can be calculated from the *structure factor* [12]

$$F_{\mathrm{hkl}} = \sum_{j=1}^{N} f_j^{\mathrm{atom}}\left(\vec{Q}\right) e^{2\pi i(hx_j + ky_j + lz_j)} . \tag{2.15}$$

The sum is taken over the electrons of N atoms in the unit cell. Atom j is at position $\vec{R}_n + \vec{r}_j$, where $\vec{R}_n$ is the lattice vector and $\vec{r}_j$ is the position of the j'th atom in the unit cell. The electronic structure of this atom is described by the *atomic form factor* $f_j^{\mathrm{atom}}(\vec{Q})$. The magnitude of this factor is proportional to the number of electrons or the atomic number Z of an atom and depends on the magnitude of the scattering vector $\vec{Q}$ [12].

The unit cell structure factor is a complex number with amplitude $|F_{\mathrm{hkl}}|$ and a phase φ_{hkl}. In Figure 2.6 an example is drawn in the Gauss plane, showing how the amplitude and the phase are built up in a unit cell with five atoms: each atom j contributes to the sum of equation 2.15 with its atomic form factor f_j^{atom} and phase α_j to the resulting structure factor.

With the unit cell factors the electron density $\rho(xyz)$ at point xyz can be calculated by a Fourier transform:

$$\rho(xyz) = \frac{1}{V} \sum_h \sum_k \sum_l |F_{\mathrm{hkl}}| \cos[2\pi(hx + ky + lz) - \varphi_{\mathrm{hkl}}] . \tag{2.16}$$

The volume V of the unit cell is defined by the unit cell vectors $(\vec{a}_1, \vec{a}_2, \vec{a}_3)$.

Reflections by a crystal can be measured by placing a detector at the positions defined by the Ewald construction. The measured intensity is, in the kinematic approximation, proportional to $|F_{\mathrm{hkl}}|^2$. As the phases are not measured directly, several methods have been developed to obtain the phases of the structure factor [8, 12]. These methods rely on the fact that the atomic form factor (see above) depends on the number of electrons of the atom: heavy atoms scatter more strongly than small atoms. Mercury ($Z = 80$), for example, scatters 178 times better than carbon ($Z = 6$). The unit cell structure factor is thus influenced by the scattering of the heavy atom (Fig. 2.6). The most commonly used method is multiple isomorphous replacement (MIR) [8], where in addition to a 'native' measurement, data from at least two different 'heavy atom derivative' crystals are obtained. The intensity differences caused by the heavy atoms are used to determine the required phase information. Another approach is multiple wavelength anomalous dispersion (MAD) [8, 14] or single wavelength anomalous dispersion (SAD) [15]. Anomalous scattering of the heavy atoms, leads to a phase shift of the diffracted wave vector. This effect

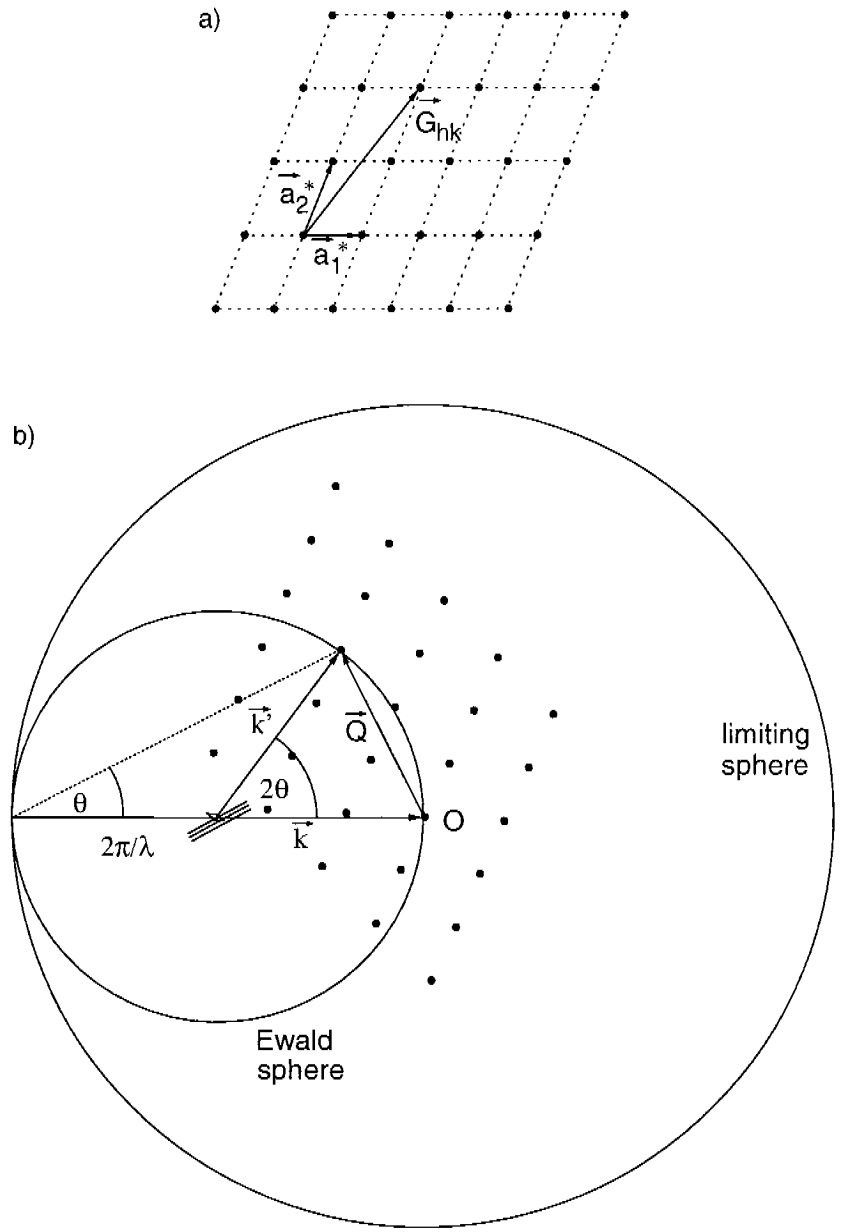

Figure 2.5: The reciprocal lattice and the Ewald sphere in 2 dimensions. a) The reciprocal lattice is defined by the reciprocal lattice vectors $(\vec{a}_1^*, \vec{a}_2^*)$. The point (h, k) can be reached by the vector $\vec{G}_{\rm hk}$. b) The incident wavevector $\vec{k}$ ends on the origin of the reciprocal lattice and defines the Ewald sphere. Scattering occurs in the direction of $\vec{k}'$ if the vector $\vec{G}_{\rm hk}$ is coincident with the scattering vector $\vec{Q}$. This Laue condition is equivalent to the demand that a reciprocal lattice point lies on the Ewald sphere. By rotating the crystal, i.e. rotation of the reciprocal lattice, all points of the reciprocal lattice can cross the Ewald sphere which are inside the limiting sphere.

depends on the X–ray wavelength and is used to break Friedel's law: from equation 2.15 it follows that usually the intensity $|F|^2$ of the reflection pair (h, k, l) and $(\overline{h}, \overline{k}, \overline{l})$ are equal. By adjusting the wavelength of the photons the intensities of specific Friedel–pair reflections are different and the phases can be calculated. For these three techniques the positions of the heavy atoms or the anomalous scatterers must be found first and subsequently the phases are determinated.

The resulting electron density map is used to create an initial atomic structure model. Starting from this model the experimental diffraction phases are modified and a new map is calculated using model derived phase information. This process is repeated until convergence of the phases is reached. Then the atomic model is refined against the measured data. The knowledge of the amino acid sequence and the principle geometrical construction of a protein, i.e. the form of bond angles, distances, torsional bond potentials and van der Waal forces, lead to constraints of the atomic position $\vec{r}_j$ in equation 2.15 and limit the free parameters in the refinement. Finally structure factors can be calculated from the electron density map of the Fourier back transformation. This allows the comparison of the measured structure factors $|F^{\mathrm{obs}}_{\mathrm{hkl}}|$ with the calculated structure factors $|F^{\mathrm{cal}}_{\mathrm{hkl}}|$, based on the best atomic model built from the experimental electron density map.

The reliability factor or R–factor is summed over all structure factors and can be written as

$$R_{\mathrm{cryst}} = \frac{\sum_{\mathrm{hkl}} \left| |F^{\mathrm{obs}}_{\mathrm{hkl}}| - |F^{\mathrm{cal}}_{\mathrm{hkl}}| \right|}{\sum_{\mathrm{hkl}} |F^{\mathrm{obs}}_{\mathrm{hkl}}|} . \tag{2.17}$$

Typical values for the R–factor range from 0.13 to 0.30. In an experiment where reflections have been collected up to 2 Å resolution an R–factor below 0.2 is usually expected in well determinated structures.

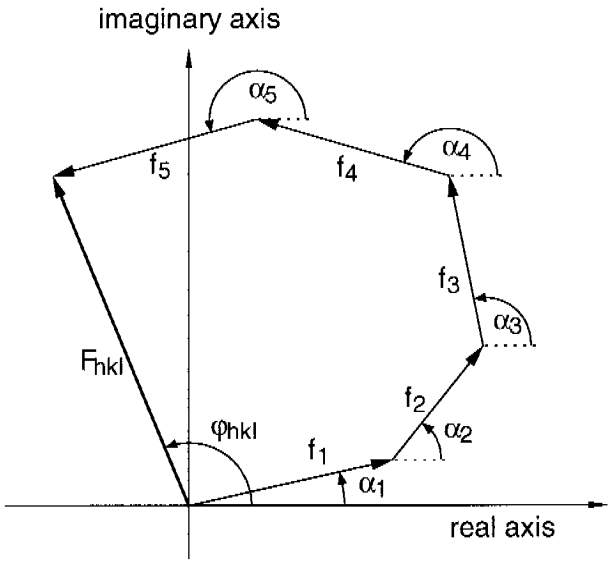

Figure 2.6: The unit cell structure factor F_{hkl} drawn in the Gauss plane. The unit cell contains 5 atoms with the atomic structure factors f_i, α_i.

In addition to Bragg reflections X–ray diffraction inevitably generates diffuse background scattering. The background is a sum of the following effects:

- Inelastic scattering
- Solvent scattering in the protein crystal
- Lattice defects
- Random or correlated motions of the molecules
- Scattering of the crystal's support medium

Both the intensity of the Bragg reflections and the background is reduced by air scattering, which also adds to the background. Furthermore, the intensity per area of background falls off by $1/r^2$, whereas the intensity of the Bragg reflection is constant in this respect, if the primary X–ray beam is parallel. In order to measure the intensity of the reflections as accurately as possible the background can be reduced by increasing the crystal to detector distance.

2.2 The Ideal Detector

From the previous chapter the properties of an ideal imaging device for X–ray crystallography can be extracted. The ideal detector is a guideline for detector developments: some properties of detectors can be improved while compromising on others.

The requirements of protein crystallography can be summarized as follows: the position of all diffracted reflections of a crystal and their integrated intensities must be measured with high precision. This leads to the following characteristics of an ideal detector:

- Detective quantum efficiency (DQE): the DQE is a measure of the overall system efficiency and is defined as $\mathrm{DQE} = \frac{\mathrm{SNR}^2_{\mathrm{out}}}{\mathrm{SNR}^2_{\mathrm{in}}}$, where SNR is the signal to noise ratio. For the best measurement all incident photons must be detected without intrinsic detector noise. In other words the detector must have a detective quantum efficiency of unity ($\mathrm{DQE} = 1$).
- Dynamic range: reflections can have a very high or extremely weak intensity. To achieve good statistics for the weak reflections, long exposures are required. Improved measurements of weak reflections extent the data to higher structure resolution. To be able to collect the high intensity reflections as well, a dynamic range of 3–5 orders of magnitude is desired.
- Active area: reflections occur in all possible directions around the sample crystal. However, by rotating the crystal for a certain angular range, which depends on its symmetry, all reflections could be measured by covering a half–sphere with the detector. In practice an area detector should cover a typically 2θ range of $\pm 60°$. A large sample to detector distance thus requires a large detector area.
- Spatial resolution: Depending on the unit cell dimensions of the crystal, reflections can be very close together. The spatial resolution must guarantee more than one pixel between two individual reflections. Therefore the detector must provide enough pixels in the active area. The spatial resolution and the active area of the detector depend on each other. For detectors with big pixels the distance to the sample must be increased, requiring a

large area. Smaller sized detectors demand small pixels.
To resolve the profile of a reflection a certain spatial resolution is required. If the divergence of the X–ray beam and its size is small, even large detectors at large distances need relatively small pixels.

- Readout speed: high intensity synchrotron sources require short exposure times in the order of a second. To minimize the experimental time it is therefore important that the read–out of the images is in the same order as the exposure time. If the angular rotation increment is decreased (fine ϕ–slicing) this becomes even more essential and a rapid read–out time of a few milliseconds is required.

- Efficiency dependence on the wavelength, λ, of the X–rays: for MAD and SAD experiments λ is varied. This technique becomes increasingly important for the phase determination since synchrotron light can be easily tuned to a certain wavelength. Typically λ is varied between 0.8 and 1.7 Å. Ideally the response of the detector is not depending on these changes.

- Uniformity of X–ray response and spatial calibration: every imaging detector must be calibrated for the variation of the individual pixel response and for spatial distortions of the image. The performed corrections should be easy to calculate and must have long term stability.

- Development, production and cost: with an infinite budget and time a nearly ideal detector is imaginable. But a real detector must be developed in a suitable time and at an acceptable price. The production of such a device should be possible in larger quantity and the cost should be scaled to the cost of providing the photons.

Currently the read–out time is the largest limitation of detectors for protein crystallography. Furthermore, the long read–out time and read–out noise prohibit fine ϕ–sliced experiments, as investigated in section 5.3.

2.3 CCDs and Hybrid Pixel Area Detectors

With recent developments of hybrid pixel array detectors (PADs) a new type of X–ray detector is added to the existing group of large area X–ray detectors — a modular silicon detector with single photon counting electronics. Although there were pixel array detectors developed with integrating electronics (so called APADs) [16, 17], PADs reported in this work refer only to single photon counting devices. In addition several other large area detectors are under development, for example the monolithic amorphous silicon flat panel detector from Marresearch (Marresearch GmbH, Norderstedt, Germany) and the MEDIPIX–project [5, 18, 19]. Many different realizations of CCD detector systems have been investigated [20, 21] and there is a lot of effort put into the improvement of this type of detector.

In this section a comparison between the most popular X–ray detector — the CCD detectors — and hybrid pixel detectors is given. The basic building blocks of these detectors will be explained and the major properties will be discussed.

2.3.1 Large Area CCD Detectors

A CCD detector consists of the modular building blocks shown in Figure 2.7. The large phosphor screen converts X–ray photons to visible/IR light. An optical element is needed to focus the image onto the smaller charge coupled device (CCD chip). The chip itself integrates the signal and is read–out after each exposure. An amplifier and an analog to digital converter (ADC) are needed at the end of the electro–optical chain. Each component of a CCD detector must be carefully chosen to fit the particular experimental needs. This leads to a wide variety of different devices, which have been intensively discussed in [22]. As only detectors for protein crystallography will be discussed here, a particular CCD type is specified for the comparison: the fiber optical coupled CCD detector. It consists of the following five elements:

- Phosphor screen
- Coupling element, i.e. a fiber optic taper
- Charge Coupled Device (CCD chip)
- Amplifier
- Analog to digital converter (ADC)

Phosphor Screens

The first step of the signal processing chain in imaging detectors is the conversion of the X–ray photons in defined quanta which can be guided and stored by the later components. As CCD chips are specified for photons in the visible/IR wavelength range, the short wavelength photons of X–rays have to be converted into visible or IR light. To shift the wavelength of photons, luminescent materials can be used. The luminescent arises from transitions of different energy levels of the main doping material in the screen. These materials are called 'Phosphors'. The most common phosphor is $Gd_2O_2S : Tb$. The luminescent element Tb^{+3} emits photons mainly in the green ($^5D_4 - ^7F_J$ transition) and in the blue ($^5D_3 - ^7F_J$ transition). This material is available as powders with a certain particle size which is bound with a binder material onto an X–ray transparent window (Fig. 2.8). The window must protect the phosphor against water vapor and visible light by means of a thin aluminum foil (aluminized Mylar). To rapidly record series of images, the photo–luminescence should decay rapidly. Typically the intensity of the emitted light drops down by 3 orders of magnitude within 0.1 s [22]. This leads to a nonlinearity of the output signal as some atoms are not recovered in their ground state when new X–ray photons arrive in the sensor.

The stopping power of a phosphor increases with the thickness of the screen. To define the thickness two points have to be considered (Fig. 2.8). A thick sensor converts most of the penetrating X–rays but the luminescent light cannot escape the screen easily. The efficiency of the phosphor is defined by the fraction of the emitted light for each stopped X–ray. The best phosphor offers an energy efficiency of 15-20 % ($Gd_2O_2S : Tb$ and $ZnS : Ag$). It is unlikely to find a substantially better phosphor than $ZnS : Ag$ [22]. The luminescent photons are emitted 360° from the conversion point. These photons can travel laterally in the phosphor until they are redirected by other particles. This spread of the luminescent light defines the spatial resolution of the screen. As this lateral spreading increases with the thickness of the

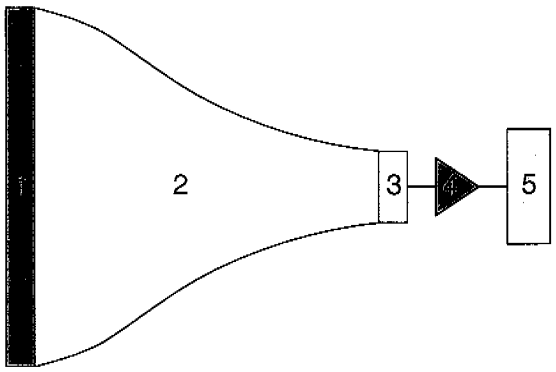

Figure 2.7: Building blocks of a CCD detector: X–rays are converted to visible light in a phosphor screen (1). The image is focused (2) to the smaller CCD chip (3) where the light is converted to charge in each pixel. During read–out this charge is shifted out and is amplified (4) and finally converted to a digital number (5).

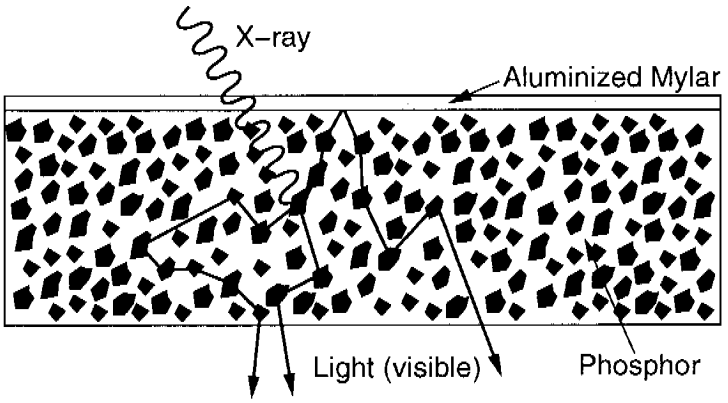

Figure 2.8: Schematic cross section through a phosphor screen filled with small particles ('Phosphors') which convert X–rays to visible light photons. These photons follow ballistic trajectories in the particles.

phosphor it works directly against the demand for higher X–ray stopping power. The spread of light is characterized by the difference between the incident X–ray and the visible/IR image. The distribution of the output signal for a point input signal is defined by the normalized point spread function (PSF).

$$1 = \int_{x=-\infty}^{x=+\infty} \int_{y=-\infty}^{y=+\infty} \mathrm{PSF}(x,y)dxdy = 2\pi \int_{0}^{\infty} \mathrm{PSF}(r)dr \,, \tag{2.18}$$

If the PSF is translational invariant across the phosphor screen, the output response of a diffraction pattern $h(x,y)$ is the convolution of the input image $g(x,y)$ with the PSF:

$$h(x,y) = \mathrm{PSF}(x,y) * g(x,y) \,. \tag{2.19}$$

Tate et al. have measured the PSF for a 30 μm thick $Gd_2O_2S : Tb$ phosphor screen [23]. The results of their measurement show that the short–range PSF drops rather rapidly, giving a very small width (FWHM = 80μm). On the other hand the long–range PSF, with low intensity, can spread over several pixels (full width at $^1/_{1000}$ maximum = 450μm).

Fiber Optic Taper

To focus the output image of the phosphor screen onto the CCD chip, fused fiber optic tapers are very efficient. They consist of many glass–fiber light guides with a diameter of 3 to 25 μm. The fiber bundle is melted and stretched to create a typical demagnification. A fiber optic taper introduces a spatial distortion due to the melting and stretching steps. The efficiencies of the tapers are related to their magnification (see Table 2.1). A large detector area of e.g. 180 × 180 mm^2 requires a magnification of 0.03 because CCDs larger than 30 × 30 mm^2 are difficult to obtain. Therefore multi–taper arrays focus the image to several CCD chips. For the given example a 3 × 3 taper matrix would lead to a magnification of 0.25. Between the tapers is a small area which is either empty or shows different properties than the core of the taper.

Magnification	Fiber optic taper efficiency (%)
1	75
0.5	20
0.3	13
0.25	9

Table 2.1: Efficiency of fiber optic tapers depend on the magnification [22].

CCD Chip

On the small end of the fiber optic taper the light is directed onto the CCD chip. Large area CCD chips without defects demand a high quality fabrication and are expensive. Today, a silicon chip is monolithically fabricated and consists of discrete columns, separated by potential barriers (Fig. 2.9). The surface is insulated by a silicon dioxide or silicon nitride layer and is overlaid with rows of clocking gates perpendicular to the columns. The pixels are thus separated by the potential barriers between the columns and by an external voltage within one column.

Photons generate a charge in the depletion region buried in the chip. After the exposure phase the accumulated charge is shifted down the columns by clocking the gates to the analog output shift register. There the charge packets are shifted out after each column clock along the row to an amplifier.

In modern chips the amplifier is directly fabricated on the chip itself. As the amplifier senses only the capacitance of the last pixel, the noise of the amplifier is very low. Scientific CDD chips can have noise levels as low as 10 electrons per pixel (marccd225, Mar USA, Inc., Evanston, USA). The analog signal of the amplifier is finally converted with an ADC and then transferred to a computer storage device. The efficiency of a CCD chip is limited by the number of photons stopped in the polysilicon layers of the device. Silicon is fully transparent in the infrared but less than 30 % at 550 nm and less than 10 % at 450 nm (blue) of the light photons reach the photosensitive bulk of the chip. A way to improve this situation is to reduce the path length of the photons in the polysilicon by illuminating the chip from the back side. This requires thinning the device down to a few micrometers ($\sim$ 10 μm). But as this process reduces the yield of the fabrication, the price of the chip would be further increased.

The read–out time of the CCD depends on several factors. First, the charge needs time to travel along the columns and rows to the amplifier. Second, the precision of the ADC conversion scales with the time needed for this process. Third, the digital number is transferred to a computer disk. The speed of this read–out sequence can be increased by dividing the chip into several regions with more outputs. During the read–out phase the CCD chip must be protected

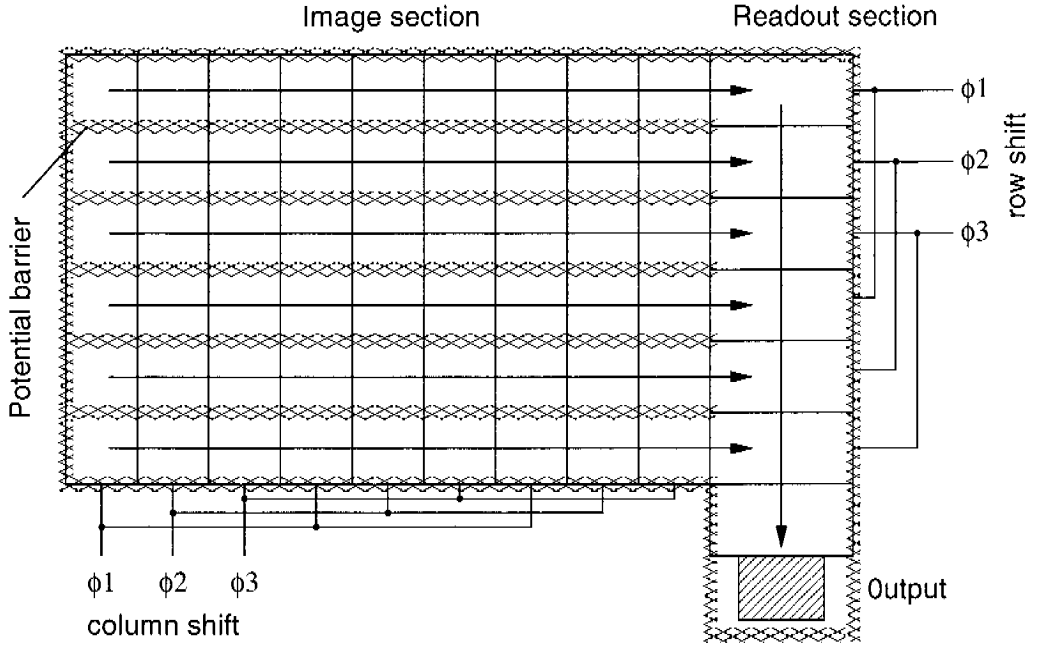

Figure 2.9: Pixels of a CCD chip are separated by implanted potential barriers and by overlaid electrodes. Photons are converted into charge in each pixel. By changing the voltage on the ϕ electrodes (column shift), the integrated charge in the image sections is shifted out to the output shift register. With the row shift electrodes the shift register is read–out.

from further exposure with a mechanical shutter. After all charge is shifted out of the chip a new exposure can be started. For setups optimized to a high framing rate, the decay time of the phosphor screen must be taken into account, as discussed in section 2.3.1.

Efficiency of a CCD Detector System

The total signal from a CCD detector is the sum of all efficiencies of all relays in the signal chain:

$$N_s = E_x/E_p C_P C_F Q_{\mathrm{CCD}} \,, \tag{2.20}$$

where N_s is the number of electrons collected in the CCD pixel, E_x the X–ray photon energy, E_p the energy of the emitted light photons of the phosphor screen, C_P and C_F the efficiencies of the phosphor and the fiber optic taper and Q_{CCD} the quantum efficiency of the CCD chip. Some numbers illustrate the equation. Good phosphors like $Gd_2O_2S : Tb$ convert about 15 % of the X–ray photon energy to visible light. But many of the photons are emitted into the wrong direction and only about 10 % reach the fiber optic taper. This means that for one penetrating X–ray photon of 12 keV and an energy of the emitted light photons of 2.5 eV (500 nm) 480 light photons enter the fiber. With a demagnification of 0.25, C_F is 9 % (Table 2.1) and a typical value for Q_{CCD} is 30 %. The total number of electrons, N_s, for one event is therefore $12000 \,/\, 2.5 \times 0.1 \times 0.09 \times 0.3 = 13$. With a noise of 10 electrons, the signal to noise ratio $S/N \approx 1.3$.

2.3.2 Hybrid Pixel Array Detectors

A hybrid pixel detector consists only of two elements (Fig. 2.10):

- Semiconductor sensor
- ASIC CMOS chip

A semiconductor sensor is directly connected to the CMOS chip, which eliminates the efficiency loss of the optical element but also couples the size of the read–out electronics with the pixel size of the sensor. This has been a major drawback for pixel detectors, but with the modern CMOS technology very small pixels can be designed. Each pixel contains an amplifier and the signal storage part. One key point of this architecture is the inter–connection technology: bump bonding has been developed in the early times of the electronic industry, but only recently the dimensions of the bump balls became small enough to be useful for the imaging devices discussed here.

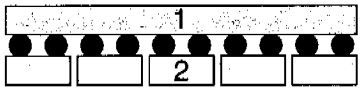

Figure 2.10: Building blocks of a hybrid pixel area detector: The semiconductor sensor (1) converts X–rays to charge which is transferred via small balls to the corresponding pixels of the CMOS chips (2). The pixel electronics comprises of an amplifier, a comparator and a digital counter.

Semiconductor Sensors

In a PAD the signal of impinging photons is directly converted into charge in the semiconductor sensor. For the discussion a summary of the physics of X–ray conversion in semiconductors, which is described in many publications (e.g. [24, 25]), is given first.

The energy of X–ray photons is absorbed by the bound electrons of the atoms of the semiconductor crystal due to the photo-electric effect. These *photo-electrons* create electron–hole pairs in the semiconductor. The number of these pairs, N_{eh}, is determined by the ionization energy E_{ion} of the semiconductor and the photon energy E_{ph} as

$$N_{\mathrm{eh}} = E_{\mathrm{ph}}/E_{\mathrm{ion}} \ , \tag{2.21}$$

with the empirical equation from Klein [26, 27]

$$E_{\mathrm{ion}} = 2.97\ E_{\mathrm{gap}} + 0.87 \ . \tag{2.22}$$

The band gaps E_{gap} for several semiconductors are listed in Table 2.2. The measured value, however, differs slightly from Klein's equation. E_{ion} for silicon has been measured between 3.62 and 3.65 eV. The radius of the resulting charge cloud is very small and can be approximated by

$$\begin{aligned} R &= 0.090\ \rho^{-0.8}\ E^{1.3} \quad \text{for } E < 10\ keV \\ R &= 0.045\ \rho^{-0.9}\ E^{1.7} \quad \text{for } E > 10\ keV \ , \end{aligned} \tag{2.23}$$

where R, in micrometers, is the radius of the material where the electron transmission is reduced to 1 %, E is the electron energy in keV and ρ is the material density in $\mathrm{g/cm^3}$ [28]. 12 keV X–rays for example give a R of 1.2 μm in silicon. The charge needs to be separated by an electric field, because otherwise the holes and electrons would quickly recombine. This can be done by applying a reversed bias voltage to a semiconductor diode.

Detector diodes consist of n– and p–doped regions; n–type semiconductors have free electrons as charge carriers with holes fixed in the crystal lattice and p–type semiconductors vice versa. Once these two materials are in contact with each other, free electrons and holes diffuse through the p–n junction into their counterparts and an excess of negative charge will be created in the p region and an excess of positive charge in the n region. This creates an electric field that counteracts the diffusion. The electric field also sweeps away any mobile charge carriers (electrons and holes) in the region around the boundary, so that a space–charge region is obtained — the depletion region — in which the excess nuclear charge of the doping atoms is not neutralized by the movable carriers. In the equilibrium the strength of the electric field is V_0, which is typically below 1 V for most materials.

For a reversed biased diode, the voltage across the junction will increase from the equilibrium value V_0 by the externally applied voltage V_{bias} to $V_0 + V_{\mathrm{bias}}$ .The width of this space–charge region is given by

$$x = \sqrt{\left(\frac{2\epsilon_s}{e}\frac{(N_a + N_d)}{N_a N_d}\right)\sqrt{\mid V_0 \mid + \mid V_{\mathrm{bias}} \mid}} \ , \tag{2.24}$$

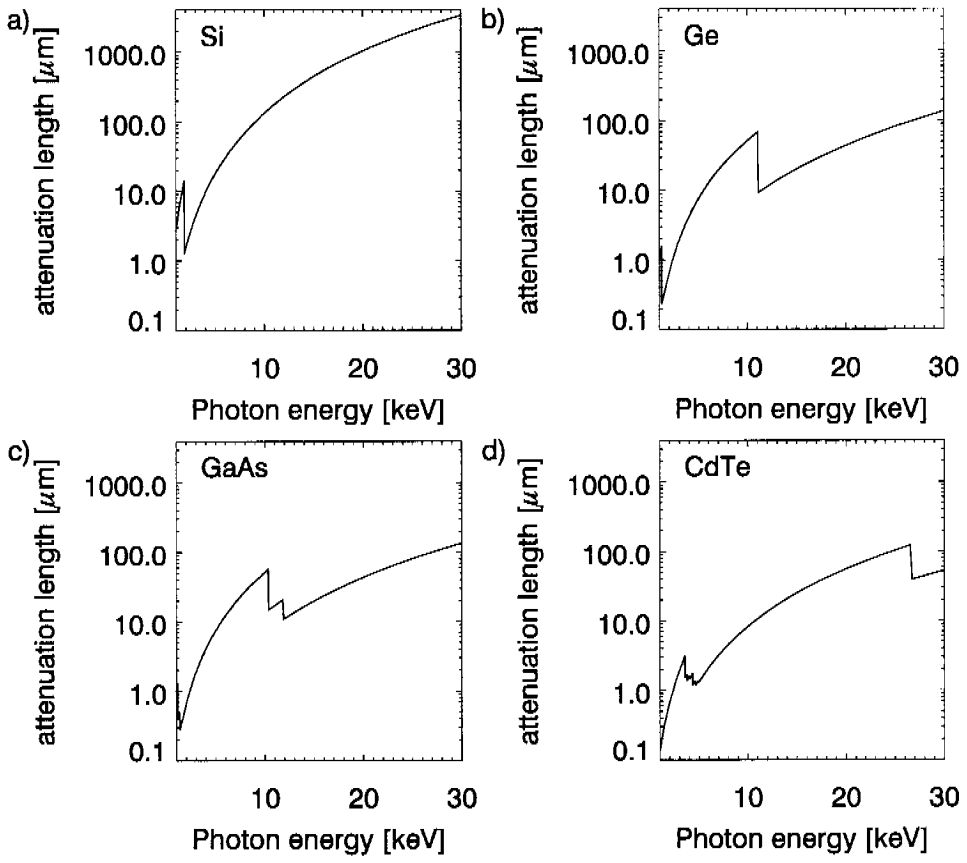

Figure 2.11: Attenuation length for typical semiconductor sensors on a logarithmic scale. a) Si; b) Ge; c) GaAs; d) CdTe. The discontinuous steps occur from absorption edges of the materials.

Material	E_{gap} [eV]	μ_e,	μ_h [cm^2/Vs]	ρ_r [Ωcm]	ϵ_r	ρ [g/cm^3]	Z
Si	1.12	1450	450	$> 10^3$	11.9	2.33	14
Ge	0.66	3900	1900	$> 10^1$	16.0	5.32	32
GaAs	1.42	8500	400	$> 10^8$	13.1	5.32	31/33
CdTe	1.56	1050	100	$> 10^2$	10.2	8.65	48/52

Table 2.2: Electronic properties of semiconductors [25]: Energy band gap E_{gap}, mobility of electrons μ_e and holes μ_h, the resistivity ρ_r, the dielectric constant ϵ_r, the material density ρ_r and the atomic number Z. Figure 2.11 shows the attenuation lengths for this semiconductors.

with ϵ_s being the semiconductor permittivity[4], e the elementary charge, and N_a and N_d the bulk concentrations of acceptor and donor dopants in the p– and n–type materials, respectively. The concentrations of the dopants and their mobilities μ_e and μ_h define the resistivity ρ_r of the material:

$$\rho_r = \frac{1}{eN_a\mu_e + eN_d\mu_h} . \tag{2.25}$$

The mobility of electrons μ_e and holes μ_h in semiconductors and the resistivity at room temperature are listed in Table 2.2. The slower motion of the positive charge is a consequence of its larger effective mass m^*. In most p–n diodes one material is more heavily doped. If for example the n–type material is dominant then N_d is much larger than N_a. The external voltage can be several orders of magnitude larger than the equilibrium voltage. The depletion width x (equation 2.24) can thus be approximated with

$$x \approx \sqrt{2\epsilon_s\mu_h\rho_r V_{\text{bias}}} . \tag{2.26}$$

To create a thick space–charge region a material with high resistivity or high charge mobility is needed. To fully deplete a 300 μm thick n–type silicon sensor with e.g. $V_{\text{bias}} = 100$ V, a resistivity of ~ 9.5 kΩcm is required. As this region is free of charge carriers it represents an insulator between the two materials. The depletion capacitance per unit area of a p–n diode (n–type material) can be derived from the equations 2.25 and 2.26:

$$C \equiv \frac{dQ}{dV} = \underbrace{\frac{dQ}{dx}}_{\approx 1/\mu_h\rho_r} \underbrace{\frac{dx}{dV}}_{\approx\sqrt{\epsilon_s\mu_h\rho_r}(2V_{\text{bias}})^{-\frac{1}{2}}} \tag{2.27}$$

$$\approx \sqrt{\frac{\epsilon_s}{2\mu_h\rho_r V_{\text{bias}}}} = \frac{\epsilon_s}{x} . \tag{2.28}$$

In the example above, the 300 μm thick diode with an area of 200×200 μm^2 has a capacitance of 14 fF.

The electron–hole pairs, generated in the space–charge region by the irradiation of X–rays, are separated by the electric field and a photocurrent is generated. The number of absorbed photons in the sensor depends on its density and thickness:

$$I_a = I_0 \left(1 - e^{-\left[\frac{\mu}{\rho}\right]\rho x}\right) , \tag{2.29}$$

with the mass attenuation coefficient μ/ρ, the density ρ and the thickness x of the sensor. The mass attenuation coefficient represents the fraction of incident photons interacting with the material. The coefficient is dominated by the photo–electric cross–section per atom and is proportional to Z^n ($n = 4..5$) [29, 30]. Thus 'high Z materials' are potentially better materials for X–ray sensors. The reciprocal of μ/ρ is the attenuation length and defines the average distance photons can travel in the sensor without interaction. In Figure 2.11 the attenuation length is plotted as a function of the photon energy for several materials. The photons cannot excite the electrons of the relevant atomic level below an absorption edge and thus the attenuation length

[4]The semiconductor permittivity is defined as the permittivity in vacuum $\epsilon_0 = 8.85418 \cdot 10^{-12}$ F/m times the dielectric constant ϵ_r, i.e. $\epsilon_s = \epsilon_0\epsilon_r$.

is high. However, when the photon energy is just sufficient to excite the electrons, then a large increase in the absorption occurs, resulting in a decreased attenuation length.

To produce high resistivity and high quality sensors, high–purity semiconductor material without imperfections is required. Silicon is the most widely available semiconductor which meets this demand and is thus an excellent choice for X–ray sensors. The pixel structure is fabricated by photolithographically implanting p^+–type material into weakly doped n–type sensor material. A cross section of such a sensor is printed in Figure 2.12. Through the external voltage V_{bias} the depletion region of the diodes is nearly as wide as the sensor itself. The top n^+ layer is insensitive to X–rays.

The photons enter the sensor from the aluminized n^+–side and the photocurrent is collected at the p^+ electrode. The thickness of the n^+ layer (typically a few micrometer) is therefore limiting the efficiency of the sensor for low energy X–rays. The efficiency for different sensor thicknesses is plotted in Figure 2.13. The effective thickness is approximately the width of the depletion region. The consequence of a n–type sensor is that the positive charge carriers with smaller mobility is collected.

The spatial resolution of a semiconductor sensor is almost completely defined by the size of the pixel structure and the sensor thickness. For normal angles of incidence nearly all of the charge from a point X–ray beam is collected in only one pixel. This leads to a virtually ideal single pixel PSF. The position of reflections, which are recorded in a single pixel, can therefore only be determined to a precision equal to the pixel size. But it is also possible that charge, generated in one pixel, spreads to the neighboring pixel if the conversion point is near the pixel boundary . In this case charge spreads into several pixels and the position can be determined with higher precision.

The charge collected at the p^+ electrode of the sensor is transferred via an electric conductive material to a preamplifier on a ASIC CMOS chip. The inter–connection technique used here, called *bump bonding*, uses indium or solder balls as conducting material. It is possible to make bump balls smaller then 20 μm.

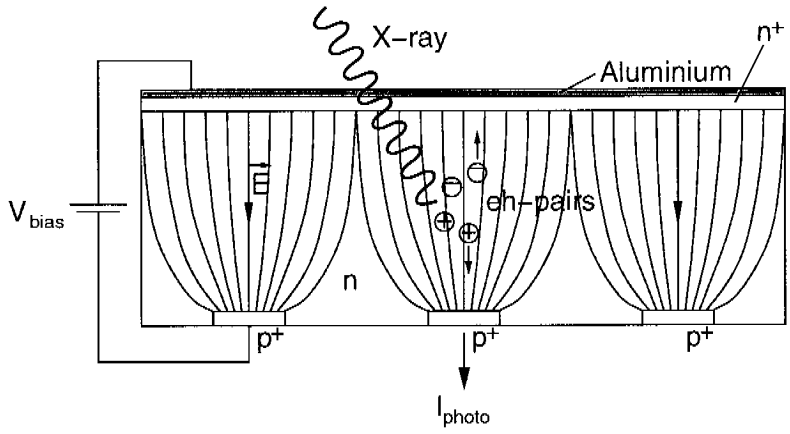

Figure 2.12: Schematic cross section through a silicon pixel sensor. The pixel structure is defined by the p^+ implants. The pixel–diodes are over–depleted by the applied voltage V_{bias}. Electron–hole pairs generated by X–ray photons follow the electric field lines $\vec{E}$ to the top n^+ layer and the p^+ implant respectively. For better conduction the n^+ layer is overlaid by a thin aluminum layer. The signal I_{photo} is collected from the p^+ electrode of the pixel and is proportional to the X–ray energy.

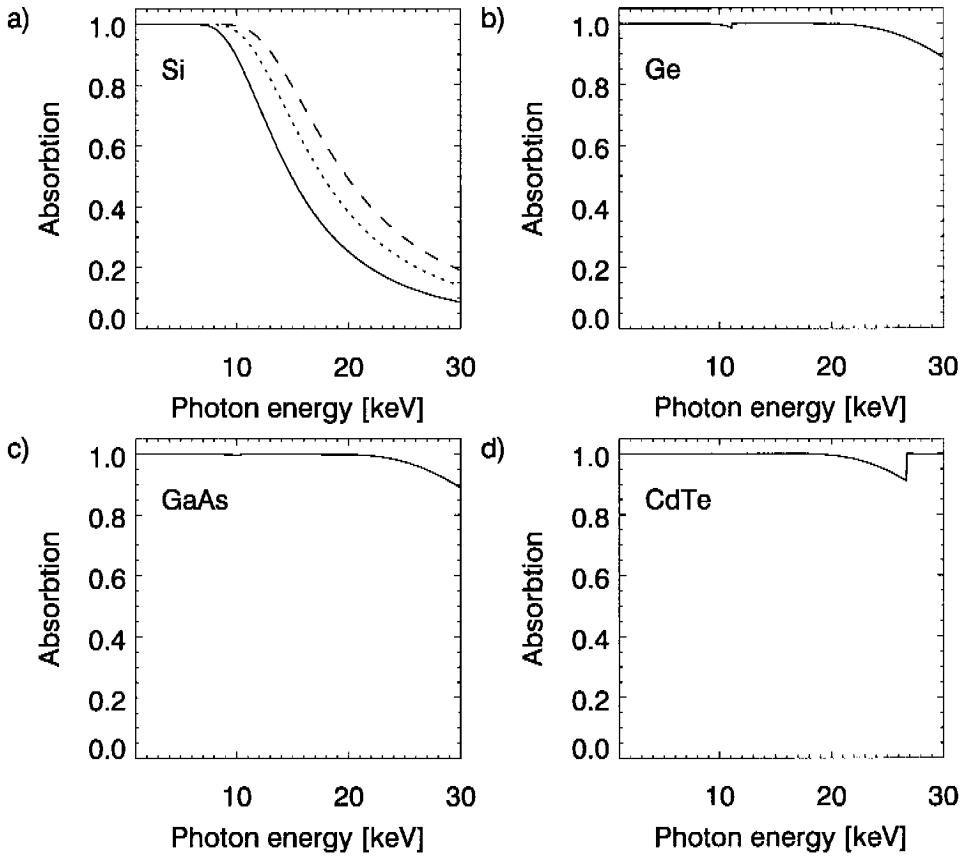

Figure 2.13: Absorption capability for semiconductors. a) Si, the sensor thickness d is 300 μm (line), 500 μm (dotted) and 700 μm (dashed). b) Ge, $d = 300$ μm; c) GaAs, $d = 300$ μm; d) CdTe, $d = 300$ μm.

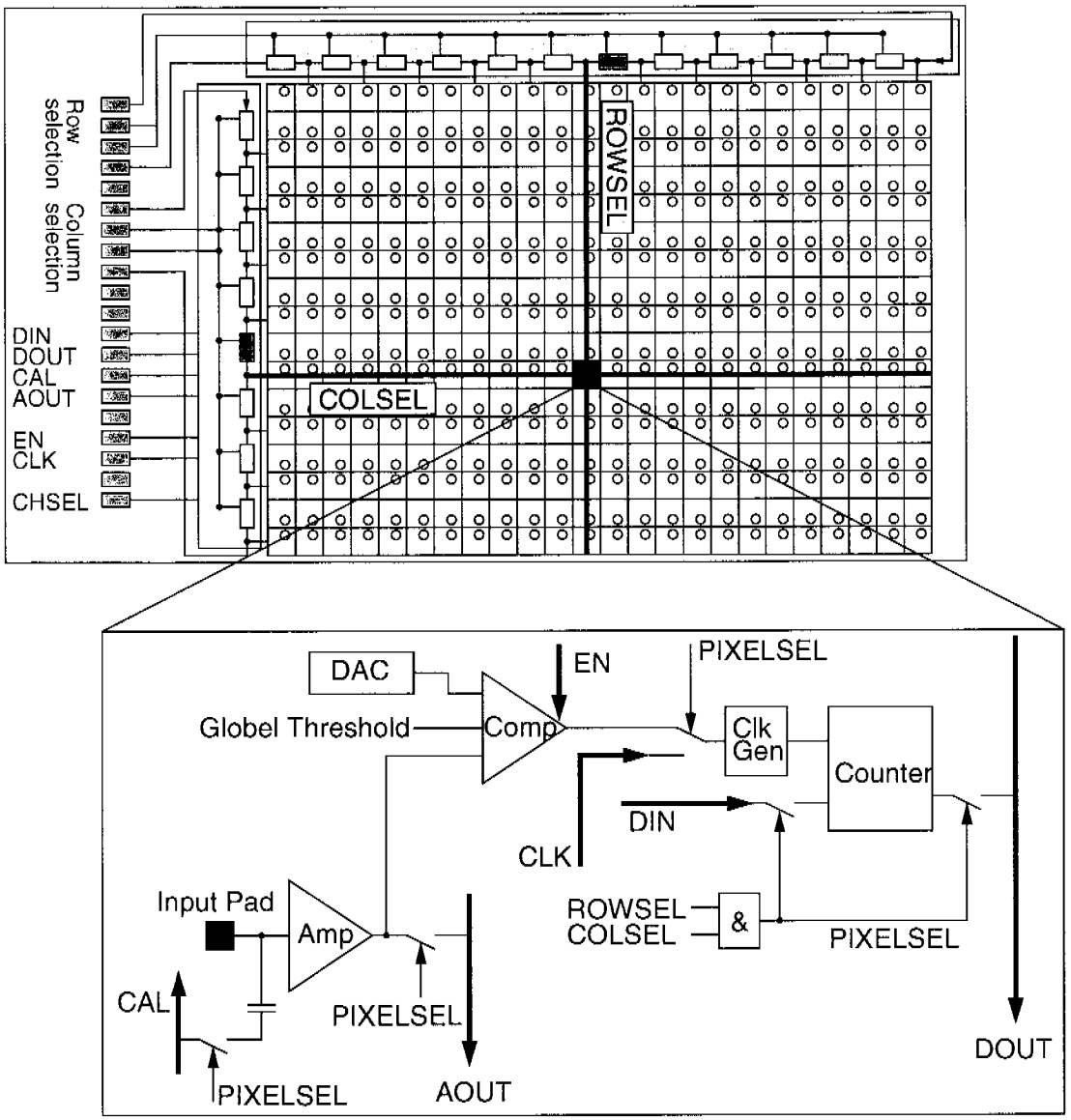

Figure 2.14: Architecture of the CMOS chip (top) and of a single pixel (bottom). During an exposure (EN= 1) no pixel is selected and all pixels are in counting mode. Charge from the input pad is amplified. The event will be registered in the counter if the charge is above the threshold of the comparator. After the exposure the pixels are selected, read–out to the output pad (DOUT) with a clock signal (CLK) and are reset via DIN. The threshold is adjusted by a global voltage and can be fine tuned by the DACs. Charge can also be fed into the amplifier by an external calibration signal (CAL).

CMOS Chip

The general scheme of the single photon counting circuit in the pixel is divided into an analog part with an amplifier and a comparator and a digital part which is a digital counter (Fig. 2.14).

- *The amplifier*
  In the amplifier incoming charge is converted and amplified to a voltage pulse. Using equation 2.21 it can be calculated that one 6 keV X–ray photon produces 1667 electron–hole pairs. This charge is integrated and converted to an output pulse of several millivolts.
- *The comparator*
  As the amplitude of the amplifier output signal is proportional to the photon energy, a comparator can set a lower and upper limit for the further processing of the signal.
- *The digital counter*
  The output of the comparator(s) is a digital pulse which controls the clock of a digital counter. Therefore, the chip is *single photon counting*. The input of the counter is gated by a global enable signal (EN). After an exposure the counter content is read–out.

Through this architecture the noise of the amplifier, fluorescence background radiation and leakage current of the sensor can be completely suppressed. The comparator is also necessary to suppress signals coming from shared events: if the level for the threshold is exactly set to half of the photon energy only the stronger part of a shared event will be seen from the counter. Several studies show that charge sharing is not of major concern for single photon counting detectors if the pixel size is not extremely small (e.g. $\sim 50 \times 50\ \mu m^2$) [18, 31].

The integration time of the amplifier leads to a so called *resolving time* ρ_t of the single counting electronics, which leads to a counting rate limitation. All counting detectors have this limitation and have one of three possible counting rate dependencies: linear, non–paralyzable or paralyzable. The counting rate dependencies are shown in Figure 2.15 [30]. CCDs belong to the non–paralyzable type with a very short ρ_t (luminescent photon emission time): the event can only be converted and integrated in the CCD chip, if not all atoms of a sensor pixel are exited. The analog amplifier of a PAD paralyzes the pixel electronics for a time ρ_t. Successor photons arriving sooner than ρ_t will be added to the previous signal (pile up). In this case the digital counter sees only one single event. However, this can be compensated by a rate correction.

As the data is digitally stored in each pixel, the read–out sequence is simplified and the read–out time is significantly reduced in respect to the read–out time of a CCD. All the data of the pixels is transferred into an intermediate storage memory. If this is done in parallel for all sub–units of the PAD the read–out time is only a few milliseconds. Within this time the counter is switched from counting to read–out mode (Fig. 2.14) and is insensitive to X–rays. Therefore no mechanical shutter is needed. The transfer of data from the intermediate memory to a computer disk can be done during the next exposure.

Efficiency and Spatial Resolution of a PAD Detector System

The overall efficiency of a PAD is dominated by the stopping power of the sensor. The physical properties of silicon demand a certain thickness of the sensor to stop most of the photons, especially for higher photon energies. This limitation can only be abandoned by using different

sensor materials like CdTe or Germanium. Thus intensive research work is being done to produce such sensors of high quality. But today Ge–sensors need cooling to very low temperatures to reduce their high leakage current, whereas detectors with silicon sensors can operate at room temperature. The overall spatial resolution is dominated by the pixel size of the readout chip. Semiconductor sensors can be produced with very small structures, but each pixel area on the readout chip must contain the complete read–out electronics. Therefore the size is set by the compactness of the electronic design. With modern processing technologies of CMOS chips this limitation is more and more reduced.

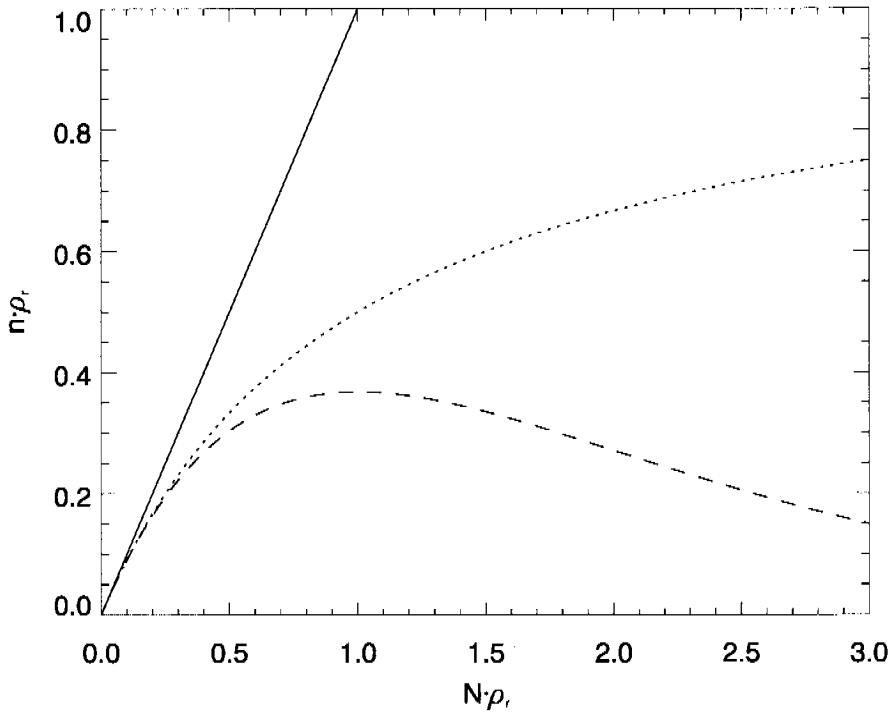

Figure 2.15: Rate dependency of counting detectors. Because of the finite resolving time ρ_t of the detector, the observed counting rate n is lower than the true counting rate N. A paralyzable detector counts all intervals which are longer than ρ_t (dashed line); the maximum observed counting rate is at $N = 1/\rho_t$ and is equal to $n_{\max} = 1/e\rho_t$. A non–paralyzable (saturating) detector is completely insensitive for a time ρ_t after each observed event, then regains full sensitivity; it approaches asymptotically the value $n_{\max} = 1/\rho_t$ for $N = \infty$ (dotted line). A detector with $\rho_t = 0$ would follow the straight line of an ideal detector (linear response).

2.3.3 Performance of CCDs and PADs

The major difference between a CCD and a PAD is caused by the signal processing type: CCDs are *integrating* devices whereas PADs discussed here are *single photon counting* devices. Therefore the two detector types behave differently in the following aspects:

- Noise, dark current and background radiation: Depending on the temperature, electronic noise and dark current is present in the material of the sensor and the readout chip. A CCD chip integrates all these components together with the true signal. The comparator of a PAD suppresses these contributions. During read–out a CCD adds noise to the signal. The digital read–out of a PAD provides a noise free transfer of the data and is therefore superior to the CCD detector in this respect.
- Linearity: A PAD is more rate limited than a CDD because of its longer resolving time ρ_t (Fig. 2.15). However, this limitation can be compensated by a rate correction.
- Zingers are high intensity events coming from radioactive decay or cosmic radiation. In a CCD the created charge in a pixel is proportional to the energy of the photons. Therefore a zinger creates a very intense spot or line in the image. A PAD counts each event as *one*, independent of its energy. Thus a zinger forms a point or a line in the image with intensity equal to unity which normally causes it to vanish.

In general the performance of modern state–of–the–art CCD detectors and new PADs can be compared according to the listing of the ideal detector in section 2.2.

- DQE: Only very few reliable measurements of the DQE of CCDs are reported. Typical values range from 0.4 to 0.7. The DQE of a PAD is only limited by the sensor absorption properties. The absorption efficiency of a 300 μm silicon sensor is 0.98 for 8 keV (1.5 Å) X–rays, near the ideal limit of 1.0, but decreases for higher X–ray energies (0.73 for 12 keV (1.0 Å) X–rays). With the single photon counting mode for a PAD no detector noise is added to the signal in contrast to a CCD.
- Dynamic range: The charge accumulation in a CCD chip saturates at $\sim 4 \cdot 10^5$ electrons. This corresponds to $\sim 3 \cdot 10^4$ 12 keV X–ray photons (Eq. 2.20). An extension by a factor of 2 to 3 is desirable. The counter of a PAD is the largest part of the CMOS chip. Thus the size of the counter scales with the pixel size. Fifteen bit counters, counting from zero to $2^{15} = 32768$, or even 20 bit counters (zero to $2^{20} = 10^6$ counts) can be designed. Without read–out noise, images with short exposure times can be added together. Therefore the dynamic range of a PAD can be greatly extended.
- Active area: A multi–taper CCD detector can have a size of $\sim$ 325 $\times$ 325 mm^2 (marccd325). A PAD is built from individual modules. Therefore its size scales with the number of modules in the array. A size of 400 $\times$ 400 mm^2 would be sufficient for protein crystallographic experiments.
- Spatial resolution: The scattering of light in phosphors is the limiting factor for the resolution of a CCD. Although the resolution reported in the detector specifications are below 100 μm, it should not be forgotten that the value is usually taken from the FWHM of the PSF. The spatial resolution of a PAD is limited by the pixel size of the readout chip, which is dominated by the size of the digital counter. By reducing the size of the counter

or making the design more compact using new technologies, pixel sizes as smaller as $50 \times 50\ \mu m^2$ are achievable.

- Readout speed and framing time: The read–out time of a CCD depends on the operation mode. Typically read–out times of a few seconds can be achieved. The framing time (depending on the exposure time) is therefore still below 1 Hz. With only several milliseconds read–out time, the framing time of a PAD is only limited by the exposure time and the transfer time of the data from the detector to a permanent storage device (computer disk). Frame repetitions of 10 Hz can be achieved. A higher framing rate needs an advanced rapid data transfer system.
- Efficiency dependence on the wavelength: Both CCDs and PADs have a good response over the commonly used wavelength range. The efficiency of a phosphor has a broad maximum for most detector types in this energy range. The efficiency of a PAD depends on the choice of the material for the sensor. Some semiconductors, however, have a strong dependency on the efficiency in the desired wavelength range (Fig. 2.11). The attenuation length of Germanium changes over one order of magnitude at 11 keV.
- Non–uniformity of response and spatial calibration: With a few adaptations, the calibration techniques developed for CCDs can also be used for PADs. The major difference is that distortions of PADs have different origins than those of CCDs. After calibration the image corrections can be done automatically for both detector types.
- Cost: The most expensive parts in a CCD detector are the fiber optic tapers. The large CCD chips are expensive because of the small numbers needed in industry. Therefore a CCD is quite expensive for large active areas (in the order of $\sim$ 1 k\$/cm^2). The components of a PAD are the semiconductor sensor and the CMOS readout chip. The former can either be cheap, because easy to obtain (Si) or expensive, because difficult to produce (CdTe). The driving force of computer industry ensures that CMOS chips can be bought at moderate costs in large quantities. However, hybrid pixel detectors are still in development and not commercially available and thus no precise production costs can be given.

To summarize, PADs have the potential to overcome physical limitations of currently available detectors like CCDs. In Table 2.3 the properties of the two compared devices are listed. The fist column corresponds to the properties of the first hybrid pixel area detector for protein crystallography: the PILATUS 1M detector. This detector will be described and analyzed in the following chapters.

	PAD	CCD
Active area (mm^2)	243×210	225×225
Number of pixels	1120×967	3072×3072
Pixel size (μm^2)	217×217	73×73
Sensor material	Si, 300 μm thick	phosphors
Dynamic range (γ/pixel)	2^{15}	60000 **
Resolving time ρ_t (ns)	$\sim$ 600 (para.)	~ 0
Maximum counting rate (γ/s/pixel)	$\sim$ 0.6 at 1.5 (dead time correction)	unlimited
QE (e^-/12 keV X–ray)	0.7	~ 0.7
QE (e^-/8 keV X–ray)	~ 1	~ 0.8
RMS read–out noise (e^-/pixel)	zero	10
Dark current (e^-/s/pixel)	zero	< 0.01
Point spread FWHM (μm)	zero	100
Point spread FW1%M (μm)	zero	300
Readout speed (ms)	5.9	2000
Framing rate (Hz)	$\sim$ 2 (prototype setup)	< 1
Operating temperature (K)	$\sim$ 298	208

Table 2.3: Specifications of a PAD (PILATUS 1M detector) and a CCD (marccd225) (** 12 keV X–ray photons).

Chapter 3

The PILATUS 1M Detector

3.1 The PILATUS 1M Detector and its Building Blocks

The PILATUS 1M detector is a modular detector built out of 18 individual modules. It was assembled in fall 2003 and is described in [32, 33]. The modules are arranged in an array of 3×6 units, where three modules are mounted on a bank. In Figure 3.1 the sensitive detector area of 243×210 mm^2 is shown. The banks are tilted by $6°$ in respect to the mounting base

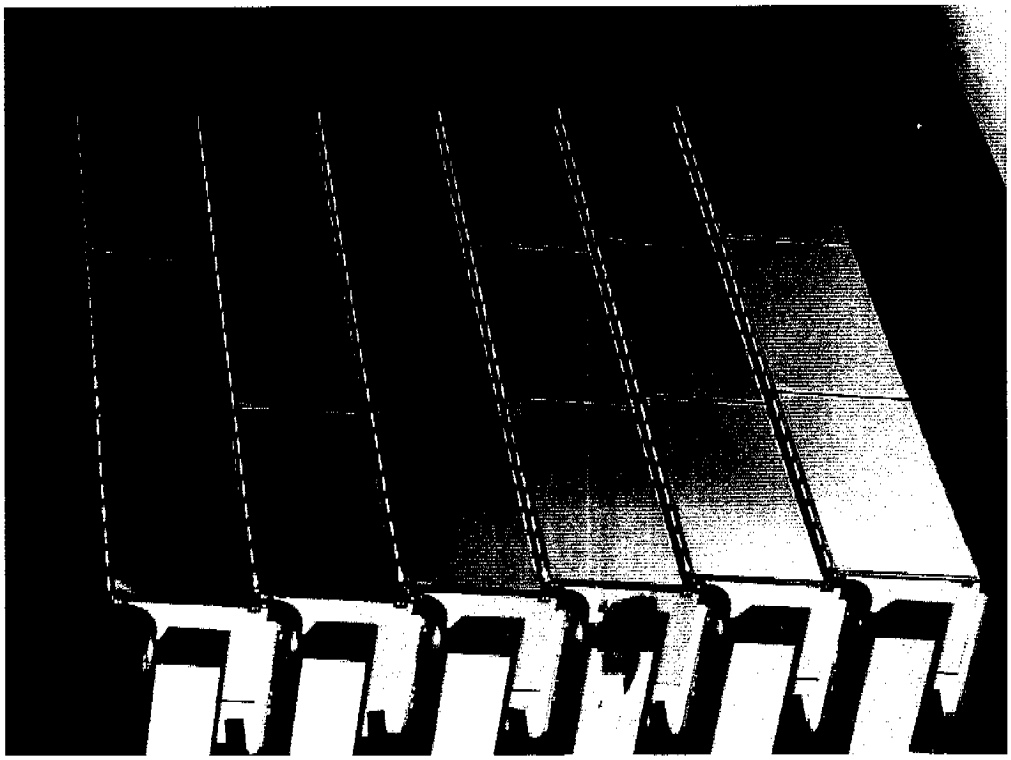

Figure 3.1: The PILATUS 1M detector. The sensitive surface of the detector is provided by 18 individual modules.

plate to allow an overlap of the modules.

One module consists of a hybrid silicon assembly and a module control board (MCB) shown in Figure 3.2a. The electronic board is bent by 90° and continues underneath the silicon assembly (Fig. 3.2b). The silicon assembly consists of a sensor, 16 readout chips and a silicon baseplate (Fig. 3.3a). Figure 3.3b shows the two rows of 8 chips; the sensor is on the back side.

3.1.1 Sensor

The monolithic high resistivity ($\approx$ 8 kΩcm) n–type silicon sensor has 366 $\times$ 156 pixels with a sensitive area of 79.4×34.1 mm^2. The back side of the n–type bulk material is structured with a regular array of 110×110 μm sized p^+ implants with a pitch of 217×217 μm (Fig. 3.4a). With a continuously high doped n^+ implant at the back side of the sensor, each pixel represents a p–n diode. The gaps between the readout chips, as seen in Figure 3.3b, are spanned with double sized pixels (Fig. 3.4b). At the corners, where four chips meet, quad sized pixels are required. The p–n diodes are reverse biased with a voltage of 100 V, provided by a single connection to the aluminized n^+ side (Fig. 3.7). The mechanical cutting of the sensors destroys the crystal lattice. The outermost pixels need therefore protection by guard rings, which are on ground potential (Fig. 3.4c). These guard rings are approximately 0.7 mm wide and enlarge the size of the sensor.

3.1.2 Bump Bonding

For each p^+ electrode and for the innermost guard ring indium balls are used as the electrical connection to the read–out electronic (Fig. 3.4d). The bump bonding technology used for the construction of the PILATUS 1M detector was developed and performed at PSI. The sensors are delivered with a thin UBM layer of Ti/Ni/Au on each p^+ electrode. A first photolithography step is performed which leaves each p^+ electrode with an opening in the applied photoresist layer. A thin layer of indium is then vacuum deposited onto the wafers. In a lift–off step, the photoresist is removed from the sensor, which leaves an indium cake of several microns thickness. On the CMOS chip a similar procedure is performed, leaving a thin UBM layer of Ti/Ni/Au and a thin indium layer on the pixel pads. The indium cakes on the sensor transform to spheres after reflowing the sensor in a reactive gas atmosphere at 180 °C (the melting point of indium is 154 °C). The balls have a diameter of $\sim$ 18 μm. Each chip is precisely positioned and pressed on the sensor with a force of $\sim$ 1 g/bump, which squeezes the balls to approximately 5 to 10 μm. After placing the 16 chips the complete assembly undergoes a second reflow process. The distance between chips and sensor increases to $\sim$ 15 μm. The chips are aligned with a precision of $\sim$ 1 μm with respect to the sensor and a well–bonded chip holds more than 500 g.

3.1.3 CMOS Chip

A CMOS chip (Fig. 3.5a) has 44 $\times$ 78 individual pixels of the same size as the sensor pixels. A pixel contains a low–noise, charge–sensitive amplifier, a comparator and a 15 bit digital counter and has the same architecture as described in section 2.3.2. A description of the detector is given in [32].

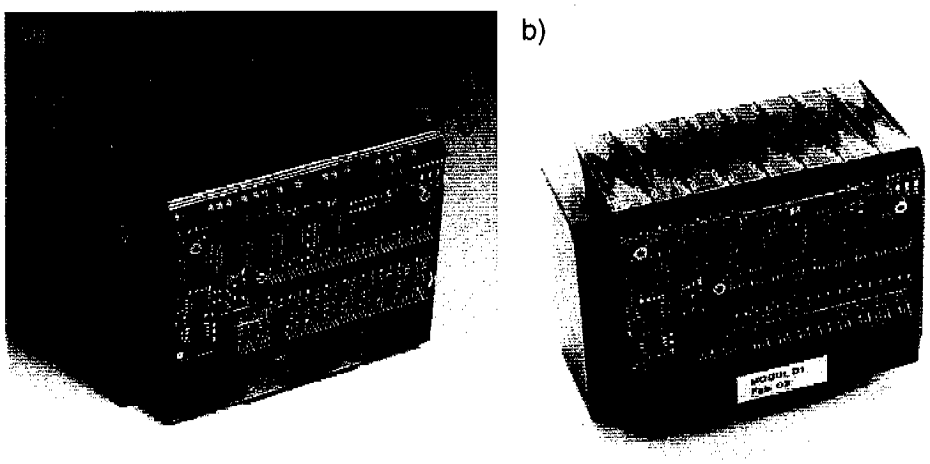

Figure 3.2: a) The fundamental unit of the PILATUS 1M detector is a module. b) Sensor and readout chips are directly mounted on the module control board.

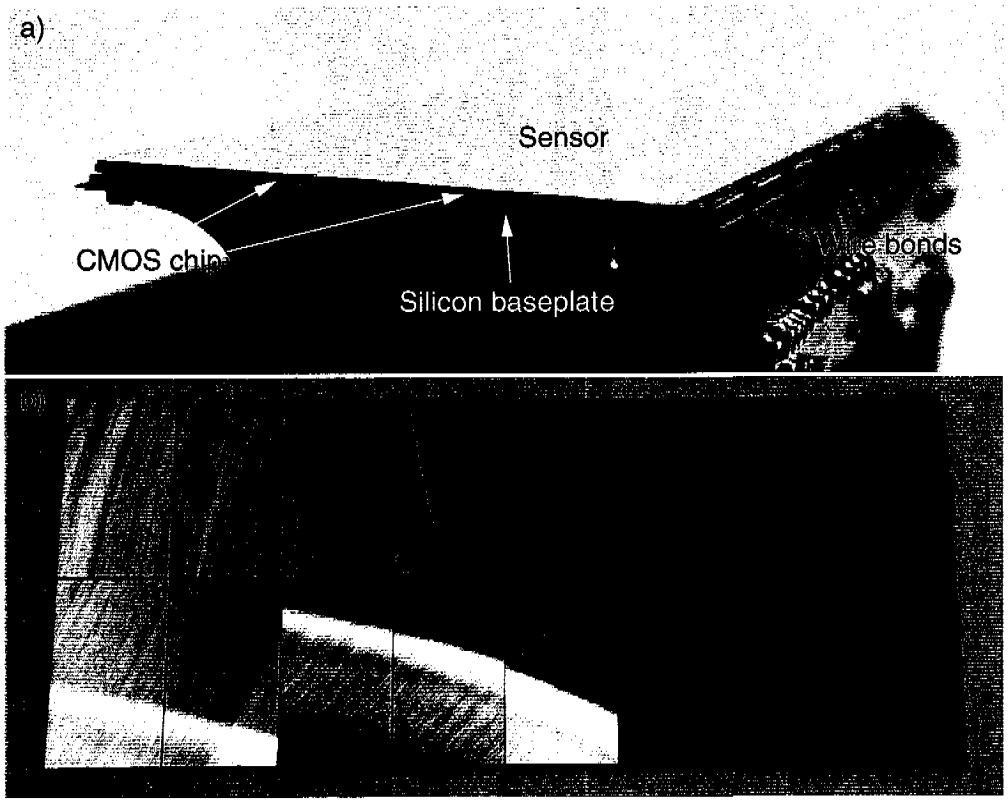

Figure 3.3: The silicon assembly on the top of each module. a) Beneath the sensor are the readout chips. A silicon baseplate adjusts to the different thermal expansions of silicon and aluminum (base). b) The readout chips of the silicon assembly. Between the 16 readout chips are small gaps.

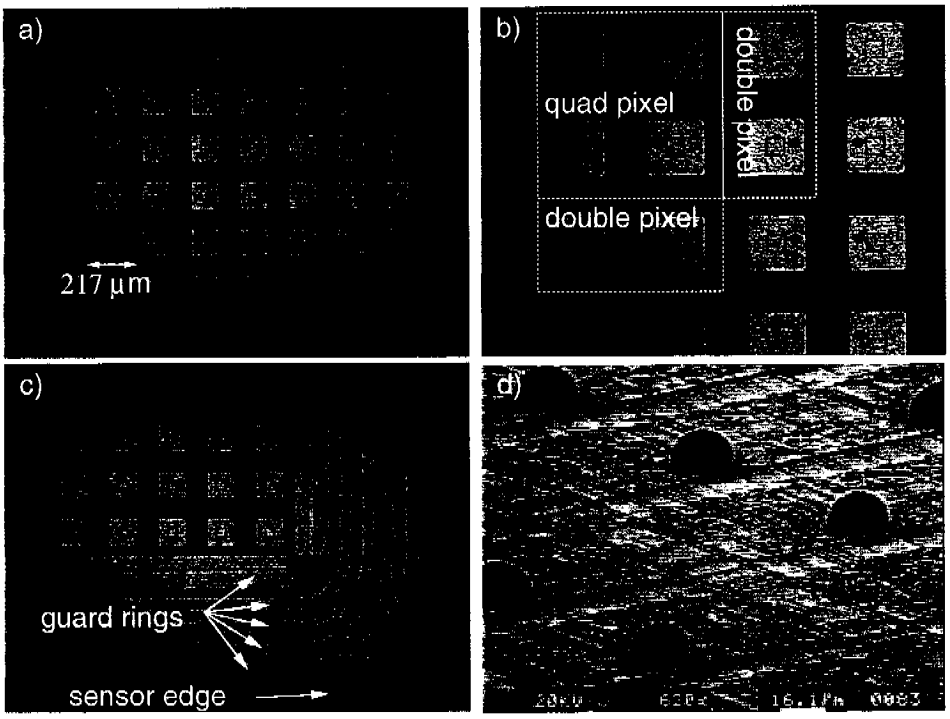

Figure 3.4: The p–side of the silicon sensor. a) The regular array of the p^+ implants has a pitch of 217×217 μm^2 and a size of 110×110 μm^2. b) The gap between the readout chips is spanned by double and quad sized pixels. c) Guard rings are required around the sensor. d) Each pixel diode and the innermost guard ring are electrically connected to the readout chips with small indium bump bonds.

Figure 3.5b shows the pixel electronics with the input pad followed by the analog part (amplifier and comparator). The digital part, i.e. the 15 bit counter, occupies most of the available space. The chip is selected by the CHSEL signal and the pixels by shift registers at the boundary of the chip which are controlled via ROWSEL and COLSEL (Fig. 2.14). A signal, arriving via the indium ball at the input pad, is amplified. The output of each amplifier can be monitored at the AOUT pad. A calibration pulse (CAL) can inject a certain amount of charge into the amplifier. The amount of injected charge dQ is calculated with equation 2.27, where dV is the calibration voltage and C is a 1.7 fF capacitor on the input of the amplifier. A $dV = 157$ mV calibrate signal corresponds to 1667 electrons injected into the amplifier. Comparing the AOUT voltage measured with the calibration pulse and with X–ray photons leads to a calibration of the electronics to the photon energy.

The lower threshold of the comparator is set by a global voltage and can be adjusted with a 4 bit DAC in each pixel, which is important to get a uniform threshold distribution across the whole CMOS chip. It is also possible to introduce an upper limit comparator though that was not implemented here. The procedure of adjusting the thresholds of all the pixels is called trimming.

The comparator creates a digital clock pulse for the counter which is designed as a pseudo random counter. It is an array of shift register with the advantage of a simple read–out and a small design. The disadvantage is that the pseudo random count number must be compared with a lookup table to reconstruct the real number of counts.

3.1.4 Radiation Tolerance, Chip Technology and Defects

As the readout chips are directly exposed to X–rays in hybrid pixel detector designs, a CMOS process or design must be used which tolerates this radiation. The flux of beamline X06SA of the SLS is more than 10^{11} γ/s for 12.4 keV photons and an electron beam current of 100 mA. The intensity is reduced by the absorption of the sample and air scattering. Diffraction images of proteins have on average 5000 Bragg reflections and most pixels receive low intensity background radiation. Therefore only 10 % of the pixels receive a significant X–ray rate. This rate is further reduced by the absorption of the silicon sensor. It can be approximated that a pixel receives a dose less than 0.1 rad/s. If the detector is used 8 h per day a dose of about 5 Mrad is accumulated in 5 years of operation.

As standard CMOS processes sustains approximately 0.2 Mrad, the chips were produced in the radiation tolerant DMILL process[1]. The chips were delivered on 6 inch wafers (Fig. 3.6) and the yield was approximately 37 %. Unfortunately on average 4.7 % of defective pixels were present on the selected chips. Additionally, the counter of the readout chip can switch into a random count state because of a subtle design fault. This effect depends on the counting rate on a pixel and occurs if two photons arrive in a short time interval. This interval is estimated from chip design simulations to be between 450 and 650 ns. Both types of defects influence strongly the accuracy of intensity measurements. Therefore procedures have been developed to work around these defects. These procedures will be discussed in section 5.2.

[1]Mixed analog/digital BiCMOS technology hardened to tolerate a combination of 10 Mrad and 10^{14} neutrons/cm^2

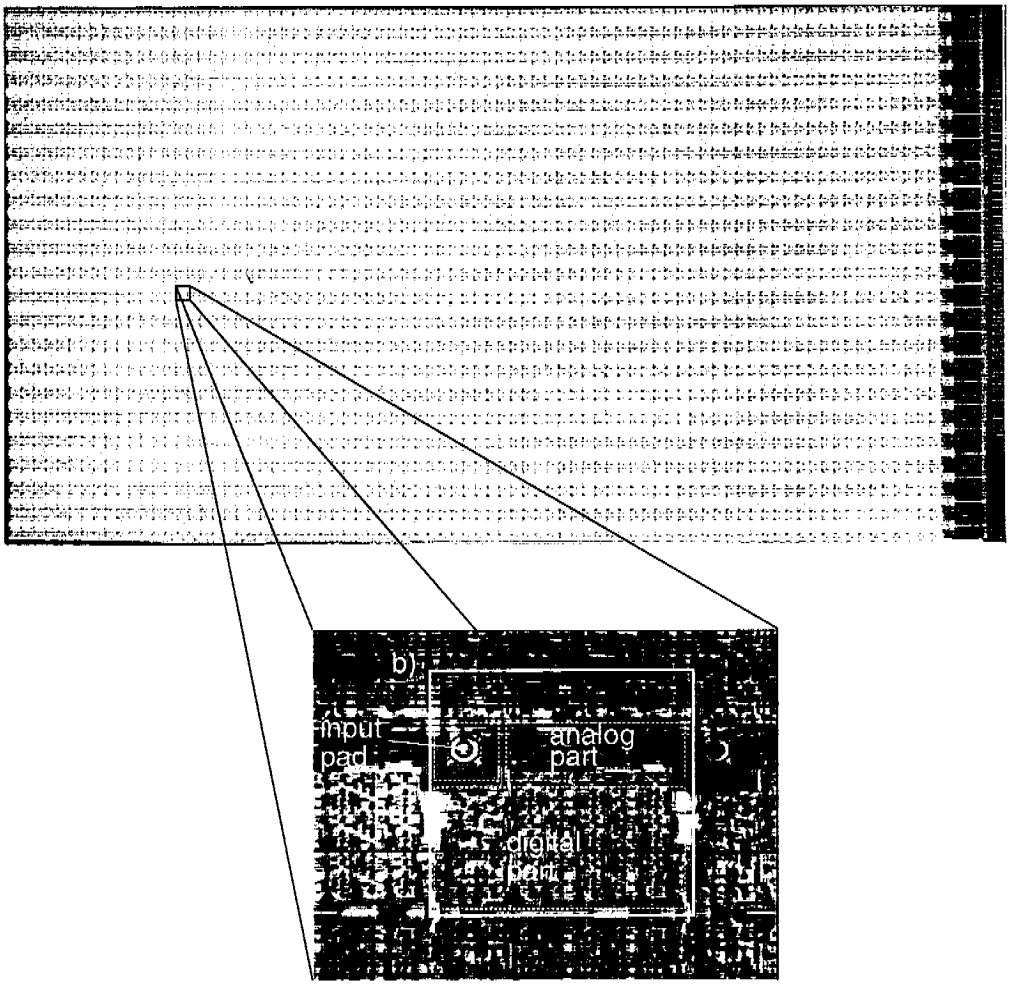

Figure 3.5: a) A CMOS chip with 44 × 78 independent pixels has a size of approximately 20 × 10 mm^2. On the right side of the chip are the column control and 42 wire bond pads. b) A magnification of a single pixel. The bump pad is followed by the analog part. Most of the pixel area is occupied by the 15–bit counter.

3.1.5 Detector Assembly

The electrical connection between the MCB and the silicon assembly is done with wire bonds. For each chip 42 connections are required. In Figure 3.7 the wire bond connections to a readout chip are shown. The two wire bonds to the sensor supply the bias voltage.

Although a module is continuously sensitive, the wirebond connections and the guard rings of the sensor prohibit an unbroken surface for the multi module PILATUS 1M detector. In addition a mechanical tolerance is required. The two inter–module gaps of 2.387 mm (11 pixels) in each bank are dominated by the width of the guard rings (approximately 2×0.6 mm). The large area required for the wire bond connections on the readout chip (Fig. 3.5) and on the MCB (Fig. 3.7) would lead to a gap between the banks of approximately 4.5 mm. This gap could be reduced to 1.085 mm (5 pixels) by an overlapping arrangement: the banks are tilted by 6° as seen in Figures 3.1 and 3.11. As a consequence of the overlap a shadow on the underlying modules occur, when the detector is illuminated by X–rays. Therefore the sensitive area of the detector is smaller than the total area mentioned above. The contributions to the insensitive area are the following (see also Fig. 4.4, page 55):

- Bump bond defects: Good bonded modules have only 0.05 % unconnected pixels on average. However, two modules turned out badly, resulting in an overall bump bond yield of 98.8 % for the detector.
- Pixel defects: Analog and digital defects of the readout chip lead to 4.7 % dead pixels, which is a result of the DMILL process.
- Chip defects: 16 (5 %) of the 288 readout chips are not responding. Five chips in one module (Fig. 4.4, top–right) are from an unsuccessfully processed wafer, 8 were destroyed during wirebonding (6 in the top–left module) and 3 during the bump bonding process.
- Insensitive areas between modules: The horizontal and vertical gaps add to a total of 48822 pixels (4.4 %).
- Shadow of the module periphery: The shadow depends on the geometry of the experiment. With the detector at 1 m distance and the detector center being equal to the central beam direction, 25000 pixels are shadowed (2.4 %).

Altogether, the sensitive area is 82.3 % of the detector area at the mentioned experimental geometry.

The total power consumption of the detector is approximately 300 W. To prevent overheating the modules are cooled with water (15° C), which circulates through the aluminum base plate (Fig. 3.11). The sensors of the detector must be protected from visible light. X–rays can enter the detector through an aluminized mylar sheet (Fig. 3.8). To prevent condensation on the electronics, nitrogen gas constantly flows through the detector (3 to 4 l/h).

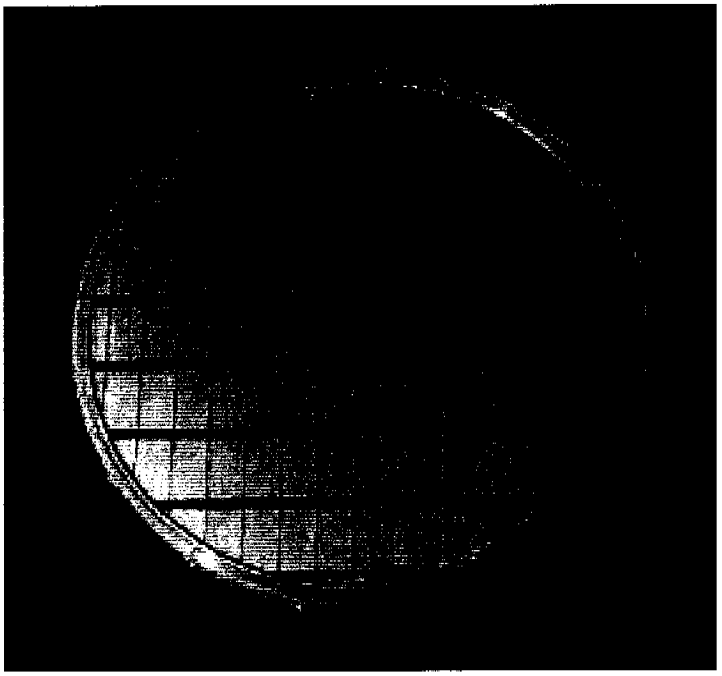

Figure 3.6: A six inch wafer with 66 CMOS chips.

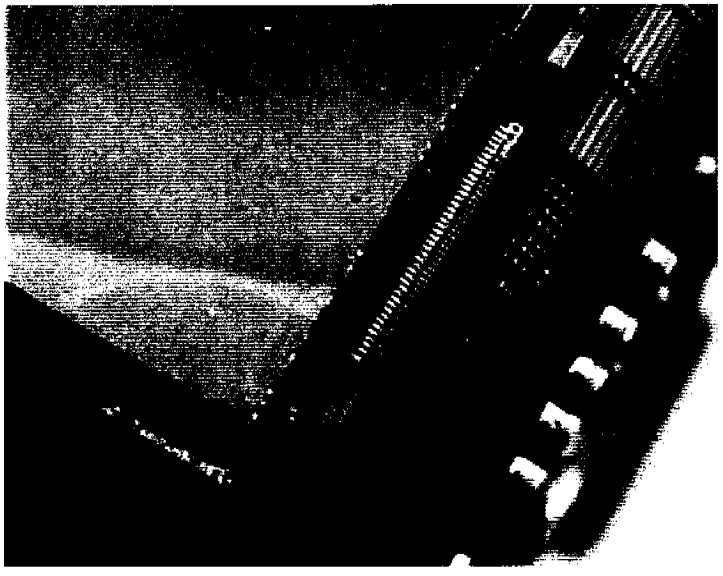

Figure 3.7: The control signals and power connections are provided by wire bonds from the MCB to each readout chip. The two long wires to the sensor corner supply the bias voltage.

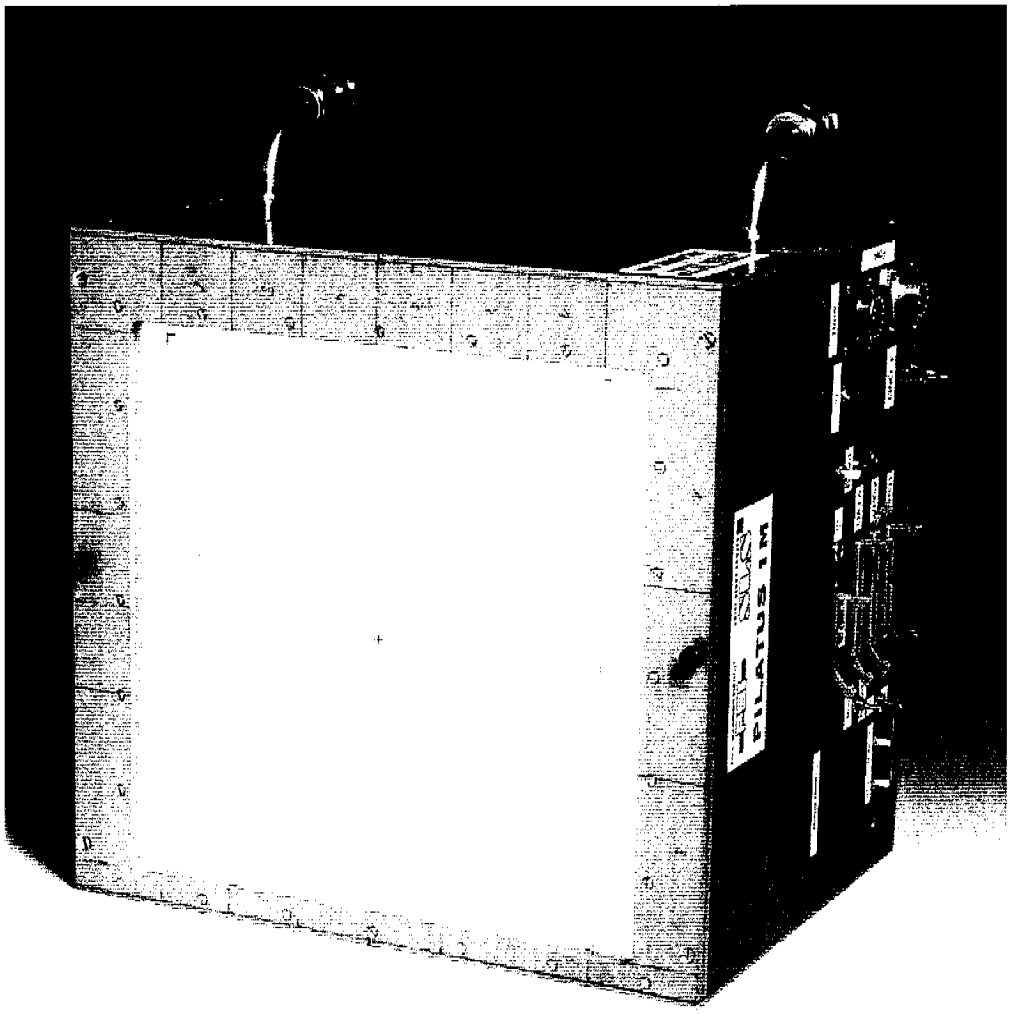

Figure 3.8: The PILATUS 1M detector. X–rays enter the detector through an aluminized mylar sheet. The power and control cable connections can be seen on the side of the detector frame. The water connections for cooling of the central base plate can be seen on the top of the detector.

3.2 Detector Control

The PILATUS 1M detector has three basic modes of operation:

- Calibration/Debug mode
- Counting mode
- Readout mode

The calibration mode is used for adjusting the amplifier and comparator settings. If no pixel is selected, the detector can be set to the counting mode by a global EN signal. All digital counters register the events passing the comparator. After the exposure time the EN signal is set to zero. The following read–out sequence is controlled by several electronic circuit boards.

3.2.1 Read–out Sequence

In the read–out sequence each pixel is selected and the data is clocked out. The data passes through the MCB and is stored in an intermediate storage memory (FIFO). The 3432 counters in each chip are read–out serially and all chips of the detector are read–out in parallel. Therefore the read–out time of the detector is equal to the read–out time of a single chip. With a read–out clock speed of 10 MHz the read–out time is

$$\underbrace{\frac{(78 \cdot 44)\ \text{pixel} \cdot 15\ \text{bit}}{10\ \text{MHz}}}_{\text{counter read–out}} + \underbrace{\frac{2 \cdot [78 \cdot (44+2) + 78]}{10\ \text{MHz}}}_{\text{row and column–control}} = 5.148 + 0.733\ \text{ms} = 5.881\ \text{ms}\ .$$

The row and column–control requires the additional clock cycles for pixel selection and control commands in the read–out pattern. For an exposure time of 600 ms the oscilloscope reading of the read–out cycle is shown in Figure 3.9. After the read–out time all pixels are deselected and, using the EN signal, a new exposure can be started.

During this new exposure and after the transfer of the data to the FIFO memory, the data is read–out serially to the data acquisition computer. This data stream is serial to parallel converted and the count number is retrieved using a lookup table. Finally the image is assembled and written to a computer disk. The time until the data is transferred from the FIFO memory to computer disk is approximately 600 ms. With the read–out time of 5.88 ms this leads to a maximal frame rate of 1.65 Hz for this setup.

3.2.2 Hardware

A diagram of the control architecture is shown in Figure 3.10 and the arrangement of the electronic boards can be seen in the photographs of the open detector in Figure 3.11. The three MCBs of the modules of one bank are serviced by a bank control board (BCB) mounted on the bottom part of the detector (Fig. 3.11a). The connections pass through holes in the central base plate. The six BCBs are connected to a single detector control board (DCB). The data stored in the FIFOs of the BCBs is transferred via the DCB and a PCI interface (model PCI110k–PRODB, PLD Applications, F–13120 Aix–en–Provence) to the computer disk.

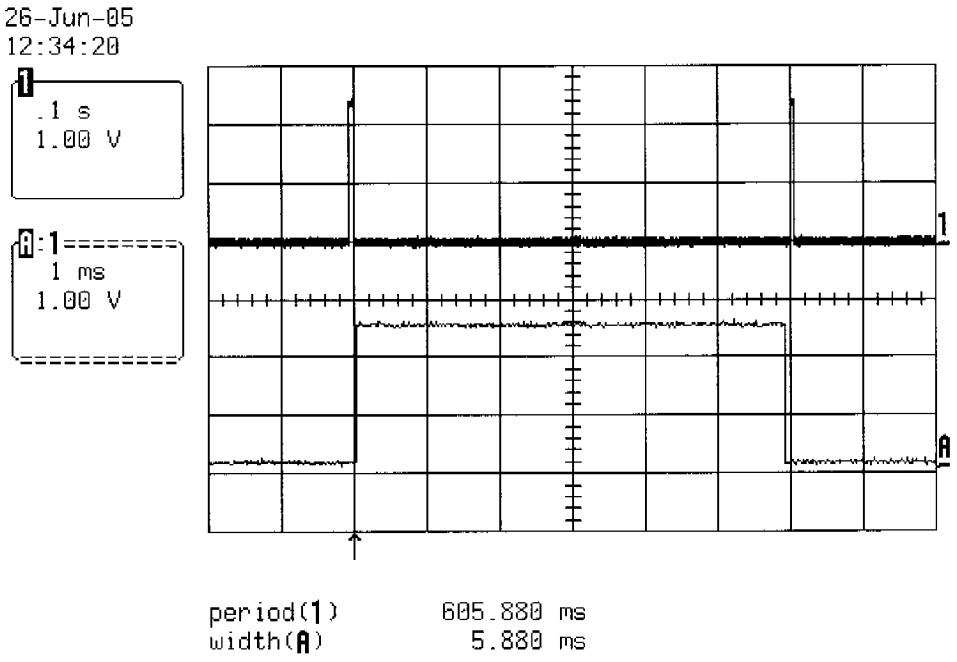

Figure 3.9: Oscilloscope reading from the read–out cycle with an exposure time of 600 ms (line 1). After the read–out sequence of 5.88 ms (zoom: line A) a new image can be recorded, leading to a frame period of 605.88 ms.

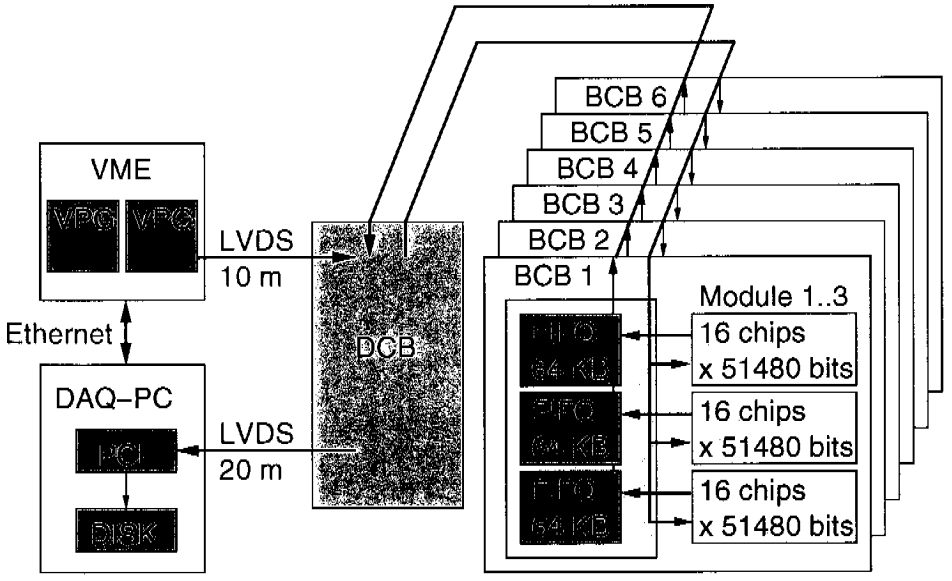

Figure 3.10: Block diagram of the control architecture of the detector.

The control patterns for the detector are sent from the computer to an Input/Output Controller (IOC) which controls two VME pattern generators (model VPG517; Dipl.-Ing. Kramert GmbH, Remigen, Switzerland). The control sequences are preloaded and started on request. The VPG then sends the control signals via LVDS cables to the DCB, where the signals are distributed via the BCBs and MCBs to the CMOS chips.

Power from external power supplies is distributed to each module and electronic circuit board by a detector power board (DPB, mounted perpendicular to the banks).

3.2.3 Software

The detector is controlled by the program `camserver` which communicates with the IOC and the PCI interface. The program is used as a socket for the user interface called `tvx`. This program sends commands to the `camserver` and is used for image visualization, data correction and data analysis. These programs, `camserver` and `tvx`, are an open source project of Dr. Eric F. Eikenberry et al.

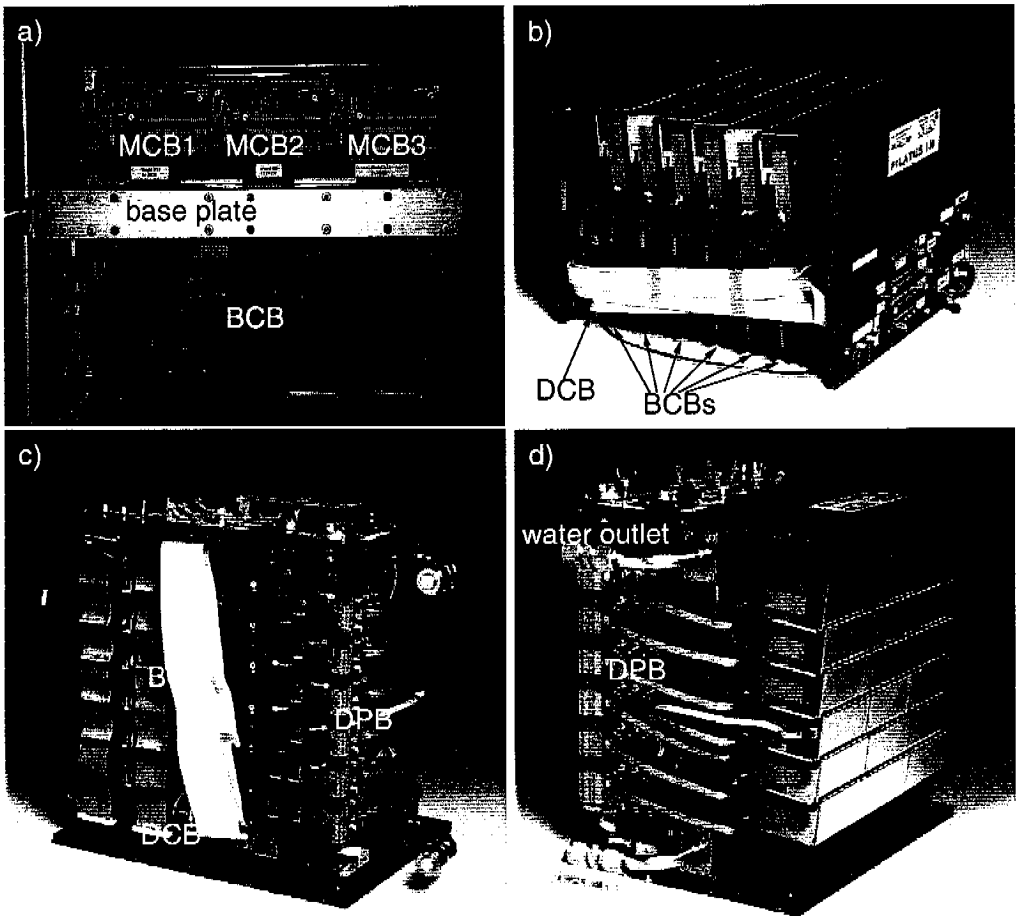

Figure 3.11: The open PILATUS 1M detector viewed from different sides. a) and b) Three MCBs of one bank are connected through the central base plate to the BCB which carries three intermediate FIFO memories. c) Six BCBs fill the bottom part of the detector and are controlled by the 7^{th} board (DCB), parallel to the BCBs. d) Power is distributed by the DPB. The central base plate is water cooled.

Chapter 4

Calibration of the PILATUS 1M Detector

The purpose of an area X–ray detector is to measure the incident dose at each position on the entrance window to the device. Ideally, this would just be the photon count at each position, but real detectors present a more complex situation. The PILATUS 1M detector is therefore calibrated to remove the effects of individual pixel response and spatial image distortions.

By calibrating the detector, first the pixel electronics is adjusted in such a way that the thresholds of all pixels correspond to the same energy. Second, the response of each pixel is measured and compared to the calculated photon count at the sensor surface. The difference is adjusted in a so called *flatfield* correction. Finally, the spatial distortions are corrected.

The first step after assembling the PILATUS 1M detector is to adjust the gains and shaping times of the amplifiers. This has been described in [34] for the prototype chip SLS04, the precursor of the SLS06 (PILATUS I) chip of the PILATUS 1M detector. In the calibration mode the CAL–signal feeds a certain amount of charge into the amplifier of a pixel (section 3.1.3). The amplifier output (AOUT) is monitored and calibrated to the X–ray photon energy.

By varying the voltage of the CAL pulse, different photon energies of X–rays are simulated. With this method the threshold of each pixel can be trimmed.

4.1 Threshold Equalization Procedure

The untrimmed detector has a wide threshold distribution, caused by differences in the transistor characteristics for different pixels. A CMOS process is normally used for digital circuits where the matching between transistors is not important. Thus, in the analog part of the chip, a significant variation of the amplifier gain between different pixels is observed.

The threshold of the detector is set below the X–ray energy used in the experiment. It has been shown that charge sharing effects can be successfully minimized by setting the threshold to half of the photon energy [18, 31]. The threshold of the comparator in each pixel is composed of a global threshold voltage, V_{comp}, plus individual voltages set by the 4 bit DACs in each pixel. V_{comp} is set in such a way that all pixels can fully count at the threshold target, e.g. $E_{\mathrm{ph}}/2$. While increasing the trim DAC value from 0 to 2^4, 16 images are acquired. For each image, 100 CAL pulses are given to the pixels. The correct DAC value of a pixel fulfills the condition that half of the CAL pulses pass the comparator. These DAC values are stored in a file, to be loaded and latched into each pixel. This takes approximately 15 min for the entire detector.

The threshold distribution can be measured by scanning the CAL pulse height. Figure 4.1 shows the number of pixels as a function of their individual threshold value for different threshold targets. The wide distribution with a standard deviation σ_0 is significantly narrowed (σ_1) after loading the trim values in the comparator DAC. The standard deviations σ_0 and σ_1 are listed in Table 4.1.

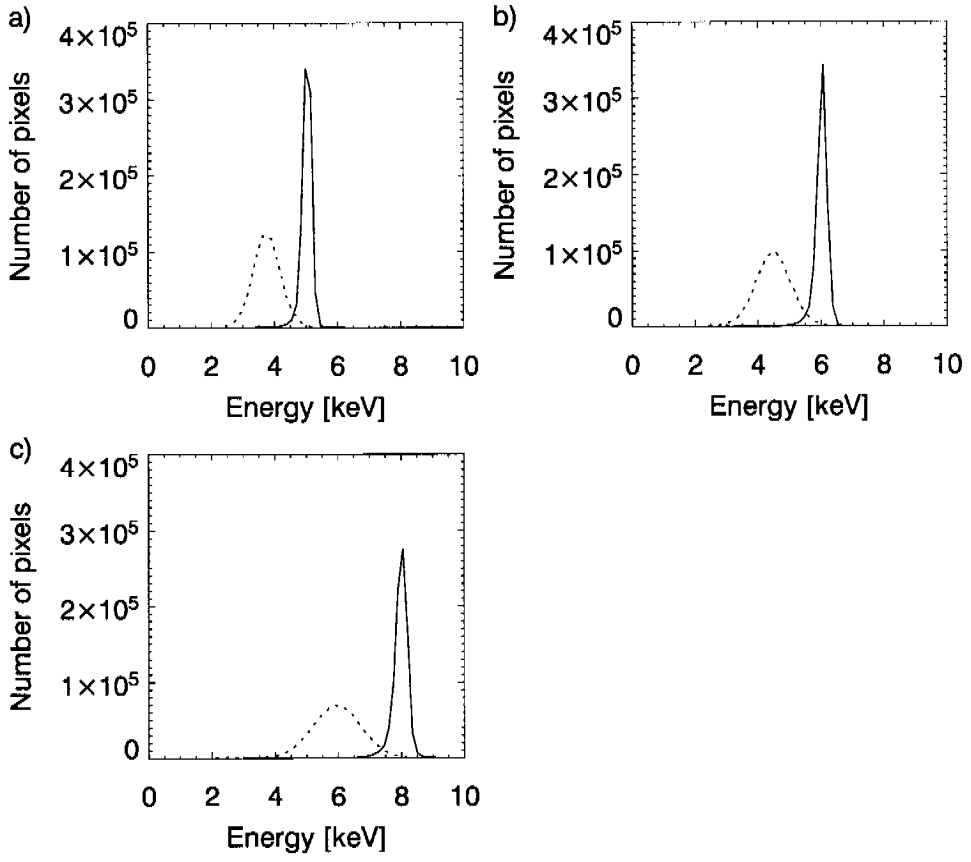

Figure 4.1: The histogram of the threshold values of all pixels of the PILATUS 1M detector trimmed to: a) 5 keV, b) 6 keV, c) 8 keV. The wide untrimmed threshold distribution (dotted line) can be narrowed by trimming the threshold of the comparators (solid line). The standard deviations of the distribution are listed in table 4.1.

Threshold target [keV]	σ_0 [keV]	σ_1 [keV]
5	0.427	0.138
6	0.546	0.148
8	0.766	0.181

Table 4.1: Standard deviations of the untrimmed (σ_0) and trimmed (σ_1) threshold distribution shown in Figure 4.1.

4.2 Flatfield Calibration

After the threshold adjustment each pixel still has an individual response to X–rays. This variation has its origins in the residual threshold variation, the quality of the bump bond connection and the sensor itself. This variation is measured and adjusted with a flatfield correction (some times also called 'floodfield' correction). In this procedure the actual field of illumination at the detector surface is reconstructed.

4.2.1 Experiment

The flatfield illumination of the PILATUS 1M detector was performed at the synchrotron beamline X06SA of the SLS. The experimental setup can be seen in Figure 4.2. The field of illumination should have no inhomogeneity and monochromatic photons are required. Scattering of mechanical parts can be the cause for patterns in the flatfield image. The best place for the detector is 90° with respect to the central beam direction.

A capillary filled with a solution of Br^- ions is excited with the very intense X–ray beam. With a photon energy above the K $1s$ edge of Bromide (13.474 keV) fluorescent X–rays are emitted from the solution. The energy of the X–rays is 11.9 keV ($K\alpha_1$ and $K\alpha_2$). The density of the Br^- in the solution is a compromise between two opposing facts: most of the incoming photons should excite the bromine atoms but most of the fluorescent light should also escape the capillary. Therefore a saturated solution was mixed with water at a ratio of 1:1 and filled

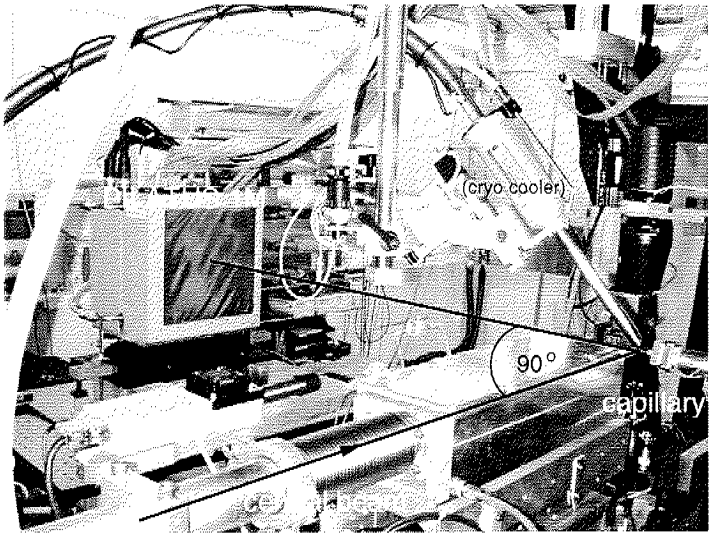

Figure 4.2: The experimental setup for flatfield calibration at the protein crystallography beamline X06SA of the SLS. The detector is placed 90° in respect to the central beam direction and is illuminated with fluorescence X–rays from the capillary filled with a Br^- solution. The displayed distance d for the flatfield measurement is adjusted to the distance used for crystallographic experiment. In the protein crystallography experiments the prominent cryo–cooler is used.

into the capillary.

For good homogeneous flatfield measurements the distance d of the detector to the X–ray source should be very long. But the special geometry of the PILATUS 1M detector requires d to be identical to the distance later used in crystallographic experiments. The reason for this is the overlap of the modules. The shadow created on the underlying module changes with the distance. Furthermore, the absorption in silicon depends on the path length of the X–rays in the material and is thus dependent on the angle of incidence. The reconstruction of the flatfield at the detector surface therefore depends on the geometry of the experiment.

The exposure time was adjusted so that about $5 \cdot 10^3$ γ/pixel were collected in one exposure. This ensures that even the quad–sized pixels between chips do not reach their maximum count state. For good statistics 10^5 counts are necessary. Therefore at least $n = 20$ images were recorded.

4.2.2 Calculation

The flatfield algorithm calculates the theoretical field of illumination at the detector surface for a given experimental setup and compares it with a recorded flatfield image of the detector. Therefore flatfield images of high quality must be provided. Furthermore the position of the central pixel (x_0, y_0), the distance d and the air absorption factor α for the used energy must be given to the algorithm.

From n independent flatfield exposures an average intensity I_{ij} was calculated for each pixel P_{ij}. These values are stored in the input flatfield image, F_0. In the raw images, counting errors are located and set to zero in the image. Although counting errors can have any value, they can be detected if a pixel is not counting within a narrow range around the average intensity I. This range is chosen by manual inspection and is approximately $\pm 3\sigma_I$. A pixel P_{ij}, not counting $n - \epsilon$ times within this range, is marked as *untrusted* and deleted from the input flatfield image ($I_{ij} = 0$). Again, manual inspection is used to determine the value of ϵ (typically 2 if $n = 20$).

The first step is to calculate the path length in air, r_{ij}, and the angle of incidence on the detector, θ, for each pixel P_{ij} at the position x_i, y_j (Fig. 4.3):

$$r_{ij} = d^2 + l_{ij}^2 \,, \tag{4.1}$$

$$\cos\theta = \frac{d}{r_{ij}} \,, \tag{4.2}$$

where l_{ij} is the distance of pixel P_{ij} from the center (x_0, y_0) and can be calculated as

$$l_{ij} = \sqrt{(x_i - x_0)^2 + (y_i - y_0)^2} \,. \tag{4.3}$$

First, X–ray absorption in air reduces the incident intensity at position x_i, y_j:

$$I \propto e^{-\alpha r_{ij}} = e^{\frac{-\alpha d}{\cos\theta}} \,, \tag{4.4}$$

with α being the air absorption coefficient. Second, the $1/r^2$ falloff in intensity reduces the number of photons collected from pixel P_{ij}:

$$I \propto \frac{1}{r_{ij}^2} = \frac{\cos^2\theta}{d^2} \,. \tag{4.5}$$

Third, the apparent size of the pixel p' depends on the angle of incidence and the pixel size p as

$$p' = p \cos\theta \,. \tag{4.6}$$

The intensity is proportional to the pixel size and is therefore

$$I \propto \cos\theta \,. \tag{4.7}$$

With the three equations 4.4, 4.5 and 4.7 the theoretically received intensity from pixel P_{ij} is then

$$I_{ij}^{theo} = I_0 \, e^{\frac{-\alpha d}{\cos\theta}} \, \cos^3\theta \,. \tag{4.8}$$

The scaling factor I_0 is the intensity at the center x_0, y_0 of the detector surface and is calculated from the highest detector response in this central region. The quantum efficiency of the sensor is taken into account. Thus, flatfield corrected images have a higher intensity than uncorrected images. The correction factors F_{ij} are calculated using:

$$F_{ij} = \frac{I_{ij}^{theo}}{I_{ij}} \,. \tag{4.9}$$

The measured intensity in each pixel P_{ij} is then multiplied with its correction factor F_{ij} and thus inhomogeneities of the different pixel responses are adjusted. The precision of the correction factors should be around 1 %.

The described procedure has been developed for CCD X–ray detectors [35]. It can also be applied to the pixel detector but its specific properties have to be considered: first the detector surface is not flat. Therefore the angle of incidence depends on the module tilt. In addition, the quantum efficiency of the silicon sensor depends on the angle of incidence. The flatfield correction of the PILATUS 1M detector depends thus on the experimental geometry, namely the

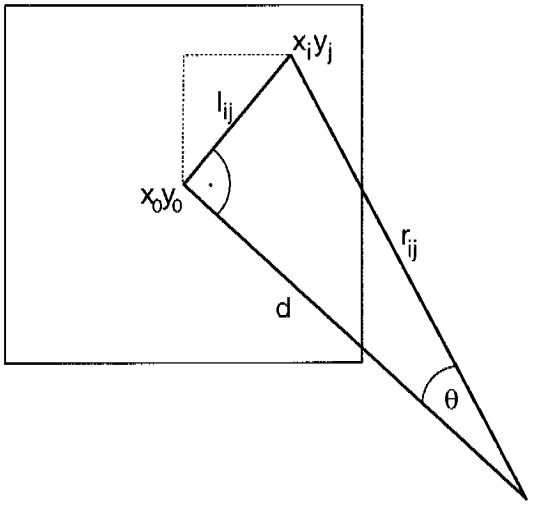

Figure 4.3: Calculation of the theoretical flatfield response of the detector. The shortest distance from the capillary to the detector surface d (normal to the surface) defines the central pixel at position x_0, y_0.

distance, the center position and the detector misalignment. The quality of the flatfield correction depends therefore on the precision of the detector mounting for the flatfield measurement and the crystallographic experiment.

4.2.3 Results

An uncorrected image is shown in Figure 4.4. The center of the field is near the center of the detector. The distance to the fluorescent sample was 130 mm. The gaps and shadows between the modules can be seen together with the dead chips (rectangular white regions). Visible counting errors of high count state are the randomly distributed black pixels, whereas the white pixels (zero count) are permanently dead pixels. The $1/r^2$ law dominates the appearance of the image. The center module of the bottom bank shows a large inhomogeneity. Irregular shaped white regions correspond to bad bump bonded areas.

The flatfield image F_0 (described in the previous section) was produced and used for the calculation of the flatfield correction file F_{ij}. For the analysis a *flat* image F_1 was calculated from F_0, i.e. the pixel values were normalized to a theoretical intensity without $1/r^2$ falloff, air absorption and apparent pixel size variation (using equation 4.8). The histogram of the intensity distribution of image F_1 is shown in Figure 4.5. Long tails can be seen on the left and right side of the histogram, corresponding to a large number of pixels counting much less or much more than the average pixel. A randomly chosen flatfield image was corrected, using the correction file F_{ij}. From this flatfield corrected image a *flat* image F_2 was calculated and in the histogram no tails can be seen (Fig. 4.5). For both histograms the mean intensities and standard deviations were calculated. As the flatfield correction reconstructs the field of illumination on the sensor surface, the mean intensity is increased from 1999 to 2666 counts due to the silicon absorption correction (scaling factor I_0). The standard deviation of the intensity distribution could be reduced from 90 for image F_1 to 63 for the flatfield corrected image F_2.

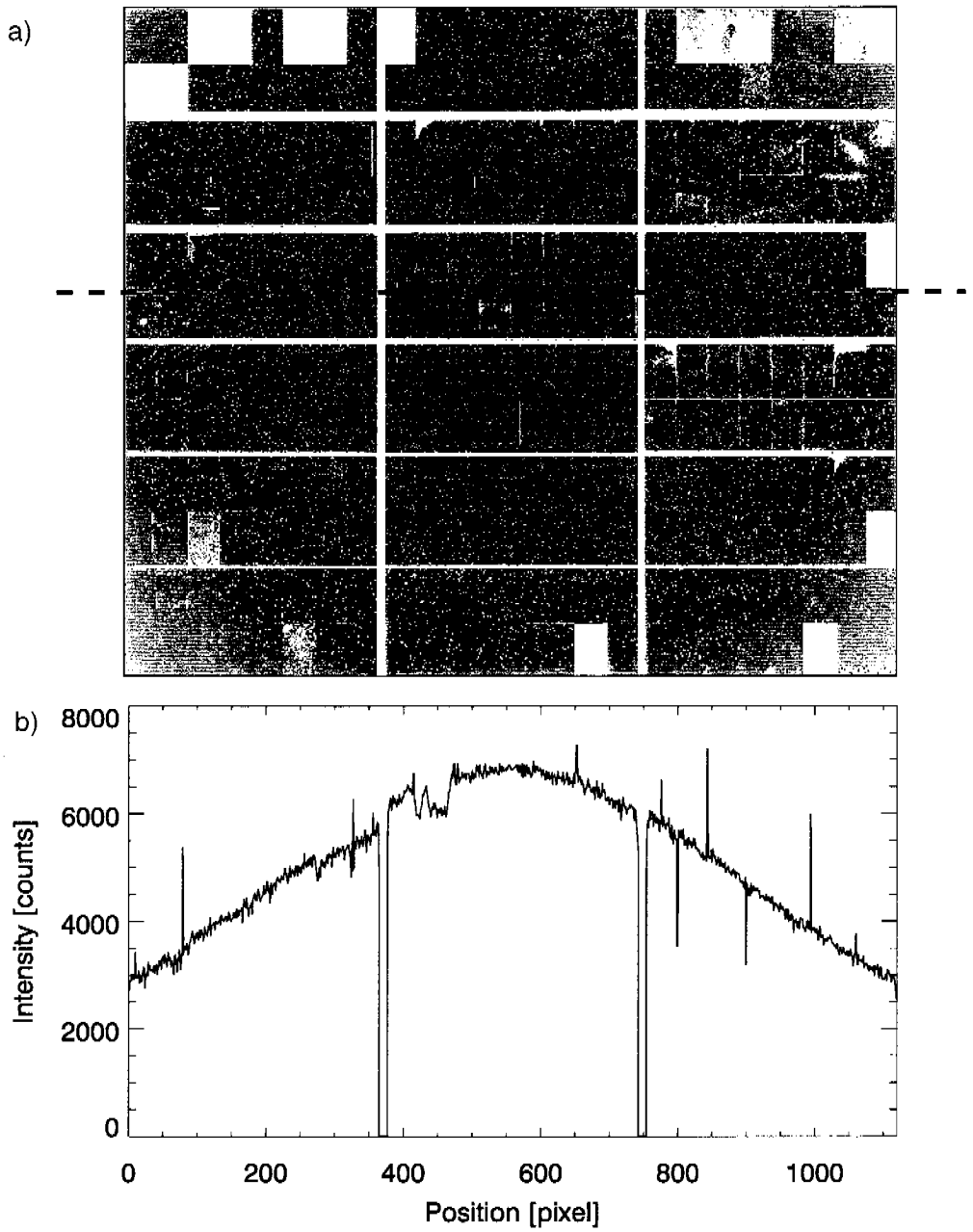

Figure 4.4: A flatfield raw image (a) and a single pixel wide cross section along the dotted line (b). The intensity distribution is dominated by the $1/r^2$ falloff. Between modules within a bank are two identical constant insensitive areas. The inter–bank spacing depend also on the shadow caused by the overlapping modules. The pixels with zero count are excluded in integration of Figure 4.4b. For more explanations of the visible detector defects see text.

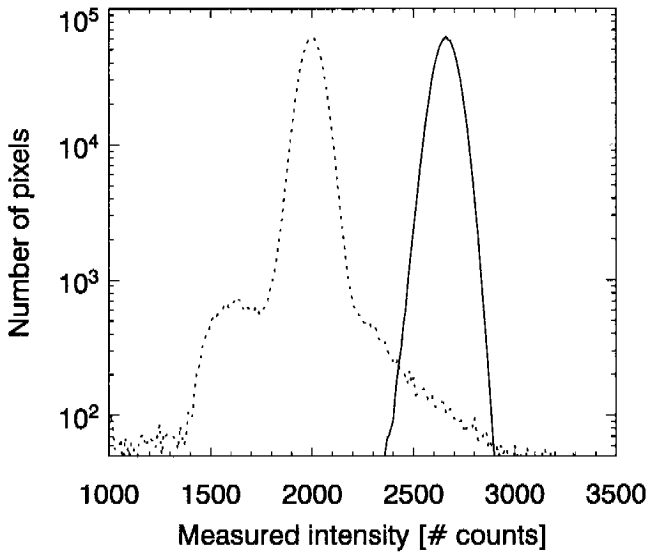

Figure 4.5: A histogram of an exposured image before and after flatfield correction on a logarithmic scale. The long tails of the uncorrected flatfield image (dotted line) is adjusted with the flatfield correction (solid line).

4.3 Distortion Calibration of the PILATUS 1M Detector

G. Hülsen, Ch. Brönnimann and E.F. Eikenberry, *Nucl. Instrum. Meth. A*, 548:540–554

Spatial image distortions are present in most imaging devices. For the calibration of the PILATUS 1M detector three sources of image distortions were analyzed. The parallax effect distorts the image within one module. The mechanical deviations of the modules from their assumed positions introduce another spatial error. The largest contribution to the distortion comes from the 6° tilt of the banks.

After quantifying the distortions an algorithm was developed to generate correction files. As the distortion of the PILATUS 1M detector is discontinuous, procedures developed for CCD detectors could not be used. But the correction file has the same format as the ones generated for CCD detectors. Therefore images could be corrected using an adapted algorithm from CCD detector systems.

The quality of the spatial distortion correction was experimentally quantified. Images of a metal mask show the remaining distortion. Spatial distortions can furthermore be visualized by measurements of powder diffraction rings. Finally, processing software for protein crystallography data calculates the spatial deviation of Bragg reflections from their assumed positions, which will be discussed in see section 5.3.

Available online at www.sciencedirect.com
SCIENCE DIRECT®
ELSEVIER
Nuclear Instruments and Methods in Physics Research A 548 (2005) 540–554
NUCLEAR INSTRUMENTS & METHODS IN PHYSICS RESEARCH Section A
www.elsevier.com/locate/nima

Distortion calibration of the PILATUS 1M detector

G. Hülsen*, Ch. Brönnimann, E.F. Eikenberry

Paul Scherrer Institut, CH-5232 Villigen-PSI, Switzerland

Received 10 May 2005; received in revised form 20 May 2005; accepted 23 May 2005
Available online 22 June 2005

Abstract

The PILATUS 1M detector is a large area tiled X-ray detector for protein crystallography. One million 217 × 217 μm^2 pixels cover an area of 24.3 × 20.0 cm^2 with 300 μm thick silicon sensors. The readout electronics enable single photon counting and a readout time of 6.7 ms. Images from this detector are spatially distorted by the influence of three factors. First, the absorption properties of the silicon leads to parallax broadening by a fraction of a pixel, depending on the angle of incidence and the photon energy. A simulation was compared to experimental data. Second, the modular architecture causes a mechanical displacement of the modules from their assumed positions. The modules are positioned on average to a precision of ~300 μm. Third, to reduce the dead area the modules are tilted by 6° and are overlapped. This introduces large distortions of several pixels which depend on the sample to detector distance.

An algorithm for distortion correction of CCD detector data was adapted to correct the data of the PILATUS 1M detector. The results of the metrology as well as the parallax shift were incorporated in these corrections. Images from a Ta-mask were used to test the corrections and quantify the remaining spatial distortion. The mask images were also used to refine the individual module positions. In order to verify the distortion corrections crystallographic standards were used. The result is that images of the detector can be spatially corrected to a precision of 74 μm or about 0.34 pixel.
© 2005 Elsevier B.V. All rights reserved.

PACS: 07.85.Fv; 07.85.Qe; 61.10.Nz

Keywords: Pixel detector; Distortion; Correction; Parallax

1. Introduction

Macromolecular crystallography is currently one of the largest applications using synchrotron X-ray sources. With this experimental technique the structure of thousands of proteins, viruses, nucleic acids, enzymes, energy transduction complexes and molecular motors have been solved. As the quality of both the X-ray sources and the experimental techniques has improved in the last years, the expectations of X-ray detection devices have increased. The latter are the limiting factors in crystallographic data collection to date.

*Corresponding author.
E-mail address: gregor.huelsen@psi.ch (G. Hülsen).

0168-9002/$ - see front matter © 2005 Elsevier B.V. All rights reserved.
doi:10.1016/j.nima.2005.05.032

The most important detector properties for these experiments are large sensitive area, wide dynamic range, good detective quantum efficiency, small point spread function and fast readout. Hybrid pixel detectors developed for modern high energy physics experiments [1–3] could meet the demands of macromolecular crystallographic experiments. This technology features a two-dimensional array of pn-diodes connected to a readout chip, which is designed in the latest CMOS technology. The PILATUS 1M detector is a hybrid modular pixel detector [4], designed for the protein crystallography beamline X06SA of the Swiss Light Source (SLS) at the Paul Scherrer Institute (Villigen–PSI, Switzerland).

The PILATUS 1M detector reduces the experimental time and enhances the quality of measurements. But like other large area detectors the data of this detector are spatially distorted. This paper describes the spatial calibration of the detector. The origins of the distortion are described, studied and quantified. Calibration routines developed for CCD cameras have been adapted for the PILATUS 1M detector. The module positions could be refined experimentally and the distortion of the corrected images was measured with a Ta-mask and crystallographic standards.

2. Origins of distortion in the PILATUS 1M detector

The modular architecture of the PILATUS 1M detector has been described in Refs. [4,5]. The fundamental unit is a module, consisting of a single $80.82 \times 35.47\,mm^2$ silicon sensor bump-bonded to 16 readout chips. The monolithic sensor (n-type, resistivity $\approx 8\,k\Omega cm$) has no dead area; double-size pixels span the gaps between the readout chips. A chip contains $44 \times 78 = 3432$ pixels each with a size of $217 \times 217\,\mu m^2$. In the CMOS chip each pixel has a low noise amplifier, a comparator for defining the minimum energy threshold and a digital counter. This permits single-photon counting at energies even below 6 keV [6]. The readout time for one image is 6.7 ms. The chips are fabricated in the radiation tolerant DMILL CMOS process. The disadvantage of this process is that the readout chips have, on average, 5% defective pixels. In addition, pixels can miscount at high rates.

The PILATUS 1M detector is assembled as shown in Fig. 1. The 18 modules provide an active area of $24.3 \times 20.0\,cm^2$. Three modules constitute one bank, the surface of which is tilted by 6° to the mounting frame. This allows overlapping the modules, which should reduce the dead area. The dead area is caused by the periphery of the module, which consists of the guard ring around the sensor and the wirebond connections from the chips to the readout electronics (Fig. 1). The two inter-module gaps in each bank are 2.387 mm wide (11 pixels) and the vertical spacing between the banks was reduced to 1.085 mm (5 pixels) by the overlapping arrangement. In total the gaps reduce the effective area by 4.5%. A consequence of the overlap is a shadow on the underlying modules when the detector is illuminated by X-rays. The area affected by the shadow depends on the experimental setup (Section 4.2).

Within one module the pixel positions are accurate to sub-micron precision because the sensor is fabricated by photolithographic processes. Therefore, there is no appreciable geometrical distortion

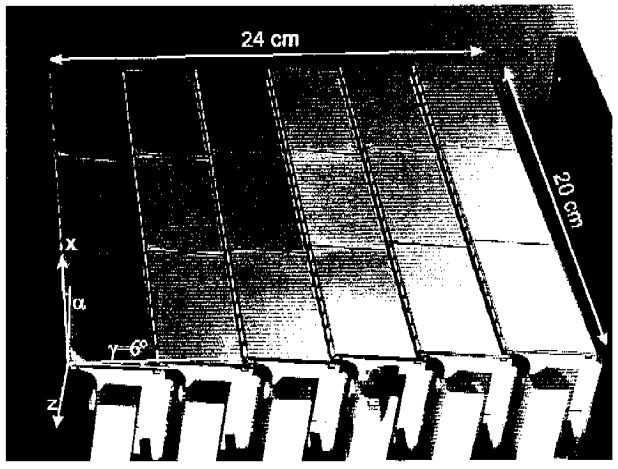

Fig. 1. The sensitive surface of the PILATUS 1M detector - showing its six banks, each with three modules. The banks are tilted by $\gamma = 6°$ to reduce the spacing of the modules in the vertical (y) direction. Between the banks the wirebond connections can be seen. The module positions are defined by the position in x, y and z, the rotation in the x–y plane, α, and the tilt angle, γ.

of the pixel array within a module. But since the 300 μm silicon sensor is much thicker than the thin phosphor screens of large CCD cameras (~30 μm), a considerable parallax effect distorts the images. The parallax distortion depends on the pixel geometry, thickness and composition of the sensor as well as the energy and angle of incidence of the X-ray photons. A second source of distortion is the mechanical deviation of the modules from their assumed positions introducing another spatial error with 5 degrees of freedom (Fig. 1). The module positions were precisely measured and this information was introduced to the correction procedure. The third and largest contribution to the distortion comes from the 6° tilt of the banks. This effect is corrected by projecting the tilted sensor surfaces onto a virtual plane. To summarize, three effects contribute to the spatial distortion:

- The parallax effect
- Mechanical module displacement
- 6° bank tilt

A raw image taken with the PILATUS 1M detector is shown in Fig. 2. The distortion is manifest. The distance of the detector to the capillary filled with silicon powder (NIST 640C) was 130 mm. The powder rings are deformed by the 6° tilt of the banks. The shadow cast by the periphery of the modules can be seen in the top half of the image. The rectangular dead areas are non-functional readout chips of the detector.

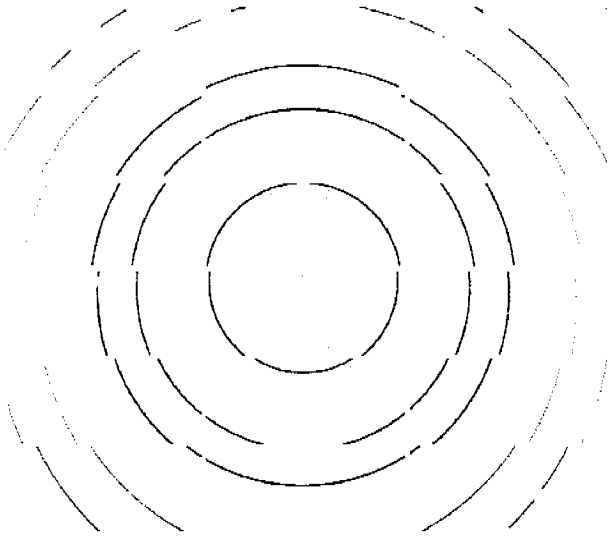

Fig. 2. Raw image of diffraction by silicon powder (NIST 640C) (dark is high intensity). The distortion of the circles can be seen particularly at the boundaries between modules. The X-ray energy was 12 keV, the detector distance to the powder specimen was 130 mm.

3. Parallax broadening effect in silicon detectors

In the following section the theory of the parallax effect is derived. A Monte Carlo simulation was written to study the influence of the experimental and detector parameters on the parallax. Finally, the results of the simulation was compared to experimental data obtained with the PILATUS 1M detector.

3.1. Principle of the parallax effect

The parallax effect leads to a smooth distortion of an image caused by the absorption properties of the sensor array. CCD cameras have very thin sensors and have only a small parallax effect [7]. Silicon detectors, unfortunately, need thick sensors and therefore suffer from parallax. For the discussion of the parallax in silicon detectors the geometry and X-ray absorption properties of the sensor as well as the energy and the spatial distribution of the X-ray beam have to be considered.

Fig. 3 shows a schematic cross-section through a structured pixel sensor. Parameter definitions are given in Table 1. Incoming X-rays with a two-dimensional Gaussian distribution σ_{beam} (measured perpendicular to the beam) impinge on the sensor at center position x_0 at an angle θ (normal angle of incidence: $\theta = 0°$). The cross-section of the resulting distribution of X-rays on the sensor surface is

$$P(x) \propto e^{-(x-x_0)^2/2(\sigma_{\text{beam}}/\cos\theta)^2}.$$

If the absorption of all photons were to take place directly at the surface, this distribution could be directly measured. But the conversion points of individual photons is given by the exponential absorption function. The number of X-rays, N, entering at an angle θ which are absorbed in a

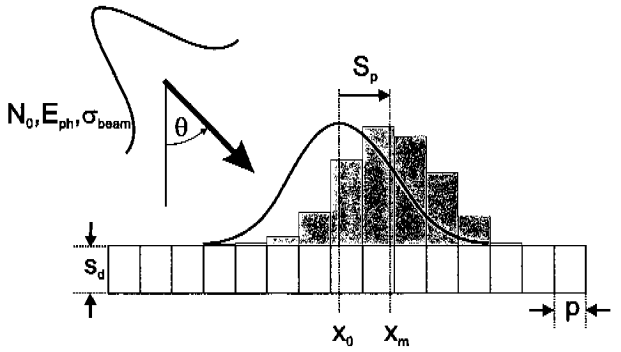

Fig. 3. Schematic view illustrating the principle of the parallax effect: the incident X-ray beam is absorbed by the sensor of thickness s_d. This leads to a shift of the detected distribution in respect to the pattern incident on the surface.

Table 1
Definition and initial values for the parameters of the Monte Carlo simulation

Parameter	Abbreviation	Value
Beam orientation	θ, φ	0°, 0°
Beam width	σ_{beam}	1 pixel
Beam intensity	N_0	10 000 photons
Photon energy	E_{ph}	12 keV
Sensor thickness	s_d	300 μm
Pixel size	p	217 μm
Absorption coefficient	μ/ρ	19.75 cm²/g (silicon)
Density	ρ	2.33 g/cm³ (silicon)
Threshold	th_0	6 keV = $E_{\text{ph}}/2$
Charge diffusion	σ_c	12 μm @ 300 μm

sensor with thickness s_d is

$$N(\theta, s_d) = N_0(1 - e^{-[\mu/\rho]\rho(s_d/\cos\theta)}) \quad (1)$$

where the mass attenuation coefficient μ/ρ is a function of the photon energy E_{ph} and ρ is the density of silicon. Thus, the distribution of the detected photons is shifted to a new mean position x_{m}. The difference of the measured center of mass x_{m} in the pixel and x_0 of the incoming distribution on the surface is the parallax shift

$$S_{\text{p}} = x_0 - x_{\text{m}}. \quad (2)$$

A photon with energy E_{ph} converting in the sensor, generates N_{eh} electron–hole-pairs:

$$N_{\text{eh}} = E_{\text{ph}}/3.61\,\text{eV}. \quad (3)$$

The absorption of a 12 keV X-ray produces a charge cloud of about 3324 e–h-pairs. Due to the high electric field ($V_{\text{bias}} = 100$ V) that is present in the depletion region, e–h-pairs drift through the sensor in opposite directions. When the charge arrives at the p implant of the sensor, the charge cloud has widened due to diffusion [4]. Thus, charge generated in one pixel can be shared between the amplifiers of neighboring pixels if the conversion point is near the pixel boundaries. It was shown in several publications (e.g. [8]) that the effect of charge sharing can be minimized by setting the threshold of the comparator to $E_{\text{ph}}/2$.

3.2. Simulation

For X-rays impinging on the surface of the detector, the detected number of photons in each pixel can be calculated. A Monte Carlo simulation (SLSProject, M. Loeckner, University of Bonn) which traces each photon in an array of pixels was adapted to our conditions. The coordinate system is shown in Figs. 1 and 4. The incoming photon beam is defined by the parameters θ, φ, the beam center, P_0, the shortest distance from the specimen to the plane of the sensor surface, d, and the

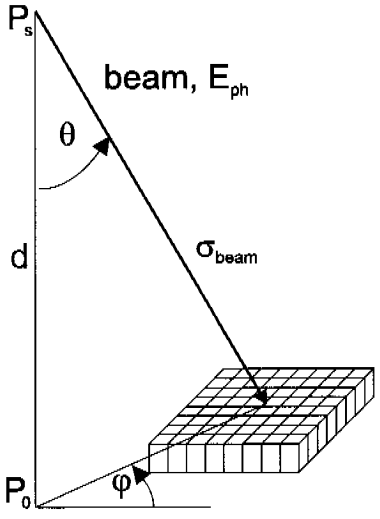

Fig. 4. Definition of the coordinate system for the Monte Carlo simulation of the parallax effect. The path of each photon of the X-ray beam with a Gaussian intensity distribution of width σ_{beam} is calculated and the conversion point inside the sensor is simulated (the abbreviations are defined in the text).

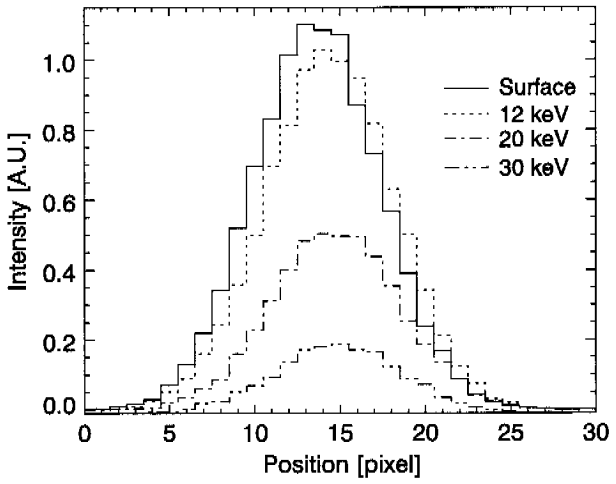

Fig. 5. Simulated intensity distribution of an X-ray beam ($\sigma_{beam} = 2p$) impinging with $\theta = 60°$ on the sensor. The dashed lines correspond to simulations with different photon energies E_{ph}.

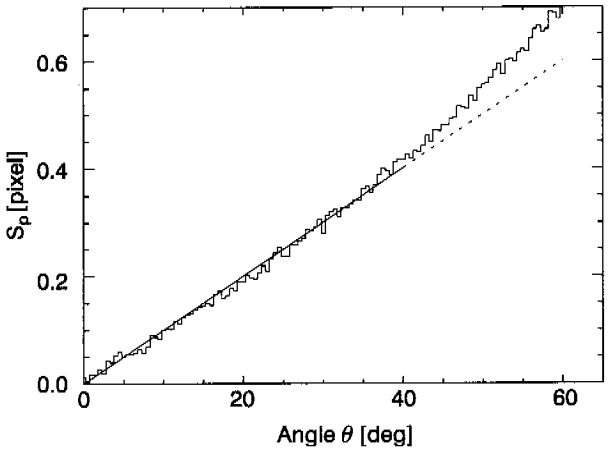

Fig. 6. Parallax shift S_p vs. angle of incidence θ. S_p increases linearly with a small quadratic component. A linear fit for $\theta < 40°$ is shown.

photon energy, E_{ph}. The beam center was kept constant for all simulations. A Gaussian beam profile of width σ_{beam} was generated with N_0 photons. The point where each photon trace crosses the sensor surface is calculated. The probability distribution of the conversion points at the end of the photon paths through the sensor is given by Eq. (1) using the parameters θ, φ, s_d, ρ, and μ/ρ (Table 1). The amount of charge generated N_{ch} by each photon is calculated according to Eq. (3). The broadening of the charge due to diffusion is simulated as well, using an average width of the charge cloud of $\sigma_c = 6\,\mu m$ [4]. The event is counted in pixel (i,j) at position $P(x_i, y_j)$ if the charge is larger than the threshold value th_0. In Fig. 5 an X-ray beam with $\sigma_{beam} = 2p$ and an angle of incidence $\theta = 60°$ to the sensor is shown. The parallax shift S_p (Eq. (2)) depends on the different simulation parameters and is used to characterize the parallax effect.

The dependence of the parallax shift S_p on the angle of incidence is plotted in Fig. 6. The parameters used are the initial values listed in Table 1. The beam was scanned over the pixels by varying θ and the center of mass x_0 and x_m was recorded. As the dependence is almost linear over $0 < \theta < 40°$, a linear function with $S_p = F_p\theta$ was fitted in this range. From the simulation a parallax factor

$$F_p = 1 \times 10^{-2} \pm 4 \times 10^{-5}\,\text{pixel/deg}$$

was found. The center of mass of an X-ray beam moves about 40% of the pixel width at $\theta = 40°$. The parallax factor F_p is useful for the correction of experimental data (Section 5) and, as the parallax shift is small, a more accurate calculation of F_p serves no purpose.

For beam sizes which are small compared to the pixel size, the parallax shift S_p oscillates as a function of θ. The oscillation is then approximated by the factor F_p. An incoming beam with $\sigma_{beam} = 0.2p$ was simulated and S_p is plotted as a function of θ (Fig. 7).

If the beam impinges at the central region of a pixel, x_m does not change and is always calculated in the center of this pixel. Only in the boundary region between two pixels does x_m change. For large angles of incidence the oscillation stops, because the parallax effect increases the width of the beam and thus the beam is recorded in several pixels. This leads, counterintuitively, to a higher accuracy of the measurement of x_m and can also be seen in the measurements (Section 3.3).

Another question is whether the two parameters θ and φ are correlated with each other. From the symmetry of the pixel array and the homogeneity of the sensor material this should not be the case. The simulation with constant θ and different φ

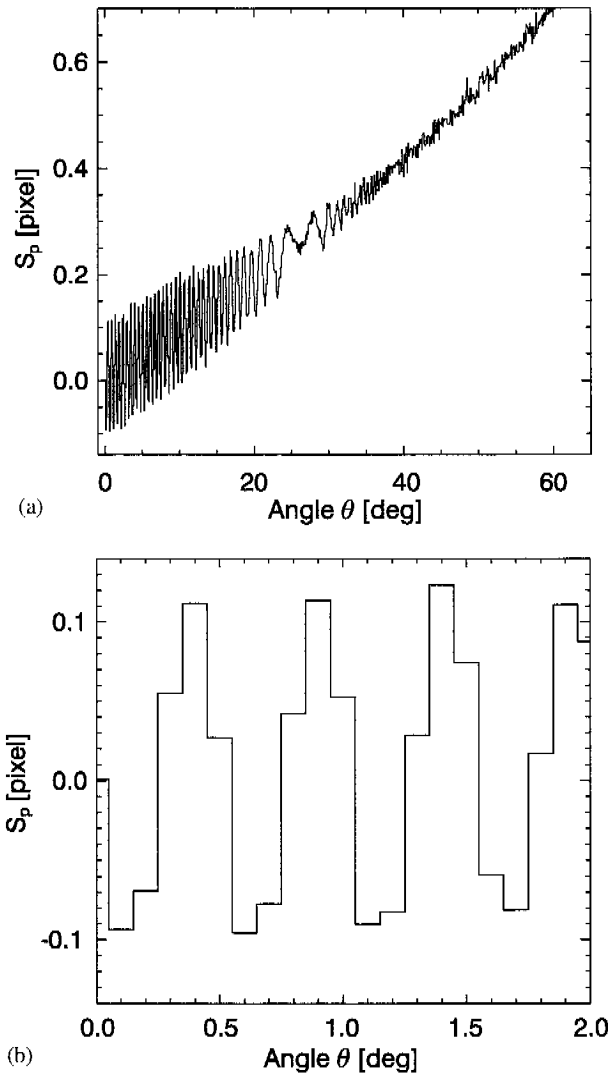

Fig. 7. Parallax shift S_p as function of the angle of incidence θ for a small X-ray beam ($\sigma_{beam} = 0.2p$). The oscillation (see magnification (b)) smears out for larger θ (a).

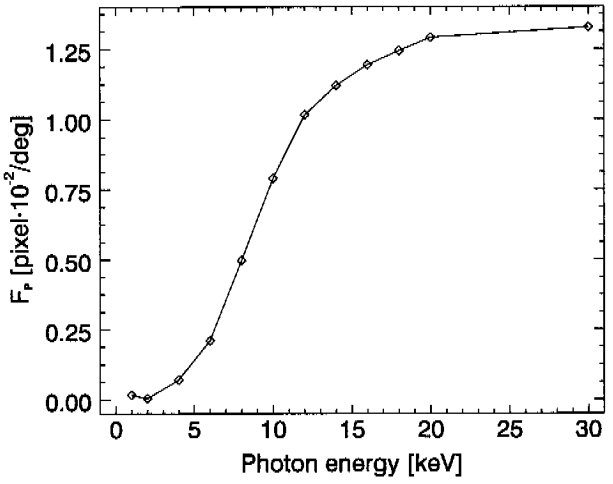

Fig. 8. Parallax factor F_p vs. photon energy E_{ph}: the short mean free path of the photons in the silicon leads to a conversion of most of the X-rays near the sensor surface for small energies (small parallax effect). For higher energies fewer photons are stopped inside the sensor and F_p reaches a maximum value.

shows that the parallax factor is independent of φ. The two-dimensional parallax effect can thus be reduced to a one-dimensional effect along a line of pixels. This simplifies the correction.

The dependence of F_p on the photon energy E_{ph} is plotted in Fig. 8. For higher photon energies F_p is maximal, and for low energies it vanishes. This can be explained by the shorter mean free path length of photons in the silicon for small E_{ph}, which leads to a conversion of most of the X-rays close to the sensor surface and, hence, the measured information reflects the incoming beam profile. It can be concluded that data taken at $E_{ph} \sim 6$ keV with a silicon pixel detector are only little affected by the parallax effect. Photons with higher energies can travel deep into the sensor, in which case the parallax effect increases and saturates for $E_{ph} > 20$ keV. At this energy only a small fraction of the photons is stopped in the sensor. For the energy range where most of the experiments with the PILATUS 1M detector are performed (6–18 keV), F_p show the greatest changes. Therefore, it is essential to calculate the parallax factor for each energy.

The simulation can also be used to study different sensor geometries (p and s_d in Table 1). The variation of other experimental and detector parameters can be derived by varying the parameters already discussed. For example, an increase of the material parameters ρ and μ_ρ is identical to a reduction of the photon energy. It can be concluded that there are two parameters which contribute to the parallax effect for a given sensor material: the photon energy, E_{ph}, and the angle of incidence, θ. As the factor F_p characterizes the dependence of the parallax effect on the angle of incidence, this factor can be used for correcting images which are affected by parallax. The

dependence of F_p on the energy can be taken from Fig. 8.

3.3. Measurement of the parallax effect

The parallax effect was measured at the protein crystallography beamline X06SA of the SLS. A single bank of the PILATUS detector was exposed to the direct attenuated X-ray beam. The width of the beam could be confined to a fraction of a pixel (σ_{beam}~15 μm). The energy was set to 13.5 keV and the intensity of the beam was reduced to ~14 000 photons/s with a 0.25 mm Fe filter. The distance of the detector to the exit of the beam pipe was ~250 mm in air. The detector was scanned four times in the vertical direction with steps of 0.1 ± 0.02 pixel (21.7 μm) and 1 s exposures were made. Four data sets were taken with angles $\theta = 0°, 10°, 20°$ and 27.5° from the surface normal. From the images the center of mass x_m from the detected beam was calculated and plotted against the position of the beam on the detector x_0 (diamonds in Fig. 9). The zero position of x_0 is an arbitrary place on the detector. The center of mass x_m does not change as long as the beam is within one pixel. When the beam reaches the boundary between two pixels, x_m moves to the next pixel. The steps are broadened due to

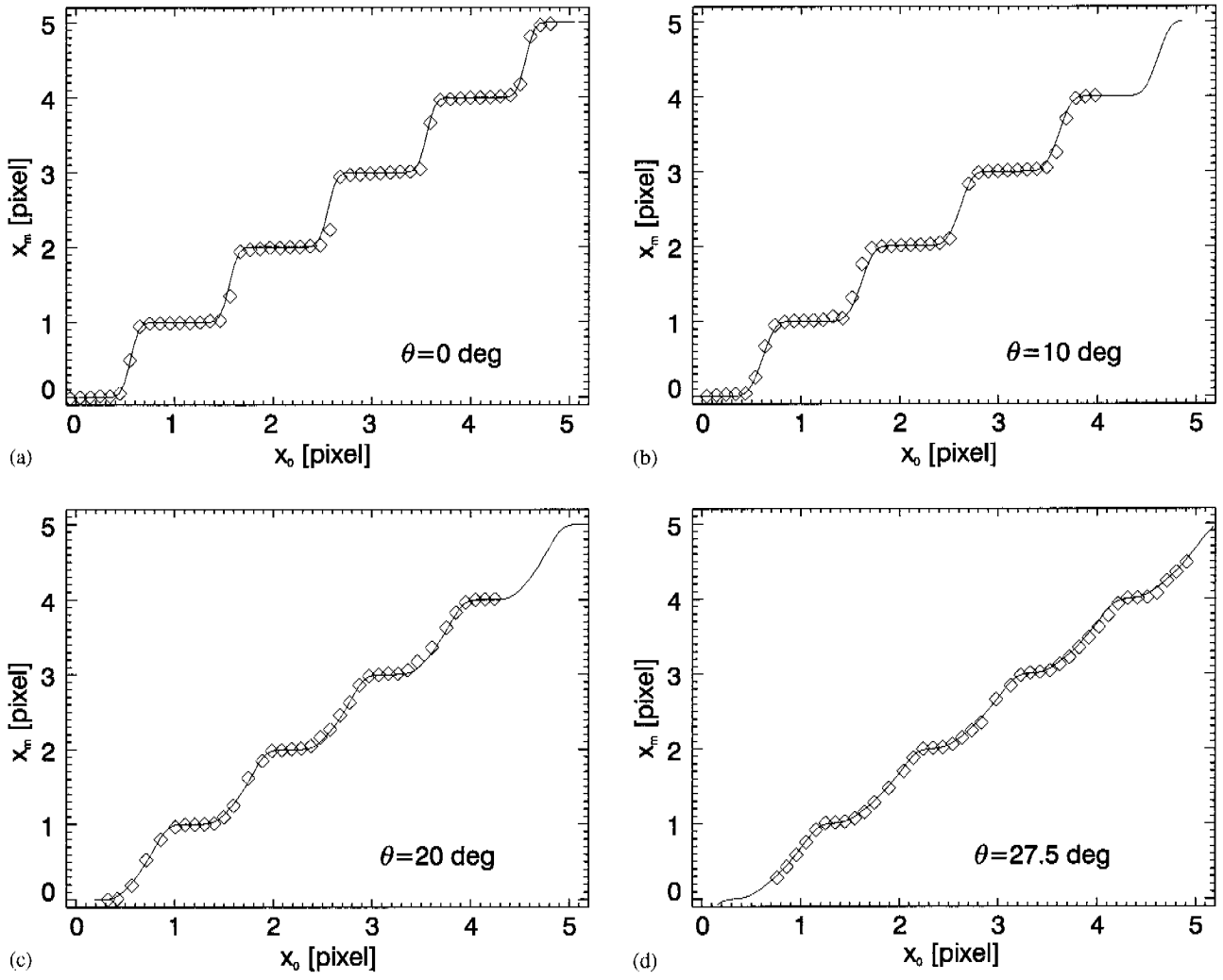

Fig. 9. Experimental data of scanning a 13.5 keV beam (σ_{beam} = 15 μm) over 217 μm pixels (diamonds) compared to a simulation (line). (a) With normal angle of incidence θ; (b) with $\theta = 10°$; (c) $\theta = 20°$; (d) $\theta = 27.5°$.

Table 2
Measured σ from the graphs of Fig. 9. The width of the beam was calculated by differentiating the graphs at the boundaries between two pixels

Angle of incidence θ (deg)	$\overline{\sigma_{exp}}$ (μm)	$\overline{\sigma_{sim}}$ (μm)
0.0 (normal)	17.6 ± 1.5	16.2 ± 0.1
10.0	21.7 ± 1.4	22.9 ± 0.2
20.0	41.9 ± 5.5	41.9 ± 0.8
27.5	60.4 ± 5.6	58.5 ± 1.1

Table 3
Summary of the mechanical mounting precision. The table lists the mean displacement error of all the 18 modules of the PILATUS 1M detector. The parameters are defined in Fig. 1

Parameter	Mean value
$\overline{\Delta x}$	40 ±48 μm
$\overline{\Delta y}$	−412 ±302 μm
$\overline{\Delta z}$	445 ±249 μm
$\overline{\alpha}$	−0.024 ±0.044°
$\overline{\gamma}$	5.83 ±0.078°

the parallax effect when θ is increased. The same experiment was simulated (Section 3.2). The simulation and the experimental parameters are identical. The x_m's from the simulations are plotted against x_0 (lines in Fig. 9).

The agreement between the experiment and the simulation was verified by the differentiation of the slopes at the boundary between two pixels, which led to σ_{exp} and σ_{sim} for the four different angles, θ. From four fully recorded steps average $\overline{\sigma_{exp}}$ and $\overline{\sigma_{sim}}$ were calculated (Table 2). The beam profile was assumed to follow a Gaussian distribution. The experiment shows that in case of $\sigma_{beam} \ll p$ all datasets show a "plateau". In these regions the measured position of the beam is not defined better than 0.5 pixel. For normal angle of incidence the width of the plateau is $\sim 0.7p$. This leads to a variance of the equipartitioned beam position [9] of

$$\sqrt{\text{var}} = 44\,\mu\text{m} \quad \text{i.e.} \frac{0.7p}{\sqrt{12}}$$

which decreases for larger angles θ.

4. Geometrical distortion

4.1. Module displacement

Within a module of the PILATUS 1M detector there is only the distortion from the parallax effect as discussed above. By using an array of 18 modules mechanical displacement errors are introduced. These errors come from the gluing of the sensor arrays on the support and from mounting the modules into the detector frame. The errors are the deviation of the final module positions in the 6 × 3 array from their assumed positions. There are 5 degrees of freedom: the displacement in x, y and z, the rotation in the x–y plane, α and the tilt angle, γ, of the modules (Fig. 1).

The position and orientation in the x–y plane of each module was measured at the Institute for Particle Physics (IPP) of the Swiss Federal Institute of Technology (ETH) Zurich, using an optical comparator with an accuracy of 5 μm (Mitutoyo KN 815). The positions of four points on the periphery of the readout chips of the modules where recorded. From this measurement the displacement from the assumed positions Δx_i, Δy_i and the rotation α_i were extracted for each module i. The readout chips are positioned to an accuracy of ~1 μm in respect to the pixel array of the sensor. The tilt angle γ_i and the deviation Δz_i have been measured at the Paul Scherrer Institute with a touch measure system (Wenzel). Three points on the sensor surface of each module were measured. With these measures the displacement Δz_i and the tilt angle γ_i could be calculated. From these two measurements a lookup table was generated as input for the distortion correction. In Table 3 the results of the measured parameters are summarized. The value of Δy shows that the gap between the six banks of the PILATUS 1M detector is not an integer of the pixel size ($p = 217\,\mu$m). The vertical gap on average is $4.26p = 0.924$ mm wide.

4.2. Bank tilt

In order to use the data from the PILATUS 1M detector with established crystallographic processing software, the data must be corrected. The pixel coordinates (i,j) of the data are projected

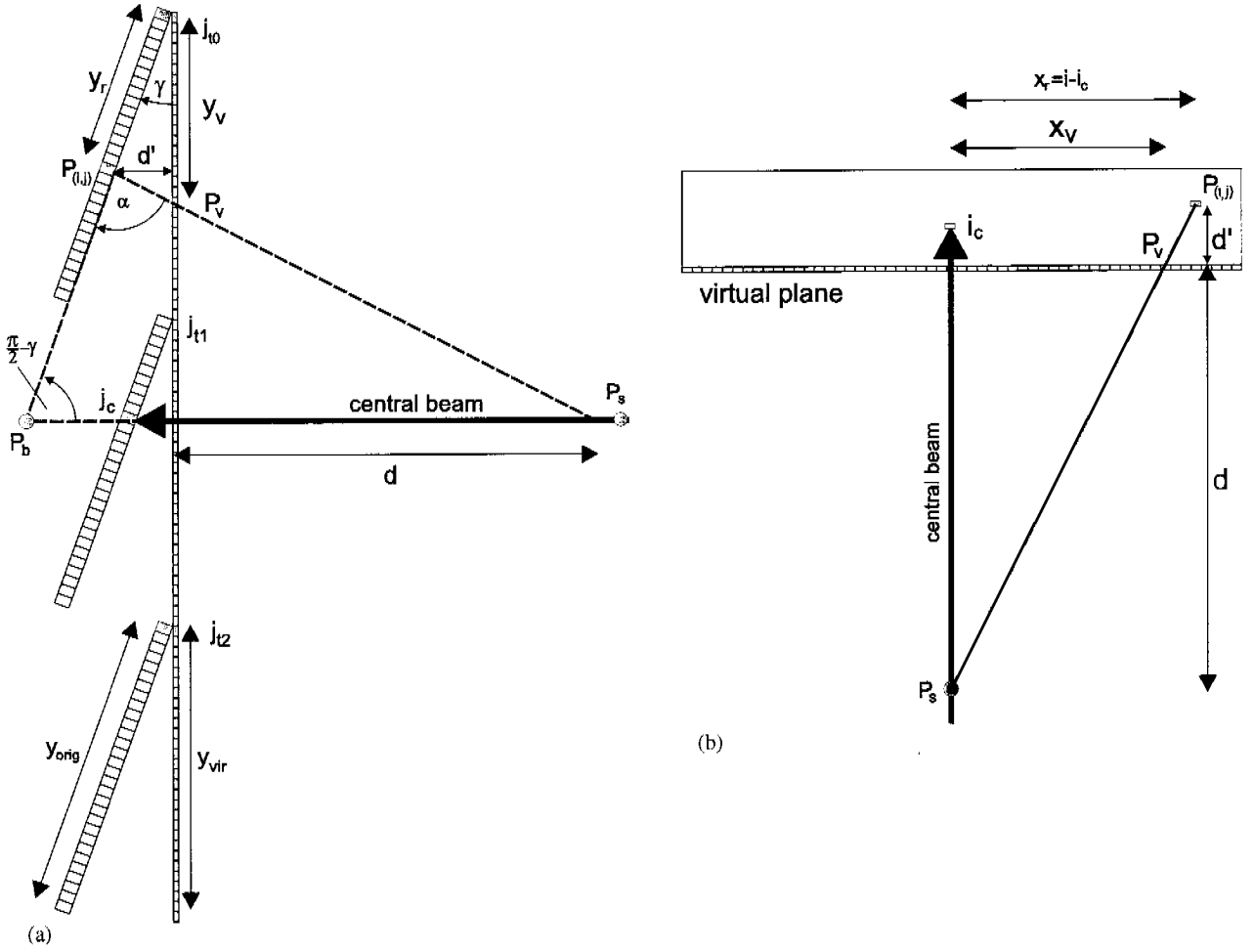

Fig. 10. Schematic side view (a) and top view (b) of the PILATUS 1M detector (not to scale). Each pixel at $P_{(i,j)}$ must be projected to the corresponding pixel position P_v on the virtual plane.

onto a virtual plane situated in front of the detector (Fig. 10). The first row ($j = 0$) defines the first line of the virtual plane and each following top row of each bank b ($0 \leqslant b \leqslant 5$) also lies in this plane.[1] The shortest distance d from the specimen to the detector is known, as well as the detector origin (i_c, j_c). If the direct beam is normal to the virtual plane than the location of the direct beam is equal to (i_c, j_c). Shifts of the pixels in the horizontal (x) and vertical (y) direction are calculated; all the variable lengths are in [mm] unless otherwise noted.

[1]The ideal pixel positions (i,j) are modified by the actual positions of the pixel in space (i_r, j_r) and the parallax effect lead to surface pixel positions (i_s, j_s) (Section 5.1).

The calculation starts with the vertical distortion: the distance y_r from the first pixel j_{tb} to pixel j of bank b is given by

$$y_r = p(j - j_{tb}), \quad 0 \leqslant b \leqslant 5$$

starting with the top row, $j = 0$, of the detector. The length y_v on the virtual plane is determined by

$$y_v = y_r \frac{\sin\alpha}{\sin(\alpha - \gamma)}$$

with the tilt angle γ. The angle α is related to the angle of incidence, 0 (Fig. 4):

$$0 = \frac{\pi}{2} - \alpha.$$

The angle α can by found from the triangle $P_b P_{ij} P_s$; two legs,

$\overline{P_b P_{ij}} = p(j_c - j)$ and

$\overline{P_b P_s} = d + (y_r + p(j_c - j))\sin\gamma$

and the included angle $(\pi/2 - \gamma)$ are given. Thus, the angle, α, is

$$\cos\alpha = \frac{(\overline{P_b P_{ij}} - \overline{P_b P_s}\cos(\pi/2 - \gamma))}{(\overline{P_b P_{ij}}^2 + \overline{P_b P_s}^2 - 2\overline{P_b P_{ij}}\,\overline{P_b P_s}\cos(\pi/2 - \gamma))^{1/2}}.$$

The major contribution to the vertical shift is $(y_r - y_v)$. The tilt angle γ leads to a difference in the vertical module length, G_b, which can by calculated as

$$G_b = y_{orig} - y_{vir} = y_{orig}(1 - \cos\gamma)$$

where y_{orig} and y_{vir} are the real and virtual module lengths. This factor must be subtracted b times from the correction value y_{sh} to create a continuous plane (b = bank of pixel j). For this reason the top pixel row of each bank is also shifted, although these lines lie in the virtual plane. The total value of the vertical correction value can be expressed in units of pixels as

$$y_{sh} = \frac{1}{p}((y_r - y_v) - bG_b), \quad 0 \leqslant b \leqslant 5. \tag{4}$$

For the horizontal part of the correction vector, only the difference of the pixel position on the detector x_r and the length x_v on the virtual plane need to be calculated. The value x_r is the difference $x - x_c$ and x_v can be calculated from the ratio

$$\frac{x_v}{d} = \frac{x_r}{d + d'}.$$

The horizontal value for the transformation vector in pixels is then

$$x_{sh} = \frac{1}{p}(x_r - x_v) = \frac{1}{p}\left((x - x_c)\frac{d'}{d + d'}\right) \tag{5}$$

with

$$d' = y_r \sin\gamma$$

and is therefore coupled with the vertical transformation. The transformation varies smoothly along a row whereas in a column discontinuous steps occur between the banks. The transformation depends on the detector position $(d, (x_c, y_c))$ and the detector geometry (γ). The vector (x_{sh}, y_{sh}) can have a magnitude of several pixels. This can be seen in Fig. 11 for a row $(j = 100)$ and a column $(i = 100)$ at a distance of $d = 200$ mm. The

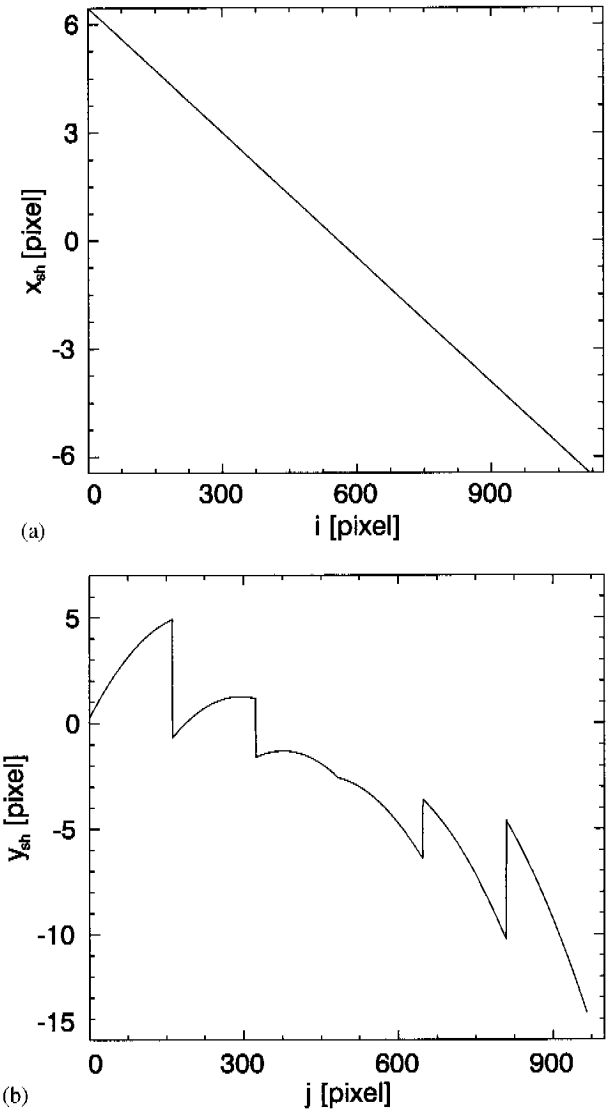

Fig. 11. Horizontal (a) and vertical (b) distortion transformation functions of a tilted detector plotted for a row ($j = 100$) and a column ($i = 100$). The tilt of the banks lead to discontinuous steps and large distortions in the vertical direction.

detector origin (x_c, y_c) is at the center of the detector.

The apparent size of the gaps between the six banks depends on the specimen distance d. For large distances ($d \to \infty$) the gaps are the specified 4.26 pixels (0.924 mm). The gaps on the top half of the detector are reduced as the distance gets smaller. However, the shadow from the periphery of the modules increases and leads to many unusable pixels. On the bottom half the gaps open up significantly. At $d = 130$ mm the effective area of the detector is reduced by 11.5%. Using a flat geometry with a 4.5 mm gap between the banks (the minimal spacing of the modules of the PILATUS 1M detector) the loss would be only 11.2%. This means that the advantage of this tilted geometry is largely compromised at experimentally useful distances, d, while the magnitude of the correction is significantly increased.

5. Distortion calibration

5.1. The spatial distortion algorithm

The correction of the three sources of distortion depends on the experimental parameters, namely the photon energy, the sample to detector distance and the effective origin of the detector. These parameters need to be known with high precision. The correction procedure is the following:

(1) The ideal pixel positions (i,j) are corrected using the displacement errors Δx_i, Δy_i, Δz_i, α_i and γ_i (Section 4.1) leading to real pixel positions (i_r, j_r).
(2) The information measured in the pixel at (i_r, j_r) is corrected for the parallax effect. The angle of incidence θ for each pixel at the corrected position is calculated and multiplied with the parallax factor F_p. This corresponds to a parallax back transformation and leads to surface pixel positions (i_s, j_s). The parameter F_p is taken from Fig. 8.
(3) The data are projected from the module surface to the virtual plane. For this Eqs. (4) and (5) are used with (i_s, j_s) as pixel positions. Special care must be taken for pixels in the shadow and in the gap, which do not have a destination on the virtual plane.

The complete distortion algorithm produces displacement values (x^i_{sh}, y^j_{sh}) for each pixel (i,j). These values are stored in two correction files. For each experiment these files must be recalculated if one of the parameters changes.

For the actual image correction, an algorithm developed by Barna et al. is used [10]. The pixel (i,j) is moved to the new position $(i + x^i_{sh}, j + y^j_{sh})$. At the destination the area overlap of the source pixel with the pixel array in the destination image is calculated and the intensity of the source pixel is distributed accordingly (Fig. 12a). If the total area of the destination pixel changes due to the distortion, the intensity is scaled. In most cases,

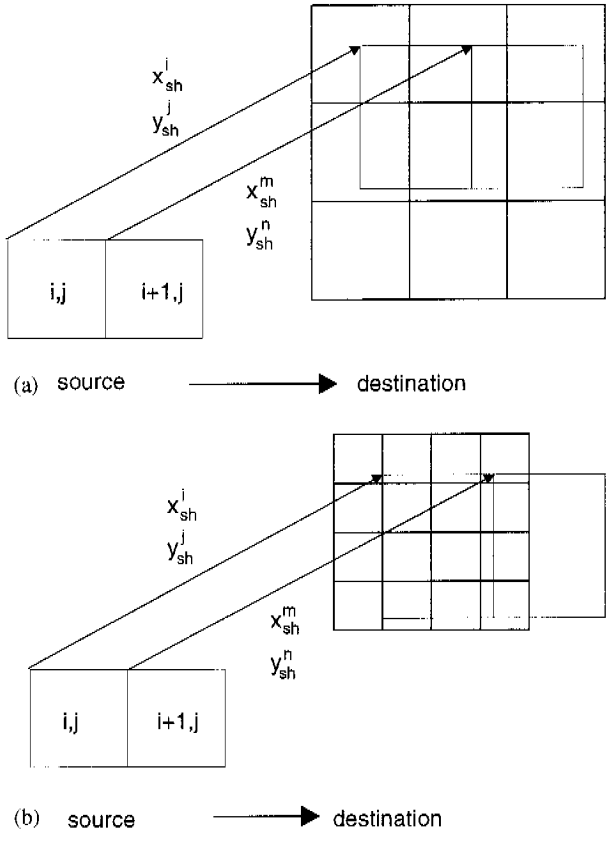

Fig. 12. Distortion correction of an image. (a) The intensity of the source pixel at (i,j) is distributed into the destination pixels around the new location at $(i + x^i_{sh}, j + y^j_{sh})$ according to the overlap of area. (b) The modified algorithm uses a finer grid in the destination image to better preserve the beam profile.

the intensity is distributed into four pixels in the destination image. The width of a photon beam with $\sigma_{\mathrm{bcam}} < p$ will be increased to $\sigma_{\mathrm{bcam}} \sim 2p$. To better preserve the 2D-profiles, the algorithm has been modified in such a way that the pixel area in the destination image is a quarter of the source pixel area. With this modification the source pixel matches better with the grid in the destination images as seen in Fig. 12b. The rules for distributing the intensity of the source pixels are the same as in the original code. The oversampling better preserves the single pixel signals of the source image. The second advantage of the algorithm is that non-responding areas of the detector occupy almost the same area in the destination image.

5.2. *Distortion measurements and refinement with a Tantalum mask*

The standard way to correct data from imaging devices is to measure the distortion directly. This can be done by using a mask (usually made from a high-Z material like Tantalum) with a matrix M_{h} of well-defined holes. The images of this matrix visualize the distortion of the detector. The distortion of the fiber optic taper of a CCD camera is taken as a continuous function. A spline fit through the matrix M_{h} yields in a good measurement for the displacement of each pixel of the detector [10]. In the case of modular detectors with discrete steps this approach does not work. Especially, the 6° tilt angle of the modules introduces sharp discontinuous steps in the distortion (Fig. 11b). In this case a spline fit to the mask image results in a wrong correction matrix and therefore images of a Ta-mask cannot be used directly for measuring the distortion of a modular detector.

However, mask images can be used to verify the geometrical correction algorithm. Several mask images were recorded at the protein crystallography beamline X06SA with the PILATUS 1M detector. The 0.2 mm thick Ta-mask contains a 45 × 40 array of holes of diameter of 0.2 mm with 5 mm spacings (~100 holes per module). The mask was placed ~3 cm in front of the detector. The detector was illuminated with monoenergetic X-rays from a fluorescent sample (Br fluorescence, $E_{\mathrm{ph}} = 11.92\,\mathrm{keV}, d = 130\,\mathrm{cm}$). The images of the holes were present, on average, in 4 pixels. To reduce the inaccuracy introduced by dead pixels of the detector, the images were taken at nine different positions; between images the detector was shifted by one pixel while leaving the mask stationary. The nine images were merged into one image to reduce the number of dead channels. This means that a value of a pixel represents the median of the corresponding good pixels in the source images, or the average if only two values above zero were measured or only one datum if data was recorded in one image. A section of the merged image is shown in Fig. 13a. The geometrical distortion of the image was corrected as described (Fig. 13b). The distortion of the matrix M_{h} is a measure for the remaining distortion. For the measurement of the distortion a correction software developed for CCDs by Barna et al. was adapted [10]: the center of mass of each point of the matrix M_{h} is measured and the closest perfect grid is calculated. All points which have a dead pixel as neighbor are rejected from the calculation. The deviation σ from the perfect grid is calculated for each point. The average deviation for all points is $\sigma_{m1} = 272\,\mu\mathrm{m}$ for the PILATUS 1M detector, that is to say, greater than one pixel.

The mask data were used to refine the position of the modules. The distortion within one module is only affected by the parallax effect. The unit cell parameter $|\vec{a}|$ of the mask matrix M_{h} can therefore be calculated for each of the 18 modules individually: the length $|\vec{a}|$ is correlated with the position of the module along the z-axis. The direction of $\vec{a}$ represents the remaining rotation of the module α and the origin of the matrix is defined by the remaining displacement of the modules $(\Delta x, \Delta y)$. These module displacement parameters were adjusted until all 18 calculated matrices converged to the same value. Again the algorithm described above was applied to determine the deviation of the matrix M_{h} from a perfect grid. The remaining distortion error for the detector could be reduced to

$$\sigma_{m2} = 72\,\mu\mathrm{m} \tag{6}$$

with the refinement method.

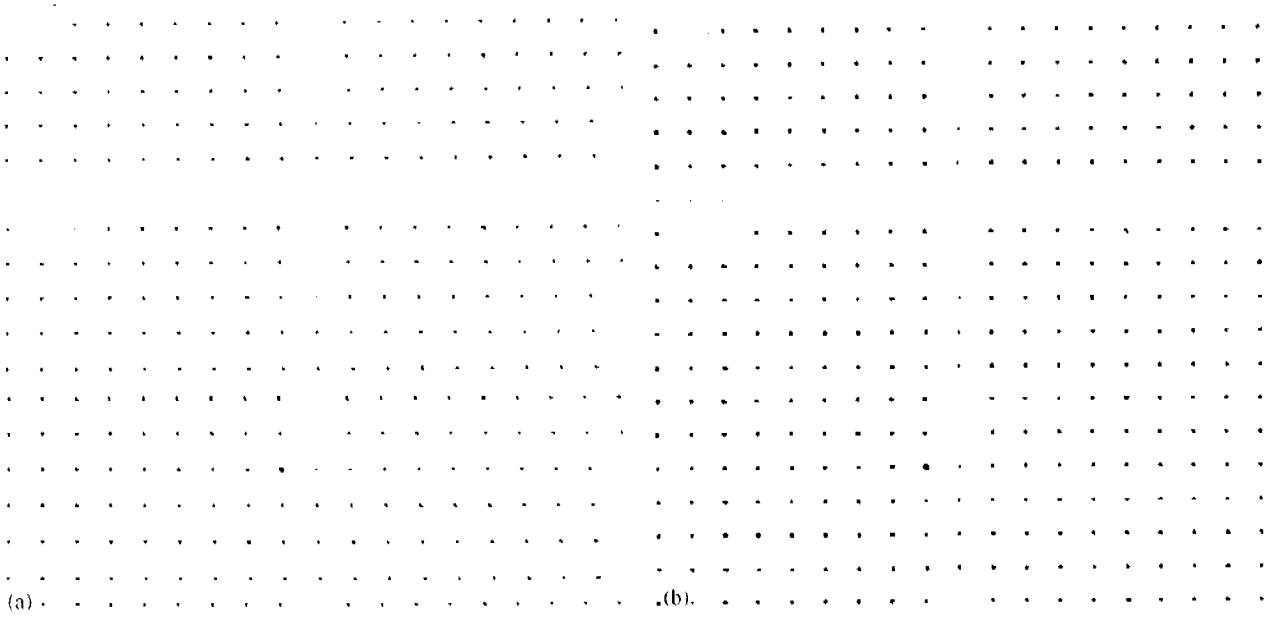

Fig. 13. Section of the image of a Tantalum mask with a matrix of well-defined holes (dark is high intensity). (a) The distorted raw image; (b) the same region after distortion correction of the image.

5.3. Measurements of silicon and glycine powder patterns

Another way to characterize the distortion correction of a detector is to measure reference crystallographic data (Fig. 14). For this experiment powder patterns from silicon (NIST 640c) and glycine were recorded. The capillaries holding the powders were rotated at 180°/s to reduce texture effects. The glycine powder produced over 50 diffraction rings, but many of them are too close to be resolved. Therefore, 10 rings were selected for the measurement. A raw image of the silicon powder rings is displayed in Fig. 2. The distortion corrected images are shown in Figs. 15a, b. The diffraction rings were recorded with the PILATUS 1M detector at a detector to specimen distance of 130 ± 5 mm (silicon) and 180 ± 5 mm (glycine) with a photon energy of 12 keV. The radii of the distortion corrected rings were measured along the ring in 0.5° steps using an integration algorithm developed by us. The algorithm calculates the deviation from a perfect ring, which is a measure of the uncorrectable spatial distortion of the data.

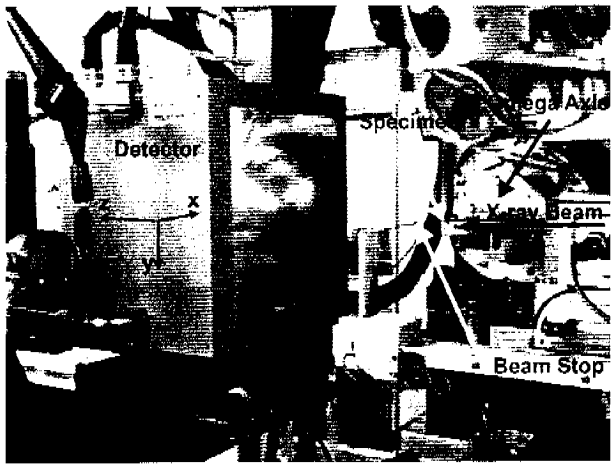

Fig. 14. The experimental setup at beamline X06SA of the SLS. The X-ray photons are diffracted from the powder in the rotating capillary. The central beam is stopped by a small piece of lead. The powder patterns are collected from the PILATUS 1M detector.

The measured deviation of the radii of the silicon powder σ_{si} are listed in Table 4 and from the glycine powder σ_{gly} in Table 5. The detector to specimen distance for silicon was refined

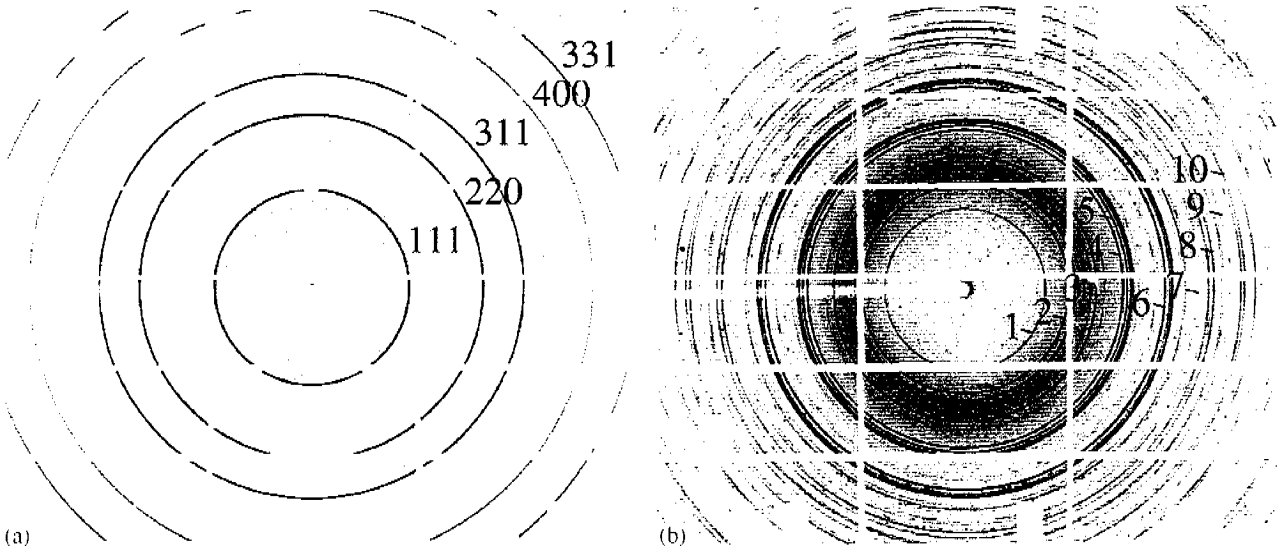

Fig. 15. Distortion corrected images of crystallographic powder patterns (dark is high intensity). (a) Silicon powder (NIST 640C); cf. Fig. 2. The hkl labels correspond to Table 4. (b) The distortion corrected image of glycine powder patterns. The labels correspond to Table 5.

Table 4
Measurements of the radii of Silicon-powder rings

Reflection	Nominal radius (mm)	Radius $\pm \sigma_{si}$ (mm)
111	44.377	44.355 ± 0.067
220	78.340	78.337 ± 0.052
311	96.724	96.717 ± 0.059
400	128.388	128.464 ± 0.149
331	149.256	149.079 ± 0.026

Table 5
Measurements of the radii of a glycine powder rings

Ring number	Radius $+ \sigma_{gly}$ (mm)
1	31.183 ± 0.074
2	40.037 ± 0.076
3	50.865 ± 0.074
4	60.955 ± 0.088
5	62.843 ± 0.089
6	77.274 ± 0.088
7	89.621 ± 0.061
8	96.088 ± 0.082
9	102.316 ± 0.076
10	108.088 ± 0.095

using the crystal parameters (Space Group $Fd\bar{3}m$, $a = 5.431$ Å) and the measured radii and lead to $d_{eff} = 128.194 \pm 0.084$ mm. The nominal radii for silicon powder rings were then calculated (Table 4). The 400 and 331 rings for the silicon powder and the rings number 9 and 10 of glycine were not completely recorded with the detector. This leads to a fluctuation of the distortion error. The average over the spatial deviations (excluding the incompletely recorded rings) results in

$$\overline{\sigma_{si}} = 59\,\mu m \quad \text{and} \quad \overline{\sigma_{gly}} = 79\,\mu m. \tag{7}$$

In three measurements the residual positional error (Eqs. (6) and (7)) are in good agreement and the average over these errors results in a spatial distortion error of

$$\overline{\sigma} = 70\,\mu m = 0.31p.$$

6. Conclusions and outlook

The origins of image distortion in a large area pixel detector were fully described and have been quantified using a synchrotron X-ray source. The parallax effect leads to a shift of a fraction of a pixel in the recorded photon beam position

depending on the angle of incidence and the photon energy. The module displacement and the tilted architecture introduce large distortions of the detector images. Pixels can be displaced several pixels from their assumed positions, depending on the specimen to detector distance. An existing correction procedure for CCD cameras was adapted to the special needs of the PILATUS 1M detector. The camera can be spatially corrected to a precision of 0.31 pixel (70 μm). The 6° tilt of the banks did not increase the effective area for realistic experimental setups. For the development of the next generation of pixel detectors, the large corrections have to be taken into account to improve the spatial distortion. A flat detector geometry with high precision module placement will greatly reduce the distortion of a modular detector.

Acknowledgements

We thank M. Naef, H. Rickert, S. Streuli and F. Glaus of PSI for their help in fabrication of the PILATUS 1M detector, and C. Schulze-Briese, T. Tomizaki, A. Wagner and C. Pradervand for help in the experimental time at X06SA. G.H. acknowledges support from the Swiss National Science Foundation.

References

[1] C. Gemme, Nucl. Instr. and Meth. A 501 (2003) 87.
[2] S. Schnetzer, Nucl. Instr. and Meth. A 501 (2003) 100.
[3] P. Riedler, et al., Nucl. Instr. and Meth. A 501 (2003) 111.
[4] Ch. Brönnimann, E.F. Eikenberry, B. Hennrich, R. Horisberger, G. Hülsen, E. Pohl, B. Schmitt, C. Schulze-Briese, M. Suzuki, T. Tomizaki, H. Toyokawa, A. Wagner, The PILATUS 1M Detector, J. Synchrotron Radiat., submitted for publication.
[5] Ch. Brönnimann, Ch. Bühler, E.F. Eikenberry, R. Horisberger, G. Hülsen, B. Schmitt, C. Schulze-Briese, M. Suzuki, T. Tomizaki, H. Toyokawa, A. Wagner, Synchrotron Radiat. News 17 (2004) 24.
[6] Ch. Brönnimann, R. Baur, E.F. Eikenberry, S. Kohout, M. Lindner, B. Schmitt, R. Horisberger, Nucl. Instr. and Meth. A 465 (2001) 235.
[7] M.W. Tate, E.F. Eikenberry, S.L. Barna, M.E. Wall, J.L. Lowrance, S.M. Gruner, J. Appl. Crystallogr. 28 (1995) 196.
[8] Ch. Brönnimann, S. Florin, M. Lindner, B. Schmitt, C. Schulze-Briese, Synchrotron Radiat. News 7 (2000) 301.
[9] I.N. Bronstein, K.A. Semendjajew, Taschenbuch der Mathematik, 25th ed., Teubner Verlag, Stuttgart, 1991.
[10] S.L. Barna, E.F. Eikenberry, S.M. Gruner, M.W. Tate, Rev. Sci. Instrum. 70 (7) (1999) 2927.

Seite Leer /
Blank leaf

Chapter 5

Detector Performance

5.1 Counting Statistics of Flatfield Images

5.1.1 Theoretical Counting Statistics for an Ideal Detector

The arrival of photons on the detector is a random process and Poisson distributed [30]:

$$f(k,m) = \frac{m^k}{k!}e^{-m}, \quad (k = 0, 1, ...) \tag{5.1}$$

with m being the average expectation of m measured photons. The variance of the Poisson distribution is [36]

$$\mathrm{var}_p(m) = m \; . \tag{5.2}$$

If p is the absorption probability, $n = mp$ photons are registered in the counter. For counting detectors the absorption process in the sensor is binomially distributed:

$$g(k,m,p) = \binom{m}{k} p^k (1-p)^{m-k} \; . \tag{5.3}$$

with the variance

$$\mathrm{var}_b(m) = mp(1-p) \; . \tag{5.4}$$

Considering this simple model, the convolution of the two processes determines the statistics of counting detectors. The expected variance of the function $h = f \circ g$ is the sum of the variance of the function f and g (App. A):

$$\mathrm{var}(m) = \underbrace{mp}_{\text{incident variance}} + \underbrace{mp(1-p)}_{\text{binomial process acting on } m \text{ photons}} \; . \tag{5.5}$$

5.1.2 Statistics of Flatfield Measurements with the PILATUS 1M Detector

Using flatfield images (see section 4.2) the counting statistics of the PILATUS 1M detector were measured as a function of the number of counts in an image. 20 flatfield images with a counting rate of 2500 γ/s/pixel were added together. Each images was recorded with an exposure time of 1 s. Because of the absence of readout noise this procedure resulted in a series of images which have the identical counting rate but simulate longer exposure times.

From each image the variance was calculated and is shown in Figure 5.1 as a function of the number of counts. The variance is 1.5 % above the expected ideal variance when the number of counts is below 10^4, but the deviation from the ideal variance increases significantly for higher count states. This result indicates that counting errors, caused by the chip design fault (see section 3.1.4), are more frequently observed in images with longer exposure times. Therefore the quality of an intensity measurement cannot be improved by acquiring more photons with longer exposure times with the PILATUS 1M detector.

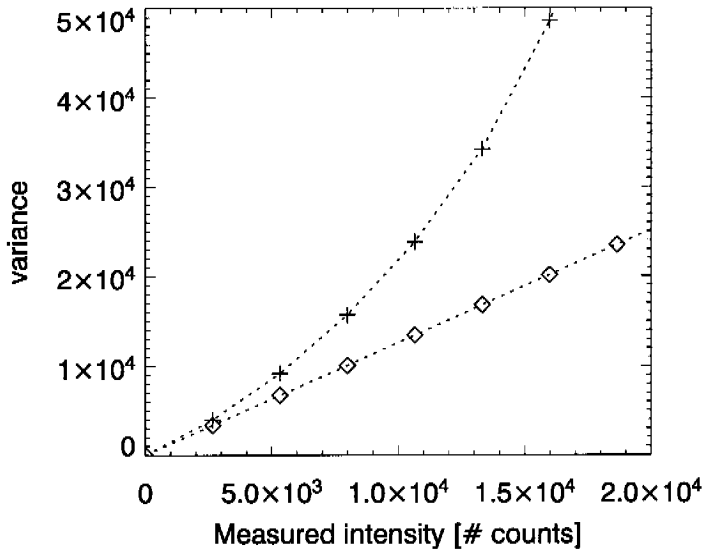

Figure 5.1: Variance of flatfield images as a function of the number of counts in an image. The counting rate is constant for all images. The variance (+) is < 1.5 % above the expected ideal variance ($\diamond$) as long as the number of counts does not exceed 10000, but above this counting errors dominate.

The frequency of occurrence of the counting errors can be measured from the flatfield images: in the 20 images around $290 \cdot 10^3$ pixels were found, having a wrong count value outside the range around the mean count value ($2 - 5.6 \cdot 10^3$ counts). In addition the preferred count value for these errors was searched. The count values of the majority of the counting errors are evenly distributed between 1–2000 and 5600–32767 (Fig. 5.2). But the most frequent number was zero (21100 pixels). It can be concluded that for approximately 7 % of the counting errors, the most probable failure of the counter is a zero count state. The remaining 93 % are evenly distributed.

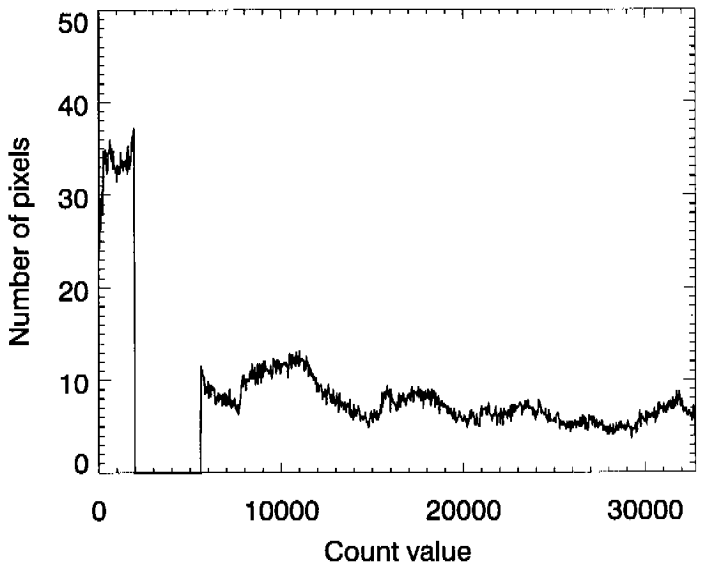

Figure 5.2: The histogram of counting errors observed in 20 flatfield images. The range of correct counting pixels is between 2000–5600. In total 287147 errors occurred. The most probable number is zero (21100 times), which exceeds the scale of the Figure.

5.2 Defect Reduction

5.2.1 Permanent Dead Pixels

Several trials were needed to find a workaround for the high number of dead pixels of the detector, seen in Figure 4.4 (page 55). The number of permanently dead pixels in images of the PILATUS 1M detector could be reduced by mounting the detector on an additional horizontal translation stage (Fig. 5.3). Datasets were recorded twice with a detector translation of one pixel (217 μm) in between. Merging the datasets led to a significant reduction of dead pixels. A pixel value of a corrected image represents the average information of two measurements, the value of one measurement if one pixel was dead or zero if both were dead.

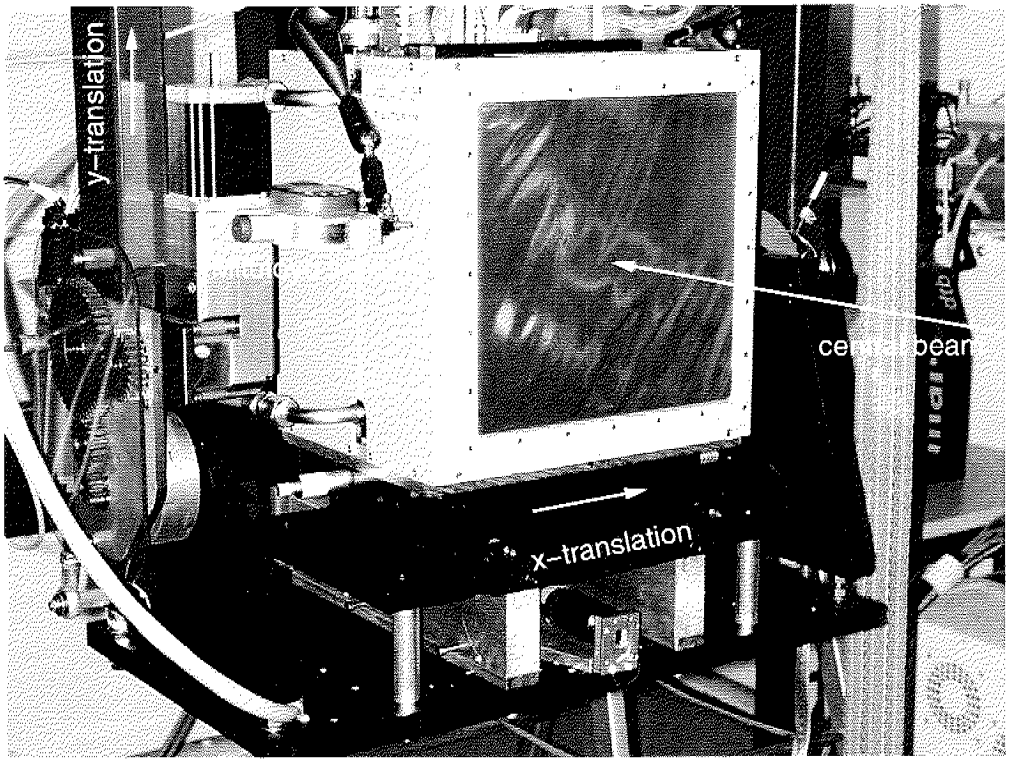

Figure 5.3: With an additional translation stage the detector can be moved along the x–axis. The amount of movement can be monitored by a Mitutoyo sensor at micrometer precision.

5.2.2 Counting Errors

The fact that counting errors dominate the counting statistics was already seen in the study of flatfield images (section 5.1). As a result crystallographic experiments were not satisfactory and more tests of the counting properties of the detector were performed. The conclusion was that counting errors should be reduced by scanning the protein crystallography data for unreasonable counting values.

With the beam conditions present at the protein crystallography beamline X06SA of the SLS, Bragg reflections of well diffracting protein crystals are recorded in about 4 pixels with the PILATUS 1M detector. Figure 5.4 shows three symmetry related reflection profiles, recorded at different positions with the PILATUS 1M detector. For comparison, a reflection profile recorded with a CCD is shown in Figure 5.4a. The profile is represented in a better way with the CCD detector with smaller pixels, although the long range PSF smears the profile out. Profiles sampled with the PILATUS 1M detector depend more on the incident position of the reflection, i.e. if the center of the reflection is centered on a pixel or at the boundary between pixels. Thus, counting errors cannot be detected in the detector plane.

The third dimension of a Bragg reflection profile is defined by the rotation angle ϕ of the crystal, i.e. the movement of the reflection through the Ewald sphere. The rocking curve of the reflections was the basis of the scanning for counting errors. Recorded ϕ–profiles from symmetry related reflections of a thaumatin crystal are shown in Figure 5.5. As discussed in the previous section, counting errors can have any value (Fig. 5.2). The large number of errors with zero count can be detected and repaired. However, the counting errors are frequently hidden in the peak profile (Fig. 5.5d). Only errors which are clearly above or below the expected value are detected. The wrong value is replaced by an average value of the neighboring pixel values in the ϕ–profile.

5.2.3 Results

In Figure 5.6a a raw diffraction image recorded with the PILATUS 1M detector is shown. As reflections from diffraction experiments can only be integrated correctly if no dead pixel affects the peak profile, these dead pixels reduce the usable area as seen in the magnification of the diffraction image (Fig. 5.6b). As the flatfield correction file includes a list of pixels with high probability of counting errors (section 4.2.2) more pixels with zero value are produced in the correction procedure. Double sized pixels at the chip boundaries receive a higher counting rate and thus have a higher probability to be marked as an untrusted pixel. Therefore the structure of the modules with 16 chips can be seen in parts of the corrected image (Fig. 5.6c). In addition a pixel with zero count state expands into 2 to 4 pixels in the corrected image due to the distortion corrections (section 4.3). The permanent dead pixels of the detector, the untrusted pixel mask in the flatfield correction and the distortion correction lead to 9 % randomly distributed dead pixels in a corrected images.

By applying the two defect reduction techniques described above to the data, the corrected image shown in Figure 5.6c was obtained. The significant reduction of the randomly distributed dead pixels to 3% can be seen in the magnification Figure 5.6d.

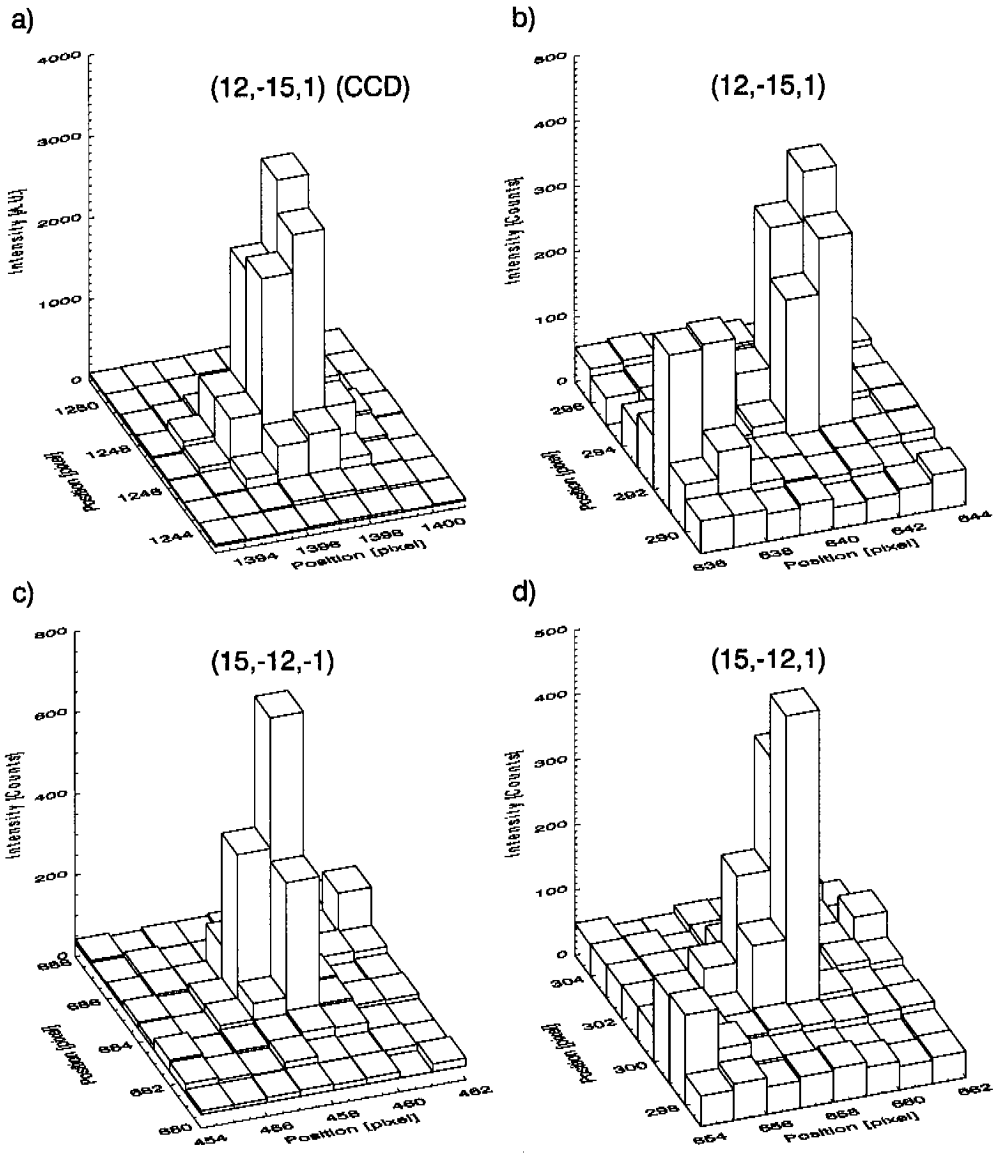

Figure 5.4: Bragg reflection profiles are well represented when measured with a CCD detector with small pixels of 80×80 μm^2 (a), but only coarsely sampled with the PILATUS 1M detector with its 217×217 μm^2 pixel (b–d). All four reflections are symmetry related as indicated by the Miller indices (h, k, l) written at the top of each Figure.

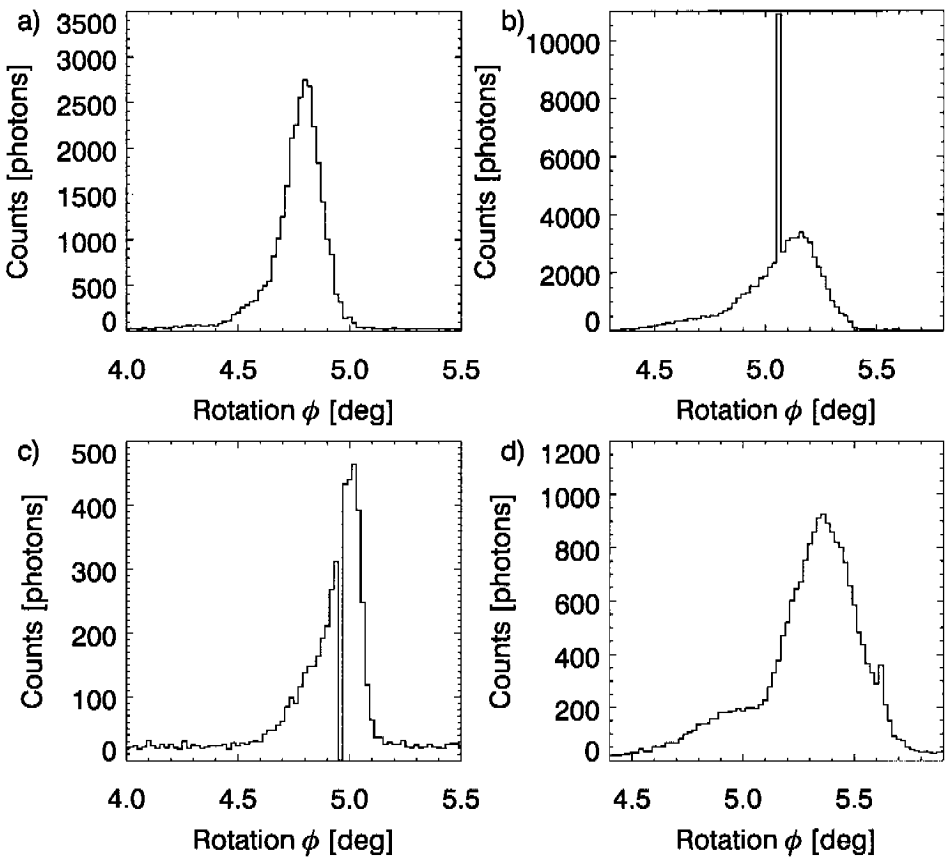

Figure 5.5: ϕ–profiles of Bragg reflections recorded with the PILATUS 1M detector. Counting errors can be detected and repaired if two conditions are fulfilled: many sample points have been acquired for the profile and the counting error is either unreasonably high or low. a) A typical profile without error. b) Counting errors with high values (*hot pixels*). c) Counting errors with zero count state (*cold pixels*) can be detected if the background is not vanishing. d) The peak at $\phi = 5.62°$ was not detected by the scanning algorithm.

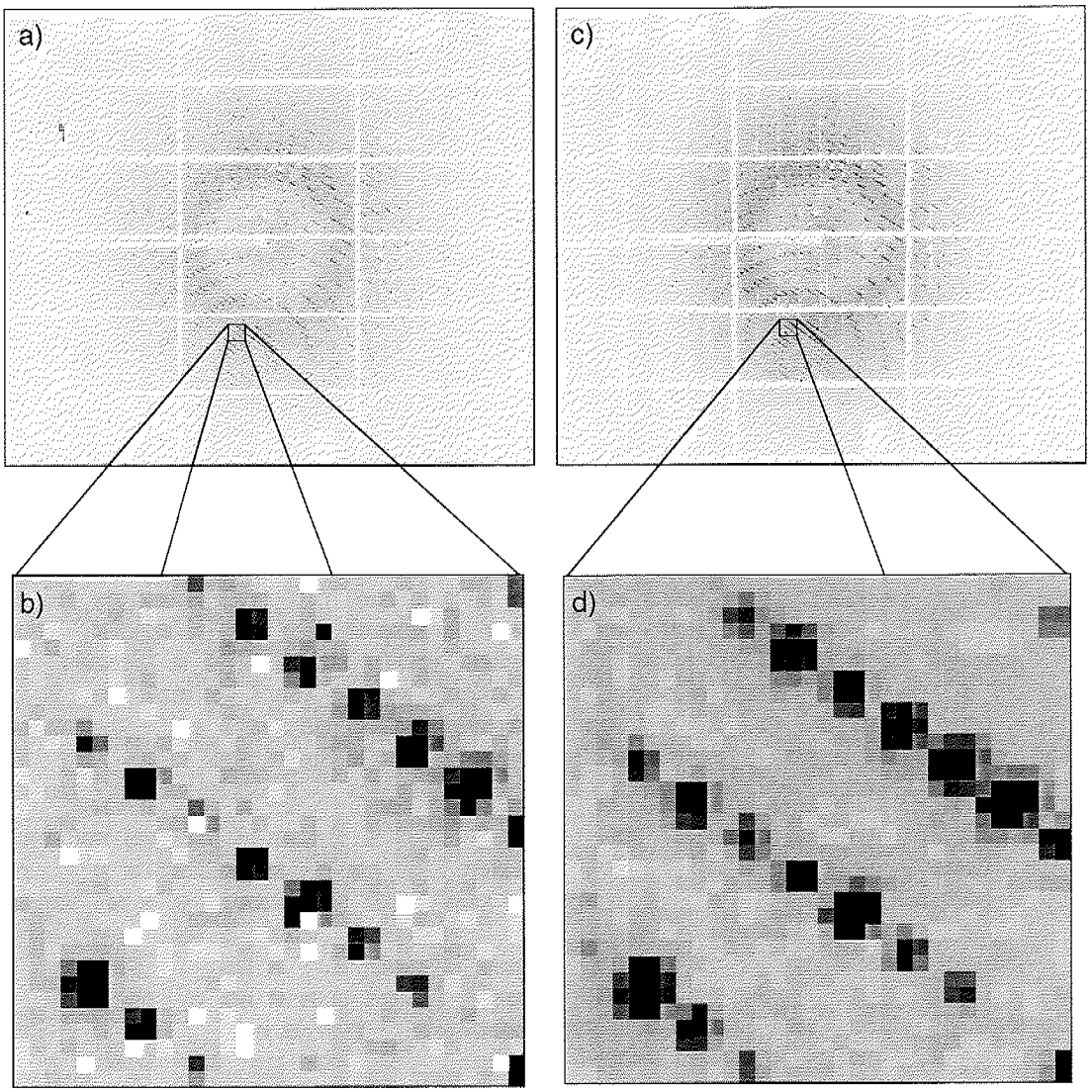

Figure 5.6: A diffraction image of a thaumatin crystal. a) The raw image recorded with the PILATUS 1M detector at the protein crystallography beamline X06SA of the SLS. c) The corrected diffraction image. The magnifications (b and d) show the reduction of the random distributed dead pixels which are marked white.

5.3 Protein Crystallography with the PILATUS 1M Detector

G. Hülsen, Ch. Brönnimann, E.F. Eikenberry and A. Wagner, *J. Appl. Crystallogr.*.

The detector performance was characterized with protein crystallography experiments. To use this new detector type, generous amounts of beam–time were allocated at the protein crystallography beamline X06SA of the SLS. First only one bank was tested and the results were used to optimize the detector system. Finally the complete PILATUS 1M detector was incorporated in the beamline system. The experiments were especially useful for the distortion calibration (section 4.3), which was optimized to meet the demands of these experiments.

An experimental drawback of the PILATUS 1M detector system is that during an experiment only raw images are collected. The image corrections are time consuming and are performed after the data collection. Therefore no pre–analysis of the crystal can be done and thus the quality of the crystal could only be estimated by investigating the raw images visually.

The experiments were performed with the defect reduction technique described in the previous section. In addition to crystallographic experiments, the counting defects were studied by recording defined *spots* of a tantalum mask. Both, coarse and fine ϕ–sliced datasets were recorded and analyzed with a standard crystallographic processing software.

Journal of Applied Crystallography

ISSN 0021-8898

Received 4 October 2005

Protein Crystallography with a Novel Large Area Pixel Detector

Gregor Hülsen,* Christian Broennimann, Eric F. Eikenberry and Armin Wagner

Paul Scherrer Institut, 5232 Villigen PSI, Switzerland. Correspondence e-mail: gregor.huelsen@psi.ch

The PILATUS 1M detector, developed at the Paul Scherrer Institut (PSI), is a single photon counting hybrid pixel detector designed for macromolecular crystallography. With more than 1 million pixels covering an area of $243 \times 210\ \mathrm{mm}^2$, it is the largest such device constructed to date. The detector features a narrow point spread function, very fast readout and a complete absence of electronic noise. Unfortunately this prototype detector has numerous defective pixels and sporadic errors in counting that complicate its operation. With appropriate experimental design we were largely able to work around these problems and successfully demonstrate the application of this technology to structure determination. Conventional coarse ϕ-sliced data were collected on thaumatin and a refined electron density map was produced that showed the features expected of a map at 1.6 Å resolution. The results were compared with the performance of a reference charge-coupled device (CCD) detector: the pixel detector is superior in speed, but showed higher R-factors because of the counting errors. Complete fine ϕ-sliced datasets recorded in the continuous rotation mode showed the predicted advantages of this data collection strategy and demonstrated the expected reduction of R-factors at high resolution. A new readout chip has been tested and shown to be not subject to the defects of its predecessor; a PILATUS 6M detector incorporating this new technology is under construction.

© 2006 International Union of Crystallography
Printed in Great Britain – all rights reserved

1. Introduction

Crystallography is the principal technique for determining macromolecular structures at atomic resolution and uses advantageously the high intensity of 3rd generation synchrotron X-ray sources (Sussman *et al.*, 1998). Macromolecular crystallography experiments benefit also from excellent beamline equipment, recent software advances and modern X-ray detectors (Gruner *et al.*, 2002; Plaisier *et al.*, 2003). However, the latter do not take full advantage of the brightness of modern synchrotron sources.

Among other attributes, an ideal detector for these experiments would have quantum limited photon detection and a short readout time with no readout noise. Hybrid pixel array detectors, originally developed for high energy physics experiments, have the potential to meet these requirements (Gemme, 2003; Schnetzer, 2003). The technology of these detectors features a two dimensional array of p–n diodes connected to a readout chip which is designed in complementary metal oxide semiconductor (CMOS) technology. In the design reported here, each pixel in the readout chip has a low noise amplifier, a comparator and a digital counter. X-rays are recorded in single photon counting mode and data thus are stored digitally at the earliest possible stage. This architecture leads to several advantages over current detectors:

- The quantum efficiency (Q.E.) of the detector is limited only by the absorption properties of the sensor. The Q.E. of a 300 μm silicon sensor is 0.98 for 8 keV (1.5 Å) X-rays, near the ideal limit of 1.0, but decreases for higher X-ray energies (0.73 for 12 keV (1.0 Å) X-rays).
- No detector noise is added to the signal.
- Readout time is reduced to a few milliseconds.
- The counting rates are matched to beam intensities at protein crystallography beamlines at 3rd generation synchrotrons.
- The detector is not sensitive to X-rays during readout; therefore no mechanical shutter is required.
- The detector has a very sharp point spread function (PSF) of one pixel, which allows better resolution of adjacent reflections.
- Low energy X-rays can be suppressed by the comparator.

The technology also introduces some disadvantages. First, to cover a large area, a pixel detector is built of individual modules between which a small region is insensitive to X-rays (Fig. 1). Second, counting detectors have rate limitations, in contrast to integrating detectors, such as CCD detectors or integrating pixel detector designs (Renzi *et al.*, 2002). Third, the better spatial resolution due to the sharp PSF is compromised by larger sized pixels. However, in crystallographic experiments the separation of reflections can be increased by a larger sample to detector distance, thus requiring a larger number of pixels to acquire a high number of reflection orders. The larger distance reduces isotropic background radiation, falling off by $1/r^2$, and therefore increases the signal to background ratio.

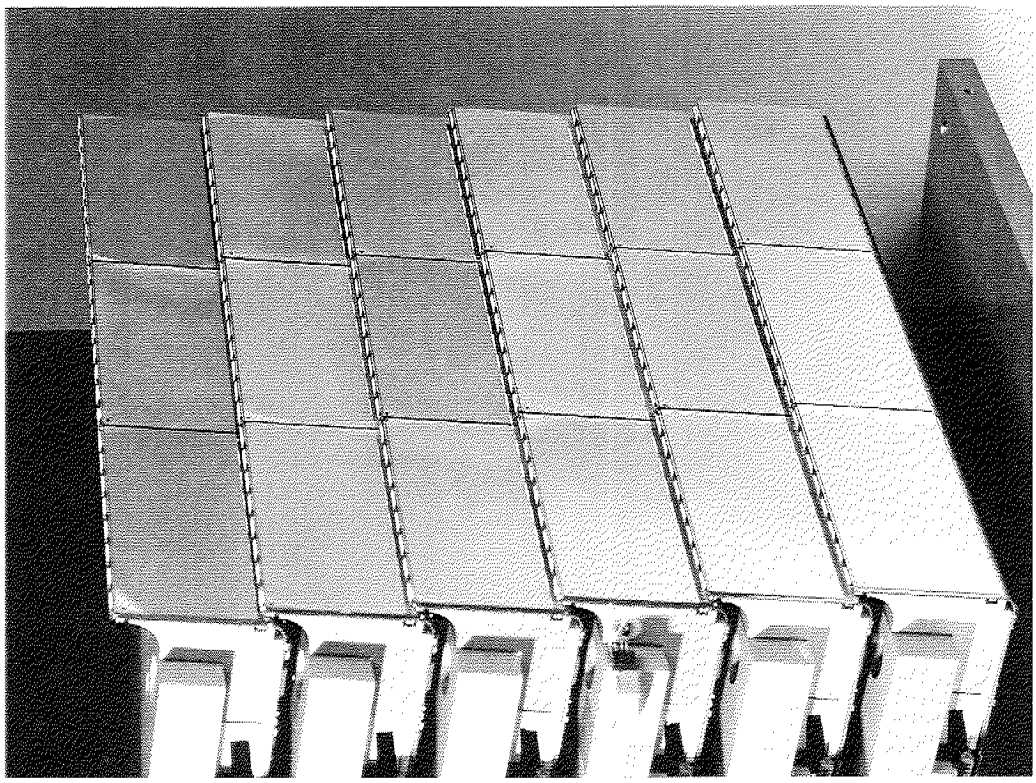

Figure 1
The Pilatus 1M detector. The sensitive surface of the detector is provided by 18 individual modules. The modules are tilted by 6° and do overlap.

PILATUS 1M, the first large area pixel detector, was designed for the protein crystallography beamline X06SA of the Swiss Light Source (SLS) at PSI. The detector covers an area of $243 \times 210\,\text{mm}^2$ with 1120×967 pixels (Fig. 1). It operates in single photon counting mode at room temperature and has noise-free readout in less than 5.9 ms. A description of the detector is given in (Broennimann *et al.*, 2005). The prototype detector suffers from two types of defects: (i) it contains a high number of dead pixels and (ii) the digital counter can switch into a random count state because of a subtle design fault (App. A). Despite these defects, which could be largely overcome by appropriate measuring techniques, the detector has been successfully used for protein crystallography and its potential could be demonstrated. In addition to conventional coarse ϕ-sliced experiments, fine ϕ-sliced datasets were recorded. In the absence of readout noise, the latter technique is proposed to improve data quality (Dauter & Wilson, 2001). And, the short readout time decreases the time needed to collect datasets of several thousand images. The results of experiments performed with the PILATUS 1M detector were compared to the performance of two CCD detectors (Mar CCD165 and Mar CCD225, Mar USA, Inc., Evanston, IL, USA).

1.1. Advantages of fine ϕ-slicing

One important step in the analysis of diffraction data is to separate the net intensity of the recorded Bragg reflections from the background radiation. The integrated intensity, I, of a reflection is the sum of counts of the pixels in the peak region, P, less the background, B. The background under the reflection is estimated in the recorded images from nearby pixels in the two dimensions of the detector plane and from pixels of the peak region at different rotation angles, ϕ, of the crystal. The boundary between background and peak region is found by fitting a three dimensional profile to the reflection (Diamond, 1969; Rossmann, 1979). The reflection profile is usually well represented in the detector plane but the rocking curve, i.e. the ϕ-profile of the reflection, is only coarsely sampled, as illustrated in Figure 2a. With the large rotation increment, $\Delta\phi$, of typically 1°/image, the reflection is recorded in one image and the peak position is poorly defined in this dimension. Because the reflection moves slightly in the two dimensions of the detector plane as it passes through the Ewald sphere (Pflugrath, 1999), the boundary of background and peak region is not well defined in all three dimensions. Therefore the profiles are not fitted at the precise position of the reflections. A large rotation increment minimizes the number of images of a dataset. However, reflections must not overlap in the plane of the detector. In fine ϕ-slicing experiments the rocking curve of the reflection is sampled more finely (Fig. 2b) and thus the position of the reflection is much better defined. In principle the rotation increment $\Delta\phi$ should be considerably smaller than the width of the rocking curve, σ_ϕ, and it is recommended (Kabsch, 2005) to set the rotation increment to

$$\Delta\phi \simeq \frac{1}{5}\sigma_\phi \,. \qquad (1)$$

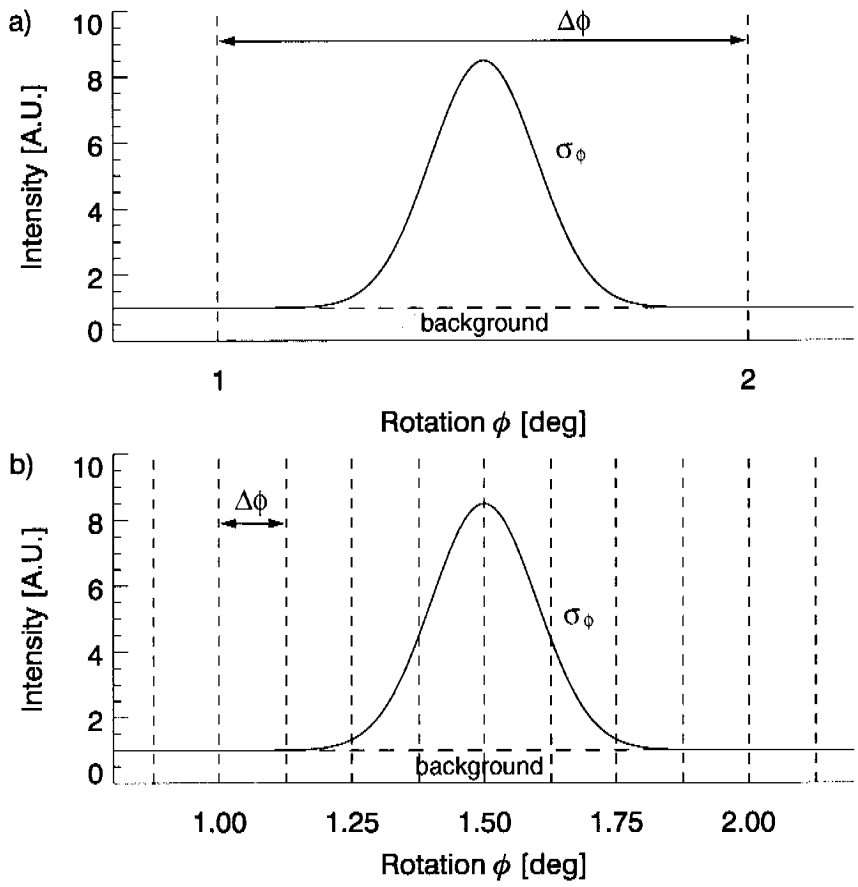

Figure 2
Rocking curve of a Bragg reflection passing through the Ewald sphere with a width σ_ϕ 0.1°. a) The intensity of the reflection is sampled in one image with a rotation increment $\Delta\phi$ = 1°/image. b) With finer sampling the position of the reflection is much better defined and less background is included in the integration.

The width of the rocking curve is usually expressed by the mosaicity of the crystal, which is the width of the reflecting range, as defined in (Kabsch, 1988). Throughout this paper we follow this definition of the crystal mosaicity. In fine ϕ-sliced data the mosaicity can be deduced from the standard deviation of the rocking curve as shown in Figure 2b and in this case is 0.1°. As the rocking curve is not available in coarse ϕ-sliced experiments, the mosaicity, reported by crystallographic integration programs, is a refinement parameter. In the example shown in Figure 2 the rotation increment should be, according to equation 1, around 0.02°/image.

A minimum amount of background should be included in the integration because the variance of the background is added to the variance of the intensity of the Bragg reflection. As the measurement of X-rays is Poisson distributed, the standard deviation of the estimation of m photons is

$$\sigma(m) = \sqrt{m}\,. \tag{2}$$

The standard deviation of the reflection intensity $I = f(P, B)$ is

$$\sigma(I) = \sqrt{P + B}\,. \tag{3}$$

The quality of the measurement can be defined by the ratio of the intensity to its standard error $I/\sigma(I)$:

$$I/\sigma(I) = \frac{I}{\sqrt{P + B}}\,. \tag{4}$$

Therefore the accuracy of a measurement is higher for lower background. In the first example described above, background from the left and right side of the reflection is unnecessarily included in the peak intensity (Fig. 2a) whereas in the fine ϕ-sliced experiment this background can be excluded (Fig. 2b). Another consequence of equation 4 is that high intensity reflections are less affected by background than low intensity reflections. Finer ϕ-slicing should therefore especially increase the data quality of weak reflections in the high resolution shells, which should increase the quality of the structure determination. Furthermore, small anomalous differences, important for phasing in multiple- or single-wavelength anomalous diffraction experiments, would be measured with higher accuracy.

If pixels are significantly larger than the width of the reflection in the detector plane, unnecessary background is also collected. The background should in this case be decreased by increasing the specimen to detector distance, but this may require a larger detector.

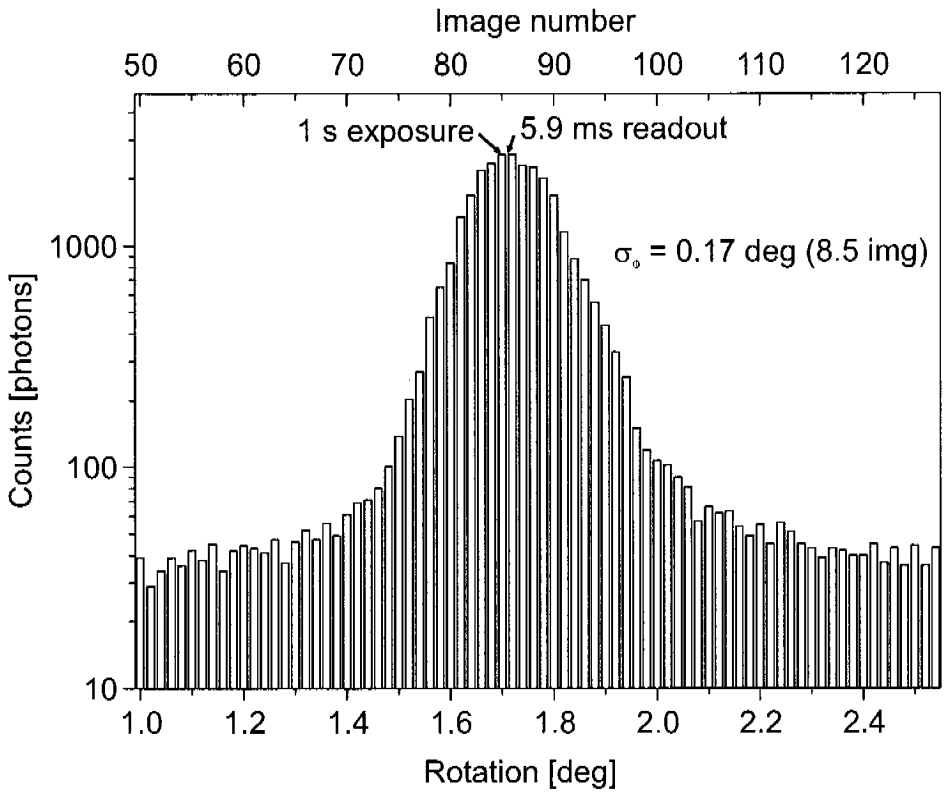

Figure 3
Typical fine ϕ-sliced profile on a logarithmic scale of a Bragg reflection as it passes through the Ewald sphere as measured with the PILATUS 1M detector with $\Delta\phi = 0.02°$/image. The profile was redrawn to illustrate the continuous sampling rotation mode of the detector: the dead time of 5.9 ms (not to scale), due to the readout of an image, leads to a 0.59 % reduction of the measured intensity for the 1 s exposures. The sampling theorem ensures that the ϕ-profile can be reconstructed with full accuracy from the fine ϕ-sliced data. The dead time between exposures therefore does not represent any loss of information.

1.2. Continuous sample rotation mode

Readout noise, added to each image by most detector technologies, prohibits fine ϕ-sliced experiments (Pflugrath, 1999). In addition, a long dead time, t_d, makes these experiments very time consuming because the number of images is significantly increased. For many widely used detectors t_d is a few seconds and is the sum of the readout time, the time needed for shutter synchronization and the data transfer time.

With the PILATUS 1M detector these experiments are performed using a novel data collection mode at synchrotrons: the crystal rotation is started and images are continuously recorded using the electronics of the detector as the shutter. Thus, the dead time of experiments with this detector is equal to its very short readout time and the utilization of both the detector and the X-ray source is significantly increased. Furthermore synchronization with a mechanical shutter is no longer needed. However, without shutter operation the sample is not protected against radiation damage during the dead time. Therefore t_d should be small, as is the case for the PILATUS 1M detector. Figure 3 shows a fine sampled ϕ-profile of a reflection recorded with the PILATUS 1M detector in this data collection mode. Detector dead time scales the intensity but does not change the profile shape as long as enough sample points have been acquired (Eq. 1). Thus, fine ϕ-slicing ensures that the ϕ-profiles can be reconstructed with full accuracy.

The time needed for experiments using the PILATUS 1M detector in this data collection mode or a CCD detector (Mar CCD165) can be compared. The PILATUS 1M detector has a readout time of 5.9 ms and no additional time is needed in the continuous sample rotation mode. With an exposure time of 1 s, 1.4 h are needed to perform a fine ϕ-sliced experiment with 5000 images and a conventional coarse ϕ-sliced dataset with 180 images is collected in 3 min. The CCD detector is normally operated with an overhead of 2.5 s. The synchronization of the shutter and goniometer adds approximately 0.5 s to this time, leading to a dead time of 3 s for this CCD detector. Thus, the fine ϕ-slicing experiment takes five hours and the coarse ϕ-slicing experiment is finished in 12 min, using the identical exposure time of 1 s.

2. Methods

2.1. Experimental setup

All the data presented here were collected at the protein crystallography beamlines X06SA and X10SA of the SLS. The X-ray wavelength was 1.0 Å and the exposure times were 1 s, unless otherwise noted. Since the flux was too high for fine ϕ-sliced experiments with this exposure time, the X-ray intensity was reduced by filters and beam confining slits to 2 % of the initial beam intensity. The PILATUS 1M detector was mounted on

an additional translation stage, allowing horizontal positioning of the detector to micron precision, perpendicular to the central beam direction. The diffraction data were collected from flash frozen (100 K) thaumatin and insulin crystals, obtained as described in (Schulze-Briese *et al.*, 2005). For the experiments performed with the pixel detector two thaumatin crystals (#1 and #2) from the same batch were used. One thaumatin crystal (#3) grown under the same conditions from a different batch and one cubic Zn-free insulin crystal (#4, space group $I2_13$, crystal size $180 \times 180 \times 140\ \mu m^3$) were used in the experiments with the CCD detectors. In a fine ϕ-sliced experiment the insulin crystal was 5 times scanned. The rotation increment and exposure time was decreased successively (0.5, 0.25, 0.1 and 0.05°/image with 10, 5, 2 and 1 s/image). The first scan was repeated at the end to monitor possible degradation of the crystal during the experiment. Thus, the angular rotation speed and the flux of the beam is constant for all 5 scans.

For flatfield calibration, the detector was placed 90° with respect to the central beam direction to minimize patterns in the flatfield image, caused by scattering of mechanical parts. At this position the detector surface was illuminated with fluorescence light (1.0 Å) from a solution of KBr. The images were collected at a sample to detector distance of 125 mm because the geometry of the PILATUS 1M detector causes this calibration to work best when the distance is the same as that used in the crystallographic experiments.

2.2. Data correction and processing

After the experiments the images of the PILATUS 1M detector are corrected for flatfield inhomogeneity. Each image is multiplied with an intensity calibration file, i.e. flatfield corrected (Barna *et al.*, 1999; Broennimann *et al.*, 2004). The calibration file also blanks out unreliably counting pixels, resulting in 9 % dead pixels in a corrected image.

The images need to be corrected for spatial distortion (Hülsen *et al.*, 2005). Within a module of the detector the pixel positions are accurate to sub-micron precision because the sensor is fabricated with photolithographic processes. As the 300 μm silicon sensor is much thicker than the thin phosphor screens of CCD detectors ($\sim$ 30 μm), a considerable parallax effect distorts the images. A parallax back transformation is carried out to determine the impinging position on the sensor surface. A second source of distortion is the mechanical deviation of the modules from their assumed positions. Therefore the pixel positions of each module are adjusted to the real position in space. A 6° tilt of the modules creates a shingled surface of the detector. To process the data with standard crystallographic software the detector surface is projected onto a virtual plane in front of the detector. The parallax effect and the detector geometry require correction files for each experimental setup. After the distortion correction, the standard deviation of the pixel position from a perfect grid is 0.31 pixels.

The active area of the PILATUS 1M detector is reduced by the insensitive areas between modules. In addition, dead pixels are randomly distributed in the detector area. In Figure 4a a section of a diffraction image recorded with the pixel detector is shown. The dead pixels are marked white. As reflections from diffraction experiments can only be integrated correctly if no dead pixel affects the peak profile, these dead pixels reduce the usable area significantly. Therefore datasets were recorded twice. First the total rotation range was scanned and after the detector translation, the second dataset was recorded. The detector was translated by one pixel (217 μm) using the horizontal translation stage. By merging the two datasets, the dead area caused by pixel defects could be reduced to 3 %. A pixel value of the corrected image (Fig. 4b) represents the average information of two measurements, the value of one measurement if one pixel was dead or zero if both were dead.

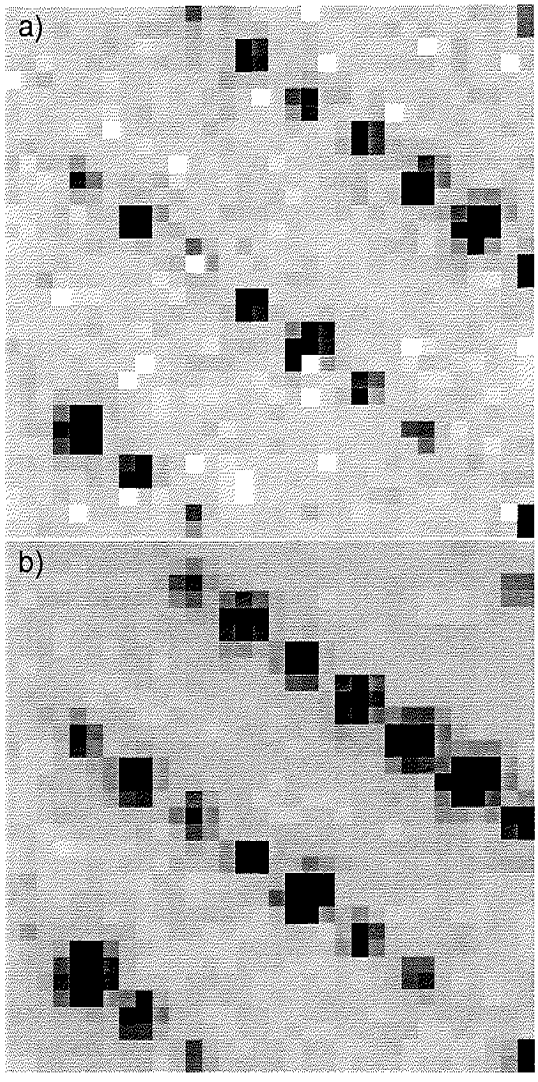

Figure 4
A section of a diffraction image of a thaumatin crystal recorded with the PILATUS 1M detector. a) The raw image with dead pixels (marked white). Reflections with such pixels in the neighborhood must be excluded from the analysis. b) The corrected image shows that dead pixels are successfully reduced by the translation procedure of the detector.

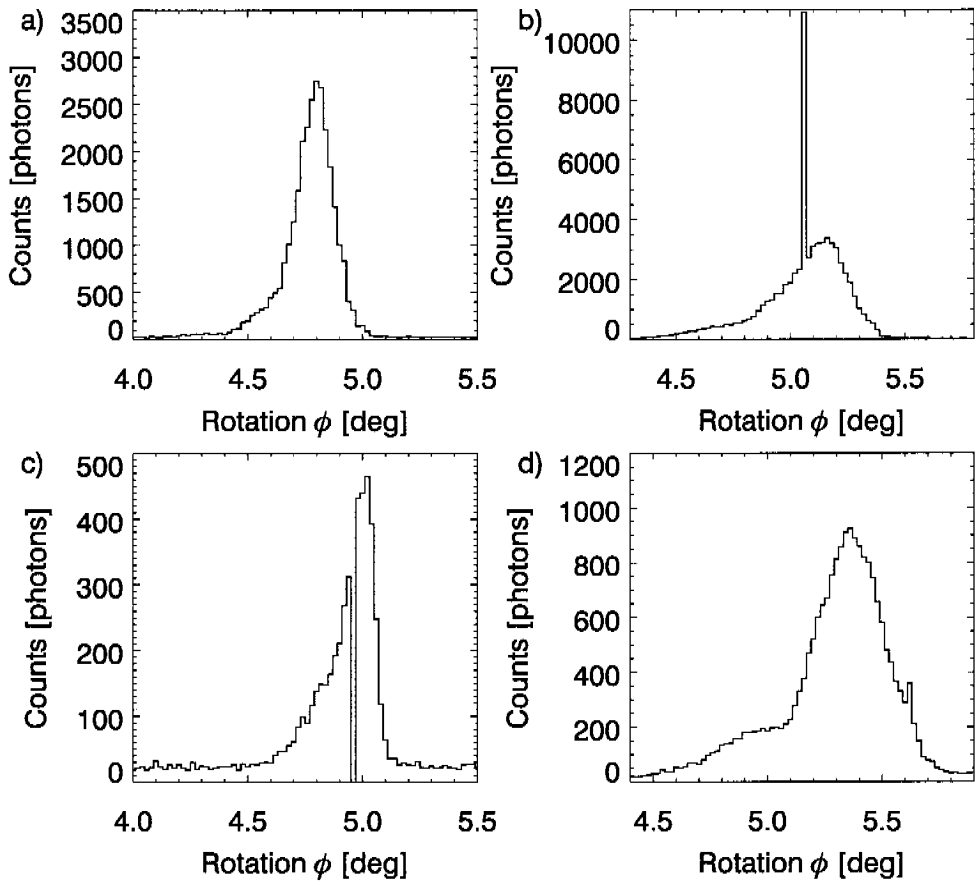

Figure 5
ϕ-profiles of Bragg reflection recorded with the PILATUS 1M detector. a) A typical reflection profile without error. b-c) Random counting errors can be detected and corrected if two conditions are fulfilled: many sample points have been acquired for the profile and the counting error is either unreasonably high or low. d) The outlier at $\phi = 5.62°$ was not detected by the semiautomatic algorithm.

Fine ϕ-sliced datasets could in addition be corrected for random counting errors (App. A). This is essential for these experiments because the significantly longer total exposure time increases the number of counting errors in the data. The errors can be detected to a certain degree in the ϕ-profiles of Bragg reflections (Fig. 5). A semiautomatic algorithm was developed which scans through the data and removes many of these errors. Each ϕ-profile is fitted to an average reflection profile in all three dimensions. Detected outliers are replaced by an average value of the neighboring pixels. Despite this routine, an unknown number of errors remain, which cannot be detected (Fig. 5d).

Using the *XDS* package (Kabsch, 1988; Kabsch, 1993) the datasets were indexed and the intensities of the reflections calculated and scaled. This crystallographic analysis package has been revised and could successfully analyze the large datasets of the fine ϕ-sliced experiments.

The quality of the datasets is expressed in the reliability factor, or R-factor, which is defined as (Drenth, 1994)

$$R_{\rm merge} = \frac{\sum_{hkl} \sum_i^{n_{hkl}} | < I > - I_{hkl,i}|}{\sum_{hkl} \sum_i^{n_{hkl}} I_{hkl,i}}, \qquad (5)$$

where $I_{hkl,i}$ is the intensity of the ith reflection out of a set of symmetry related reflections hkl with multiplicity n_{hkl}. The ratios $I/\sigma(I)$ are another indication for the quality of a dataset.

3. Experimental results and discussion

3.1. Coarse ϕ-sliced experiments

A conventional coarse ϕ-sliced experiment on a thaumatin (crystal #1) was performed with the PILATUS 1M detector at beamline X06SA. A rotation range of 120° was measured using a rotation increment of 0.5°/image. Table 1 summarizes the results of the experiment.

The pixel detector collected the data with a completeness of 99.9 %. This value could only be achieved by the translation technique described above. Loss of reflections, due to the insensitive area between the modules, was no problem for this high symmetry crystal. The standard deviation of the reflection position ($\sigma_{\rm spot} = 0.5$ pixels) indicates that images could be spatially distortion corrected to a sufficient degree. The value below 10 % for the reliability factor shows that the defects of the prototype could be successfully compensated by the correction procedures. But the low value of 13 for the signal to noise ratio indicates that counting errors affect the data quality.

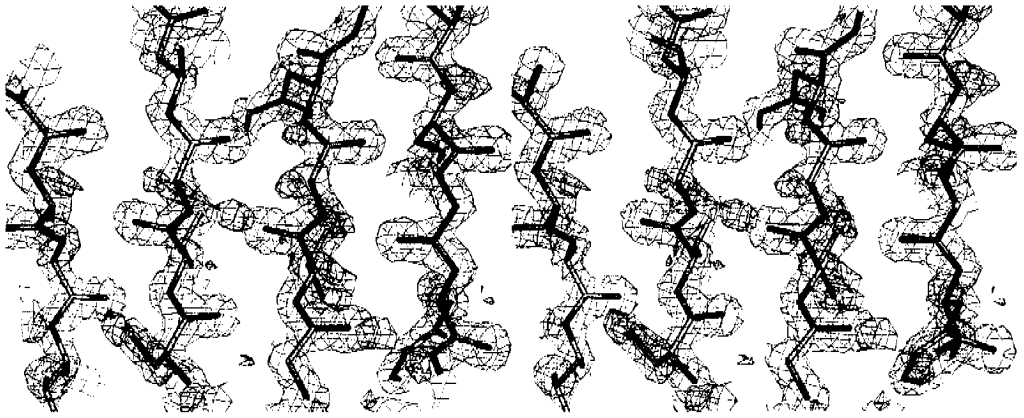

Figure 6
Stereo plot of a section of the electron density map of thaumatin after refinement (blue: $2F_o - F_c$, 2σ contour level, red: $F_o - F_c$, 2σ).

From the data obtained, the structure of the protein could be solved by molecular replacement using a structure model obtained by sulfur single anomalous dispersion (S-SAD) at beamline X06SA (Wagner, 2005). The subsequent isotropic refinement of the thaumatin structure against the measured diffraction data with the Crystallography & NMR system (CNS) (Brünger *et al.*, 1998) led to reasonable statistics (Table 1). In Figure 6 a stereo plot of a section of the electron density map after the refinement is shown (blue: $2F_o - F_c$; red: $F_o - F_c$; 2σ contour level; F_o are observed and F_c calculated structure factors). The map is relatively noisy, but shows all the features expected at 1.6 Å resolution.

The experiment was repeated with the Mar CCD165 detector, usually installed at the beamline X06SA, using identical experimental parameters but a different thaumatin crystal (#3). This crystal did not diffract as well as the one used in the experiment with the pixel detector. This can be seen in the lower completeness of 68.4 % in the highest resolution shell. However, the reliability factor and the signal to noise ratio of the dataset is more than a factor of two better for the CCD detector. This result shows that with the counting errors higher quality intensity measurements with the PILATUS 1M detector are not possible.

3.2. Fine ϕ-sliced experiments

Fine ϕ-sliced datasets, containing 5200 images were collected with the PILATUS 1M detector at beamline X06SA. The total rotation range of 104° was measured with a rotation increment of 0.02°/image. After the correction procedure (section 2.2), the mosaicity of the thaumatin crystal (#2) was determined by *XDS* to be 0.2°, which corresponds well with the value of 0.17° deduced from the rocking curve shown in Figure 3. To fulfill equation 1, the rotation increment of the dataset was reduced to 0.04°/image. This was done by adding pairs of images and scaling the resulting images down by a factor of two. Because of the absence of readout noise this procedure resulted in a dataset which is identical to an experiment with a rotation increment of 0.04°/image. Two more datasets were prepared by adding sets of 5 and 25 images together with an appropriate scaling factor. The three resulting datasets thus have oscillation ranges of 0.04, 0.1 and 0.5°/image.

The reliability factors as a function of the resolution shell are shown in Figure 7 and a summary of the finest and the coarsest dataset is listed in Table 2. Compared with the performance of the detector in the conventional coarse ϕ-sliced experiment (Table 1) the overall R-factor of the finest dataset (0.04°/image) differs by only 0.7 %. The higher number of counting errors due to the significant increase in exposure time could be successfully compensated by the correction algorithm (section 2.2). The 10 % better R-factor in the highest resolution shell indicates that weak reflections were much better acquired, which can however also be influenced by a difference in crystal quality.

Compared within the summed datasets, the data in the high resolution shells was considerably improved (Fig. 7). The difference of the R_{merge} for the finest and the coarsest dataset is 10 % in the highest resolution shell. No significant improvement is observed in the low resolution shells. Thus, the fine ϕ-sliced data demonstrate the beneficial effect of this data acquisition mode for weak reflections in the high resolution shells.

Table 1
Results of the analysis of thaumatin data for the coarse ϕ-sliced experiments using two detector systems and a rotation increment $\Delta\phi = 0.5°$/image. The performance of the detectors in the highest resolution shell is listed in parentheses. No refinement of the CCD-data was performed.

Detector	PILATUS 1M	Mar CCD165
Crystal	#1	#3
Crystal size [μm]	300 × 150 × 100	
Space group	92 ($P4_12_12$)	
Unit cell a, c [Å]	57.50, 150.89	57.78, 150.06
Diffraction statistics		
Resolution [Å]	70 - 1.6 (1.7 - 1.6)	
Completeness [%]	99.9 (99.9)	94.8 (68.4)
Unique reflections	34 320 (5 579)	32 580 (3 817)
Total observed	258 324 (41 040)	300 251 (29 070)
Redundancy	7.53 (7.36)	9.22 (7.62)
σ_{spot} [pixel]	0.50	0.32
R_{merge} [%]	9.5 (36.0)	4.6 (13.0)
Mean $I/\sigma(I)$	13.02 (5.17)	33.78 (13.35)
Refinement statistics		
R_{cryst} [%]; working set	19.4	
R_{free} [%]; free set	21.2	

Table 2
Results of the analysis of thaumatin data for the fine ϕ-sliced experiments with the PILATUS 1M detector. The performance of the detector in the highest resolution shell is listed in parentheses. The images with a rotation increment $\Delta\phi = 0.02°$/image were summed to give images with rotation increments equivalent to 0.5 and 0.04°/image, respectively (see also Figure 7 and text).

$\Delta\phi$ [°/image]	0.5	0.1	0.04
Crystal		#2	
Crystal size [μm]		300 × 150 × 100	
Space group		92 ($P4_12_12$)	
Unit cell a, c [Å]	57.60, 151.11	57.55, 150.86	57.55, 150.81
Diffraction statistics			
Resolution [Å]		70 - 1.6 (1.7 - 1.6)	
Completeness [%]	99.9 (99.8)	99.9 (100.0)	99.9 (100.0)
Unique reflections	34 377 (5 589)	34 393 (5 599)	34 393 (5 599)
Total observed	218 721 (30 239)	245 350 (39 074)	245 416 (39 314)
Redundancy	6.36 (5.41)	7.13 (6.99)	7.14 (7.02)
σ_{spot} [pixel]	0.59	0.64	0.74
R_{merge} [%]	11.8 (34.0)	10.2 (26.2)	10.2 (24.2)
Mean $I/\sigma(I)$	13.09 (5.67)	13.28 (7.04)	12.36 (7.24)

The reduction of the rotation increment per image leads to an increase in the effect of readout noise in data from CCD detectors. To verify this, a total rotation range of 30° was measured 5 times with one insulin crystal (#4) at beamline X10SA. The results of this experiment performed with the Mar CCD225 detector are shown in Figure 8. The comparison between the performance of the two detectors reveal the principle differences of the two detector types: it can be seen that the advantages of finer slicing are compromised by the readout noise of the CCD, which leads to a significant increase of the R-factors for smaller rotation increments, especially in the high resolution shells. This result is not caused by the degradation of the crystal which can be seen by comparing the first with the last scan. Furthermore, at the protein crystallography beamlines of the SLS shutter synchronization does not introduce any difficulties in data collection. This could be verified by inspection of the XDS analysis of the data. The mosaicity of the crystal ($\sim 0.1°$) would require a $\Delta\phi$ equal to 0.02°/image. But with the high R-factors already obtained at 0.05°/image, a further reduction of the rotation increment for finer ϕ-slicing was not performed.

4. Conclusions and outlook

The PILATUS 1M detector is the first large area silicon pixel detector designed for macromolecular crystallography. The performance of the detector was successfully investigated with crystallographic experiments. One important advantage of this detector is its fast readout time: conventional crystallographic datasets can be collected in less than 3 min. The dead pixels of the prototype could be largely compensated by detector translation: with this technique a completeness of 99.9 % was achieved for a high symmetry crystal. No limiting effect of the insensitive area between modules of the detector was found. The analysis of the crystallographic data shows that with the correction procedures reasonable R-factors could be obtained, but random counting errors affect the data quality. However, the structure of the protein could be solved and the refined electron density map is of good quality.

The theoretically predicted advantages of finer rotation increments have been verified. In contrast to data from CCD detectors, the quality of the high resolution data was largely increased by using a rotation increment smaller than the mosaic spread of the crystal. The duration of the experiments could be reduced by operating with continuous sample rotation, without mechanical shutter.

The analysis of the PILATUS 1M performance provided critical information for the development of the next generation pixel detector system. The readout chip of the new detector will be replaced by the significantly improved design of the PILATUS II chip. Outstanding data quality should be achieved, because the defects of the prototype chip have been eliminated in the new readout chip. A PILATUS 6M detector incorporating this new technology is under construction. With an expected framing rate of $\sim$ 10 Hz fine ϕ-sliced datasets can be recorded in the same time as conventional coarse ϕ-sliced datasets are currently collected with CCD detectors. Furthermore, conventional datasets potentially can be collected in a few seconds in the continuous rotation mode, depending on the experimental conditions.

Appendix A
Random counting errors

Because of a property of the counter design, random counting errors are possible when two X-ray photons arrive on a pixel within a short time interval, e.g. between t_1 and t_2. Below that interval the pixel electronics cannot resolve the two events and count a single event; at longer intervals the electronics can separate the events clearly. X-ray arrival times follow the interval distribution (Evans, 1955). With a mean rate of photon arrival events per pixel, a [γ/s/pixel], the average interval between events is $1/a$. The probability that the duration of a particular interval will be between t and $t + dt$ is

$$dP_t = ae^{-at}dt \; . \qquad (6)$$

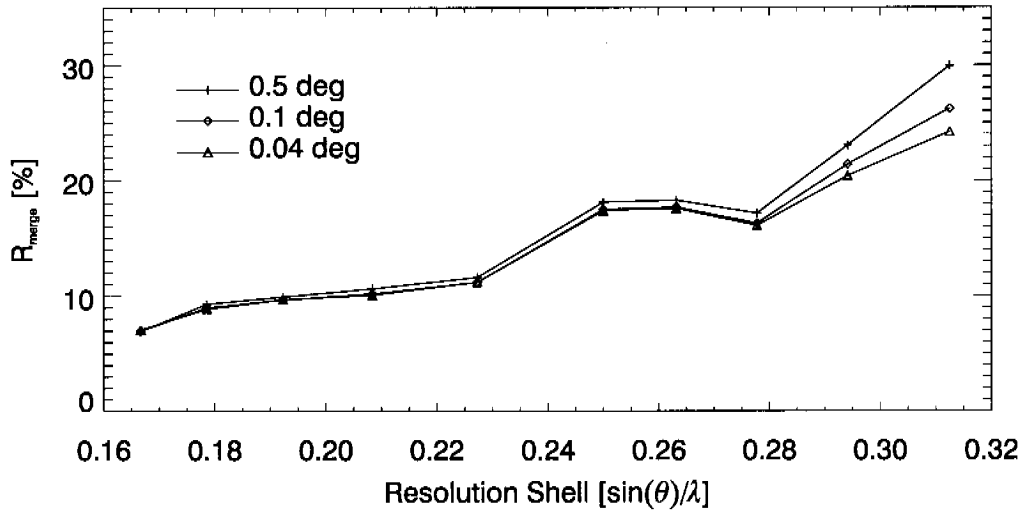

Figure 7
R_{merge} for datasets with decreasing rotation increments $\Delta\phi$ collected with the PILATUS 1M detector. A thaumatin crystal was scanned with $\Delta\phi = 0.02°$/image. The figure displays the quality of this dataset summed to larger rotation increments. The quality increases with finer rotation increment.

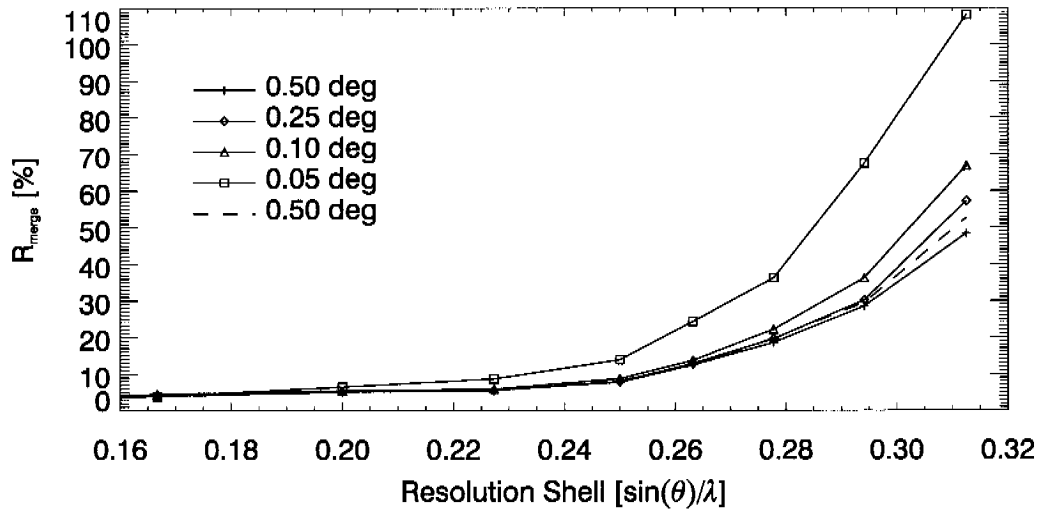

Figure 8
R_{merge} for experiments with decreasing rotation increments $\Delta\phi$ performed with the CCD detector. An insulin crystal was scanned 5 times. The last scan (dashed line) with $\Delta\phi$ equal to the first scan shows the degradation of the crystal. The quality of the dataset decreases with finer ϕ-slicing.

If N intervals are measured with q pixels, the number of intervals, n_c, between t_1 and t_2 is

$$n_c = Nq \int_{t_1}^{t_2} a e^{-at} dt \,, \tag{7}$$

$$= Nq \left(e^{-at_2} - e^{-at_1}\right) \,, \tag{8}$$

$$\approx Nqa(t_2 - t_1) \,, at \ll 1 \,. \tag{9}$$

If the probability is p that the counter switches into a random count state for a time interval between t_1 and t_2, then the number of counting errors in an image is

$$n_e = pn_c \,. \tag{10}$$

In a homogeneously illuminated image of the PILATUS 1M detector with a 1 s exposure and an average counting rate of $a = 2300\ \gamma$/s/pixel, $n_e = 50 \cdot 10^3$ counting errors were detected (5 % of the pixels). The time interval in which counting errors are likely is estimated from chip design simulations to be between $t_1 = 450$ ns and $t_2 = 650$ ns. Thus, in the exposure described above $n_c = 2300 \times 10^6 \times 2300 \times (650 - 450) \cdot 10^{-9} \approx 10^6$ (Eq. 9) and the probability, p, for a counting error is approximately 0.05.

For very low X-ray rates (background) a negligible number of counting errors occur ($n_e = 16$ for $a = 40\ \gamma$/s/pixel), but an increasing number of counting errors occur at higher rates, as in strong reflections with several 1000 γ/s/pixel.

Due to the counting errors, it is observed that the variance of intensity measurements for the prototype pixel detector is far above the theoretical expectation. To simulate crystallographic measurements under controlled conditions the following 'mask' experiment was performed. A 0.2 mm thick tantalum mask with a square matrix of 0.2 mm diameter holes on 5 mm centers was moved to 5 different positions in front of the detector. Images of the holes were recorded with the detector at each position of the mask. After image correction (section 2.2) the intensities of all spots were measured. The 5 intensities of each spot measured at the 5 mask positions were evaluated for mean and standard deviation. Spots contaminated by proximity to dead pixels were excluded from the analysis.

As discussed in the section 1.1, the standard deviation of an X-ray measurement follows equation 2. A factor η can be introduced to compare the theoretical standard deviation with the standard deviation of experimental measurements:

$$\sigma(m) = \eta\sqrt{m} \,. \tag{11}$$

For a quantum limited detector the factor η is unity. But the mask experiment verified that counting errors dominate measurements with the PILATUS 1M detector: the factor η is 7.5 for counting rates below 1000 γ/s/pixel and increases for higher counting rates. The origin of this problem is fully understood and has been solved by a redesign of the readout chip. This PILATUS II chip has a special logic which prohibits counting errors. Measurements have shown that a pixel can count more than $1.5 \cdot 10^6\ \gamma$/s/pixel without counting errors.

We thank M. Naef, H. Rickert, S. Streuli and F. Glaus of PSI for their help in fabrication of the PILATUS 1M detector and C. Schulze-Briese, T. Tomizaki and C. Pradervand for their help in the experiments at beamline X06SA of the SLS. Many thanks also to W. Kabsch for discussions and his help in processing our data with *XDS*. G. Hülsen acknowledges support from the Swiss National Science Foundation.

References

Barna, S. L., Eikenberry, E. F., Gruner, S. M. & Tate, M. W. (1999). *Rev. Sci. Instrum.* **70**(7), 2927–2933.

Broennimann, C., Bühler, C., Eikenberry, E. F., Horisberger, R., Hülsen, G., Schmitt, B., Schulze-Briese, C., Suzuki, M., Tomizaki, T., Toyokawa, H. & Wagner, A. (2004). *Synchrotron Radiation News*, **17**, 23–30.

Broennimann, C., Eikenberry, E. F., Henrich, B., Horisberger, R., Hülsen, G., Pohl, E., Schmitt, B., Schulze-Briese, C., Suzuki, M., Tomizaki, T., Toyokawa, H. & Wagner, A. (2005). *J. Synchrotron Radiat.* In the press.

Brünger, A. T., Adams, P. D., Clore, G. M., DeLano, W. L., Gros, P., Grosse-Kunstleve, R. W., Jiang, J. S., Kuszewski, J., Nilges, M., Pannu, N. S., Read, R. J., Rice, L. M., Simonson, T. & Warren, G. L. (1998). *Acta Crystallogr.* D**54**, 905–921.

Dauter, Z. & Wilson, K. S. (2001). *International Tables for Crystallography, Crystallography of Biological Macromolecules*, vol. F. Dordrecht: Kluwer Academic Publishers. Chapter 9.1.6.6.

Diamond, R. (1969). *Acta Crystallogr.* A**25**, 43–55.

Drenth, J. (1994). *Principles of Protein X-ray Crystallography*. Berlin: Springer Verlag.

Evans, R. D. (1955). *The Atomic Nucleus*. New York: MacGraw-Hill Book Company.

Gemmo, C. (2003). *Nucl. Instrum. Meth. A*, **501**(1), 87–92.

Gruner, S. M., Tate, M. W. & Eikenberry, E. F. (2002). *Rev. Sci. Instrum.* **73**, 2815–2842.

Hülsen, G., Broennimann, C. & Eikenberry, E. F. (2005). *Nucl. Instrum. Meth. A*, **548**, 540–554.

Kabsch, W. (1988). *J. Appl. Crystallogr.* **21**, 916–924.

Kabsch, W. (1993). *J. Appl. Crystallogr.* **26**, 795–800.

Kabsch, W., (2005). Personal communication.

Pflugrath, J. W. (1999). *Acta Crystallogr.* D**55**, 1718–1725.

Plaisier, J. R., Koning, R. I., Koerten, H. K., van Roon, A. M., Thomassen, E. A., Kuil, M. E., Hendrix, J., Broennimann, C., Pannu, N. S. & Abrahams, J. P. (2003). *Nucl. Instrum. Meth. A*, **509**, 274–283.

Renzi, M. J., Tate, M. W., Ercan, A., Gruner, S. M., Fontes, E., Powell, C. F., MacPhee, A. G., Narayanan, S., Wang, J., Yue, Y. & Cuenca, R. (2002). *Rev. Sci. Instrum.* **73**(3), 1621–1624.

Rossmann, M. G. (1979). *J. Appl. Crystallogr.* **12**, 225–238.

Schnetzer, S. (2003). *Nucl. Instrum. Meth. A*, **501**(1), 100–105.

Schulze-Briese, C., Wagner, A. & Oetiker, M. (2005). *J. Synchrotron Radiat.* **12**, 261–267.

Sussman, J. L., Lin, D., Jiang, J., Manning, N. O., Prilusky, J., Ritter, O. & Abola, E. E. (1998). *Acta Crystallogr.* D**54**, 1078–1084.

Wagner, A. (2005). In preparation.

Chapter 6

Discussion

Detector Development, Calibration and Test

The PILATUS 1M detector is the first large area silicon pixel detector for macromolecular crystallography. After approximately five years of development this prototype could be assembled and tested. The dominant part of the work presented here was to build the detector. The defects of the prototype were analyzed and the system was calibrated. Finally, crystallographic experiments were performed and the collected data were successfully processed and analyzed.

First, the DMILL wafers were screened for good readout chips. Unfortunately an average number of 4.7 % defective pixels were found even in *good* chips; the best chip found had approximately 100 dead pixels ($\sim$ 3 %). The different steps of the bump bonding process could be experimentally optimized. Most of the modules have only 0.05 % bump defects. The 4.75 % dead pixels, randomly distributed in the active area of the detector, cause problems when recording sharp Bragg reflections in crystallographic experiments. This type of detector defect could be partially compensated by shifting the detector by one pixel between exposures. With this technique the requirement for high completeness of the data was always achieved.

Already within the production phase, the counting performance of the detector was investigated. The most valuable information was extracted from flatfield measurements, with the important result that counting errors were the dominating source of problems of the prototype. The experiments showed that at this stage of the development the detector performance was not limited by the physical quantum limit, but by the above mentioned drawbacks. This problem could be bypassed by a high redundancy of the measurements. This can either be obtained by repeated measurements or fine ϕ–slicing crystallographic experiments. The former technique was successfully used by our collaborators at SPring–8[1], whereas the latter will be discussed below.

The detector was trimmed for threshold variations, calibrated for individual pixel response and was corrected for spatial distortions. The adjustments of the thresholds was done with a calibration signal sent to each pixel and the wide distribution of 140 electrons could be significantly narrowed to 42 electrons. This result is biased by the fact that the verification of the

[1]Japan Synchrotron Radiation Research Institute, 1-1-1 Kouto, Mikazuki-cho, Sayo-gun, Hyogo 679-5198, Japan

calibration was done with the internal signal, which is not constant across the readout chip. An even better calibration can be obtained by trimming the detector directly with monochromatic X–rays of energy equal to the target threshold.

For the individual X–ray response of each pixel a well developed calibration technique for CCD detectors was adopted. The real pixel response was measured by a flatfield illumination. It has been shown that some modules have a distinctive pattern with higher and lower responding areas. These patterns together with the usual variation in pixel response could be adjusted.

The three sources of spatial distortions of the detector were analyzed. The parallax effect is the smallest contribution for the overall distortion of an image. Bragg reflections are shifted by a fraction of a pixel, depending on the angle of incidence and on the photon energy. As an example, for a photon energy of 12 keV, reflections recorded under a high angle of incidence ($\sim 50°$) are shifted by approximately 0.5 pixel. The effect was simulated and for a given energy a parallax factor could be calculated. This simulated dependency could be verified with an experiment. A parallax back transformation was developed using the parallax factor for a calculated angle of incidence.

The mechanical mounting of the modules into the detector frame introduces a deviation of a pixel position from its assumed position. This deviation is a composition of all mechanical mounting steps during the detector construction: the silicon hybrid with the sensor is glued onto the module, which is screwed on the bank and the bank itself is mounted on the detector base plate. Between modules within a bank the mounting is precise to a fraction of a pixel (± 48 μm). Between banks the spacing is smaller then assumed, but with a much higher variation (± 302 μm). The varying amount of glue between the silicon assembly and the MCB as well as between the MCB and the module base leads to a variation of the sensor height of ± 249 μm. The sensors are well aligned and only slightly rotated in the detector plane.

The largest distortion is, however, caused by the tilt of the modules. The tilt of the modules was measured to be $5.83 \pm 0.08°$. This architecture was chosen to reduce the inter–bank spacing, but this is only true for large distances. In the top half of the detector the gap is nearly eliminated at typical experimental detector to specimen distances (< 200 mm), but shadows of the overlying modules lead to unusable pixel rows. In the bottom half no X–rays are blocked by the module periphery, but the apparent gap is significantly larger in comparison to the inter–bank spacing, measured perpendicular to the detector plane. At a typical detector distance, many pixels are displaced by more than 2 mm whereas at large distances the influence of the bank tilt is negligible. The conclusion is that the bank tilt does not reduce the insensitive area between banks at typical experimental detector distances. However, the correction procedures needed for this detector architecture have been developed and shown to work properly.

The distortion correction procedures developed for CCD X–ray detectors are based on the fact that image distortions are smoothly varying across the sensor surface. Images of a mask display this continuous distortion and can be used to calculate correction files. For the PILATUS 1M detector only the parallax effect meets this demand. Both the mechanical and the bank tilt are discontinuous distortions. Correction files are therefore calculated using the measurements of the detector geometry and the parameters of the experimental situation.

All three contributions of the distortion depend on the position of the detector with respect to the sample and primary beam. Thus the correction file must be recalculated for each experimental detector position and photon energy with the procedures developed in this work. After the distortion correction, mask and crystallographic images display the residual spatial error of

the PILATUS 1M detector. The distortion correction procedure was optimized and the spatial distortion error of the corrected images is only 0.31 pixel (70 μm).

The performance of the detector was successfully investigated with crystallographic experiments. The outstanding advantage of this prototype in comparison to commercially available CCD detectors is its fast readout time: conventional crystallographic datasets can be recorded in less than 3 min whereas it takes 15 min with a typical CCD system. The shifting technique provides a large usable active area without randomly distributed pixel defects. Therefore the large number of reflections needed for the structure calculation can be acquired. A completeness of 99.9 % was achieved for high symmetry crystals. No limiting effect of the insensitive area between modules of the detector on the completeness was observed.

The analysis of the crystallographic data shows that the reliability–factors (R–factors) for this prototype were rather high. No overall R–factor smaller than 9 % was found. R–factors obtained in identical experiments with state of the art CCD–detectors are on average a factor of two better. This is also true for the signal to noise ratio. The advantage of the noise–free single photon counting data collection is compromised by a high number of random counting errors in the Bragg reflections. However, from the data the protein structure could be refined and the calculated electron density map is of good quality and shows all the features expected at the measured resolution.

The theoretically predicted advantages of finer rotation increments were verified. In contrast to data from CCD detectors, the quality of the high resolution data could be increased by using a rotation increment smaller than the mosaic spread of the crystal. Counting errors could be detected in the ϕ–profile of the reflection in these experiments. An algorithm was developed, which scans through the dataset and corrects detected counting errors. However, counting errors can only be found if the value is significantly different from the expected value. Furthermore, the long duration of the total exposure time, due to the increase in number of images, leads to a significant increase in the number of counting errors. However, by using a counting error correction algorithm, similar data quality was achieved for fine and coarse ϕ–sliced experiments. The duration of the experiments could be reduced by operating with a novel data collection technique for protein crystallography at synchrotrons: the continuous sample rotation technique without mechanical shutter. Although a framing rate of only 1 Hz was used for the experiments, datasets consisting of 9000 images could be recorded within 2.5 h.

My contribution to the project

The detector was designed and constructed by the detector development group of the SLS at PSI during the years 1997 to 2003. I was involved in most of the steps of the production after starting my work in the year 2000, but also in the following tests and analysis of the detector:

- Development of the PILATUS I (SLS06) chip test station and screening of the 24 DMILL wafers.
- Debugging and screening of the electronic boards.
- Optimization of the bump bonding process.
- Construction and testing of 32 modules.

- Incorporation of the PILATUS 1M detector into the protein crystallography beamline X06SA of the SLS.
- Experiments at the beamlines X06SA and X04SA (materials science) of the SLS.
- Analysis of the data.
- Development of the PILATUS II readout chip and design of the PILATUS 6M detector (see below).

The following points where done by myself:

- Adaptation of a Monte Carlo simulation for the parallax effect for the use in the detector control software `tvx` and studies of this effect in a silicon pixel detector.
- Geometrical measurements of the PILATUS 1M detector.
- Development of a distortion calibration program for the detector control software `tvx`.
- Analysis of the residual spatial distortion.
- Processing and analysis of protein crystallography data with XDS.

Outlook

The analysis of the PILATUS 1M performance provided critical information for the development of the next pixel detector system. This detector, the PILATUS 6M detector, is currently under construction and will have a similar architecture, but we have abandoned the idea of a shingled detector surface. The number of modules is extended to 5×12 modules, each with 487×195 pixels, leading to an active area of 424×435 mm^2 with 2463×2527 pixels (6.224 Mpixels). The insensitive area between the modules is reduced to 7 pixels within a bank and 17 pixels between adjacent banks. Between the readout chips the gap is now spanned by $1.5\times$–sized pixels; at the corners of 4 chips $2.25\times$–sized pixels are used. The readout chip of the new detector will be replaced by a significantly improved design of the PILATUS II chip. Using a 0.25 μm CMOS process permits a reduction of the pixel size to 172×172 μm together with a more dense and faster electronics. The counters are increased to 20 bits and a special logic prohibits counting errors. Measurements have shown that a pixel can count more than $1.5 \cdot 10^6$ γ/s/pixel without counting errors. However, a dead time correction will be required for high quality intensity measurements. The chips have been screened in large quantity and the yield of perfect chips is about 50 %.

Outstanding data quality should be achieved, because the defects of the prototype chip have been eliminated in the new readout chip. With an increased framing rate of $\sim$ 10 Hz, due to a reduced data transfer time, fine ϕ-sliced datasets can be recorded in the same time as conventional coarse ϕ-sliced datasets are currently collected with CCD detectors. Furthermore, the conventional datasets potentially can be collected in a few seconds in the continuous rotation mode, depending on the experimental conditions.

Appendix A

Variance of Convoluted Probabilities

The second moment of a probability distribution $f(x)$ is called the variance and is also equal to the square of the standard distribution σ and is

$$\mathrm{var}_f(x) = \sigma^2 = \int_{-\infty}^{+\infty} x^2 f(x) dx \,, \tag{A.1}$$

assuming a normalized function $f(x)$ with

$$\int_{-\infty}^{+\infty} f(x) dx = 1 \,. \tag{A.2}$$

For the convolution of two probability functions $f(x)$ and $g(x)$ the variance is

$$\mathrm{var}_{f\circ g}(x) = \int_{-\infty}^{+\infty} x^2 \left[\underbrace{\int_{-\infty}^{+\infty} f(u) \cdot g(u-x) du}_{f\circ g} \right] dx \,. \tag{A.3}$$

Interchanging the integration leads to

$$\mathrm{var}_{f\circ g}(x) = \int_{-\infty}^{+\infty} f(u) \left[\underbrace{\int_{-\infty}^{+\infty} x^2 g(u-x) dx}_{\star} \right] du \,. \tag{A.4}$$

The term ($\star$) can be rewritten by using the substitution $u - x = v$:

$$\begin{aligned} \int_{-\infty}^{+\infty} x^2 g(u-x) dx = \\ - \int_{-\infty}^{+\infty} \left(u^2 - 2vu + v^2 \right) g(v) dv = \\ -u^2 \underbrace{\int_{-\infty}^{+\infty} g(v) dv}_{=1} + 2u \underbrace{\int_{-\infty}^{+\infty} v g(v) dv}_{=<v>} - \int_{-\infty}^{+\infty} v^2 g(v) dv \,. \end{aligned}$$

For a symmetric distribution $g(v)$ the first moment $< v >$ is equal to zero. Therefore equation A.4 can be written as

$$\begin{aligned} \mathrm{var}_{f\circ g}(x) &= \int_{-\infty}^{+\infty} f(u)\left[u^2 + \int_{-\infty}^{+\infty} x^2 g(x)dx\right] du \\ &= \int_{-\infty}^{+\infty} u^2 f(u)du + \underbrace{\int_{-\infty}^{+\infty} f(u)du}_{=1} \cdot \int_{-\infty}^{+\infty} x^2 g(x)dx \; . \end{aligned} \tag{A.5}$$

The variance of the convolution probability $(f \circ g)$ is thus equal to the sum of the variances of the individual probability distributions $f(x)$ and $g(x)$:

$$\mathrm{var}_{f\circ g}(x) = \mathrm{var}_f + \mathrm{var}_g \; . \tag{A.6}$$

Appendix B

Abbreviations

Symbol	Description
ADC	Analog to Digital Converter
AIDS	Aquired Immune Deficiency Syndrome
AOUT	Analog Output
ASIC	Application Specific Integrated Circuit
BCB	Bank Control Board
BIT	Binary Digit
CAL	Internal calibration signal
CCD	Charge Coupled Device
CERN	Conseil Européen pour la Recherche Nucléaire (European Organisation for Nuclear Reasearch)
CHSEL	Chip Selection
CLK	Digital Clock
CMOS	Complementary Metal Oxide Semiconductor
CMS	Compact Muon Solenoid
COLSEL	Column Selection
COMP	Comparator
DAC	Digital to Analog Converter
DCB	Detector Control Board
DIN	Digital Input
DMILL	Durci Mixte Isolant Logico Linéaire
DNA	DeoxyriboNucleic Acid
DOUT	Digital Output
DPB	Detector Power Board
DQE	Detective Quantum Efficiency
EN	Enable Signal
FIFO	First In First Out
FWHM	Full Width at Half Maximum
HIV	Human Immunodeficiency Virus
JASRI	Japan Synchrotron Radiation Research Institute

Symbol	Description
LHC	Large Hadron Collider
LVDS	Low Voltage Differential Signalling
MAD	Multiple Wavelength Anomalous Dispersion
MCB	Module Control Board
MIR	Multiple Isomorphous Replacement
PAD	Pixel Array Detector
PCI	Peripheral Component Interconnect
PILATUS	PIxeL ApperaTUs for the Swiss Light Source
pixel	Picture Element
PSF	Point Spread Function
PSI	Paul Scherrer Institute
QE	Quantum Efficiency
ROWSEL	Row Selection
SAD	Single Wavelength Anomalous Dispersion
SLS	Swiss Light Source
SPring–8	Super Photon Ring, 8 GeV
UBM	Under Bump Metal
VME	VERSA–Module Europe
VPG	VME Pattern Generator
XDS	X–ray Detector Software

Appendix C

List of Symbols

Symbol	Description	Unit
$\vec{a}_i$	Lattice vector	
$\vec{a}_i^*$	Reciprocal lattice vector	
C	Capacitance	F
e	Elementray charge	C
E	Photon energy	keV
E_{gap}	Energy bandgap	eV
f_i^{atom}	Atomic form factor	
h, k, l	Miller indices	
I	Intensity	
$\vec{k}$	Wavevector	
N_a	Acceptor impurity density	cm^{-3}
N_d	Donor impurity density	cm^{-3}
Q	Charge	C
$\vec{Q}$	Scattering vector	
R_{cryst}	Reliability factor	
V	Voltage	V
V_0	Built in voltage	V
V_{bias}	Reversed bias voltage	V
Z	Atomic number	
ϵ_0	Permittivity in vacuum	F/cm
ϵ_r	Dielectric constant	
ϵ_s	Semiconductor permittivity	F/cm
θ	Scattering angle	rad
λ	Wavelength	Å
μ_e	Electron mobility	cm^2/Vs
μ_h	Hole mobility	cm^2/Vs
μ/ρ	Mass attenuation coefficient	cm^2/g

Symbol	Description	Unit
ρ	Material density	cm^{-3}
ρ_r	Material resistivity	$\Omega\mathrm{cm}$
ρ_t	Resolving time	s
$\rho(xyz)$	Electron density	cm^{-3}
σ	Standard deviation	
ϕ	Angular rotation	rad

Bibliography

[1] L. Stryer. *Biochemie*. Spektrum Verlag, Heidelberg, 1991.

[2] J. L. Sussman, D. Lin, J. Jiang, N. O. Manning, J. Prilusky, O. Ritter, and E. E. Abola. Protein Data Bank (PDB): Database of Three-Dimensional Structural Information of Biological Macromolecules. *Acta Crystallogr.*, D54:1078–1084, 1998.

[3] R. Lapatto, T. Blundell, A. Hemmings, J. Overington, A. Wilderspin, S. Wood, J. R. Merson, P. J. Whittle, D. E. Danley, K. F. Geoghegan, S. J. Hawrylik, S. E. Lee, K. G. Scheld, and P. M. Hobartet. X–ray analysis of HIV–1 proteinase at 2.7 Å resolution confirms structural homology among retroviral enzymes. *Nature*, 342:299–302, 1989.

[4] P. M. D. Fitzgerald and Springer J. P. Structure and Function of Retroviral Proteases. *Annu. Rev. Bioph. Biom.*, 20:299–320, 1991.

[5] J. R. Plaisier, R. I. Koning, H. K. Koerten, A. M. van Roon, E. A. J. Thomassen, M. E. Kuil, J. Hendrix, C. Brönnimann, N. S Pannu, and J. P. Abrahams. Area detectors in structural biology. *Nucl. Instrum. Meth. A*, 509:274–283, 2003.

[6] C. Gemme. The ATLAS pixel detector. *Nucl. Instrum. Meth. A*, 501(1):87–92, 2003.

[7] S. Schnetzer. The CMS pixel detector. *Nucl. Instrum. Meth. A*, 501(1):100–105, 2003.

[8] J. Drenth. *Principles of Protein X–ray Crystallography*. Springer Verlag, Berlin, 1994.

[9] R. Zhao, D. C. Pevear, M. J. Kremer, V. L. Giranda, J. A. Kofron, R. J. Kuhn, and M. G. Rossmann. Human rhinovirus 3 at 3.0 Å resolution. *Structure*, 4:1205–1220, 1996.

[10] E. Arnold and M. G. Rossmann. The use of molecular- Structures determined by electron microscopy place replacement phases for the refinement of the human rhinovirus 14 structure. *Acta Crystallogr.*, A44:270–282, 1988.

[11] T. C. Appleby, H. Luecke, J. H. Shim, J. Z. Wu, W. Cheney, W. Zhong, L. Vogeley, Z. Hong, and N. Yao. Crystal Structure of Complete Rhinovirus RNA Polymerase Suggests Front Loading of Protein Primer. *J. Virol.*, 79:277–288, 2005.

[12] C. Giacovazzo. *Fundamentals of Crystallography*. Oxford University Press, Oxford, 2002.

[13] T. Hahn. *International Tables For Crystallography A*. Kluwer Academic Puplishers, Boston, 1996.

[14] A. Schmidt, A. Gonzalez, R. J. Morris, M. Costabel, P. M. Alzarib, and V. S. Lamzina. Advantages of high-resolution phasing: MAD to atomic resolution. *Acta Crystallogr.*, D58:1433–1441, 2002.

[15] Z. Dauter, M. Dauter, and E. Dodson. Jolly SAD. *Acta Crystallogr.*, D58:494–506, 2002.

[16] M. J. Renzi, M. W. Tate, A. Ercan, S. M. Gruner, E. Fontes, C. F. Powell, A. G. MacPhee, S. Narayanan, J. Wang, Y. Yue, and R. Cuenca. Pixel array detectors for time resolved radiography. *Rev. Sci. Instrum.*, 73(3):1621–1624, 2002.

[17] G. Rossi, M. Renzi, E. F. Eikenberry, M. W. Tate, D. Bilderback, E. Fontes, R. Wixted, S. Barna, and S. M. Gruner. Tests of a prototype pixel array detector for microsecond timeresolved X–ray diffraction. *J. Synchrotron Radiat.*, 6:1096–1105, 1999.

[18] C. Ponchut, J. L. Visschers, A. Fornaini, H. Graafsma, M. Maiorino, G. Mettivier, and D. Calvet. Evaluation of a photon-counting hybrid pixel detector array with a synchrotron X–ray source. *Nucl. Instrum. Meth. A*, 484:396 406, 2002.

[19] C. Ponchut and F. Zontone. Evaluation of medipix-1 in X-ray scattering and X-ray diffraction applications. *Nucl. Instrum. Meth. A*, 510:29–34, 2003.

[20] G. T. Reynolds, J. R. Milch, and S. M. Gruner. High sensitivity image intensifier–TV detector for x–ray diffraction studies. *Rev. Sci. Instrum.*, 49:1241–1249, 1978.

[21] D. J. Thiel, R. L. Walter, S. E. Ealick, D. H. Bilderback, M. W. Tate, S. M. Gruner, and E. F. Eikenberry. Marcomolecular crystallographic result obtained at CHESS using a detector incorporating a charge–coupled device. *Rev. Sci. Instrum.*, 66(2):1477–1479, 1995.

[22] S. M. Gruner, M. W. Tate, and E. F. Eikenberry. CCD Area X–ray Detectors. *Rev. Sci. Instrum.*, 73:2815–2842, 2002.

[23] M. W. Tate, E. F. Eikenberry, S. L. Barna, M. E. Wall, J. L. Lowrance, and S. M. Gruner. A Large–Format High–Resolution Area X–ray Detector Based on a Fiber–Optically Bonded Charge–Coupled Device (CCD). *J. Appl. Crystallogr.*, 28:196–205, 1995.

[24] G. Lutz. *Semiconductor Radiation Detectors*. Springer Verlag, Berlin, 1997.

[25] M. S. Sze. *Semiconductor devices, physics and technology*. John Wiley and Sons, New York, 1985.

[26] C. A. Klein. Bandgap Dependence and Related Features of Radiation Ionization Energies in Semiconductors. *J. Appl. Crystallogr.*, 39(4):2029–2038, 1968.

[27] H. Nakatani, E. Sakai, C. Tatsuyama, and F. Takeda. GaSe nuclear particle detectors. *Nucl. Instrum. Meth. A*, 283(2):303–309, 1989.

[28] H. J. Fitting. Transmission, energy distribution, and SE [secondary electron] excitation of fast electrons in thin solid films. *Phys. Status Solidi A*, 26(2):525–535, 1974.

[29] M. Mikulec. *Single Photon Detection with Semiconductor Pixel Arrays for Medical Imaging Applications.* PhD dissertation, University of Vienna, Vienna, Austria, 2000. Cern-Thesis-2000-021.

[30] R. D. Evans. *The Atomic Nucleus.* MacGraw–Hill Book Company, New York, 1955.

[31] Ch. Brönnimann, S. Florin, M. Lindner, B. Schmitt, and C. Schulze-Briese. Synchrotron beam test with a photon–counting pixel detector. *J. Synchrotron Radiat.*, 7:301–306, 2000.

[32] Ch. Broennimann, E. F. Eikenberry, B. Henrich, R. Horisberger, G. Hülsen, E. Pohl, B. Schmitt, C. Schulze-Briese, M. Suzuki, T. Tomizaki, H. Toyokawa, and A. Wagner. The PILATUS 1M detector. *J. Synchrotron Radiat.*, 2005. in press.

[33] G. Hülsen, E. F. Eikenberry, R. Horisberger, B. Schmitt, C. Schulze-Briese, T. Tomizaki, H. Toyokawa, M. Stampanoni, G. L. Borchert, P. Willmot, B. Patterson, and Ch. Brönnimann. Pixel Detectors For Diffraction Experiments At The Swiss Light Source. *AIP Conference Proceedings*, 705:1009–1012, 2004.

[34] S. Kohout. Messungen am Auslesechip für den PILATUS Detektor. Diploma thesis, Universität Zürich, Zürich, Switzerland, 2001.

[35] S. L. Barna, E. F. Eikenberry, S. M. Gruner, and M. W. Tate. Calibration procedures for charge–coupled device x–ray detectors. *Rev. Sci. Instrum.*, 70(7):2927–2933, 1999.

[36] I. N. Bronstein and K. A. Semendjajew. *Taschenbuch der Mathematik.* B.G. Teubner Verlagsgesellschaft, Stuttgart, 1991.

List of Figures

2.1 The three dimensional structure of the protein thaumatin 7
2.2 Light Microscope and X–ray crystallography 8
2.3 The crystal lattice 10
2.4 The Bragg law 10
2.5 The Ewald sphere 13
2.6 The unit cell structure factor F_{hkl} 14
2.7 Building blocks of a CCD detector 18
2.8 Schematic cross section through a phosphor screen 18
2.9 Schematic of a CCD chip 20
2.10 Building blocks of a hybrid pixel area detector 21
2.11 Attenuation length for typical semiconductor sensors 23
2.12 Schematic cross section through a silicon pixel sensor 26
2.13 Absorption capability for semiconductors 27
2.14 Architecture of the CMOS chip 28
2.15 Rate dependency of counting detectors 30

3.1 The PILATUS 1M detector 35
3.2 The fundamental unit of the PILATUS 1M detector is a module 37
3.3 The silicon assembly on the top of each module 37
3.4 The p–side of the silicon sensor 38
3.5 The SLS06 (PILATUS I) CMOS chip 40
3.6 A six inch wafer with 66 CMOS chips. 42
3.7 Wire bond connections from the MCB to the CMOS chips 42
3.8 The closed PILATUS 1M detector 43
3.9 Oscilloscope reading from the read–out cycle 45
3.10 Block diagram of the control architecture of the detector 45
3.11 The open PILATUS 1M detector viewed from different side 47

4.1 The histogram of the threshold values of the PILATUS 1M detector 50
4.2 The experimental setup for flatfield calibration 51
4.3 Calculation of the theoretical flatfield response 53
4.4 A flatfield raw image 55
4.5 A histogram of an exposured image before and after flatfield correction 56

5.1 Variance of flatfield images 60
5.2 Histogram of counting errors observed in flatfield images 61

5.3 Defect Reduction using a detector translation 62
5.4 Profiles of Bragg reflections in the detector plane 64
5.5 ϕ–profiles of Bragg reflections recorded with the PILATUS 1M detector 65
5.6 A diffraction image recorded with the PILATUS 1M detector 66

List of Tables

2.1 Efficiency of fiber optic tapers depend on the magnification [22]. 19
2.2 Electronic properties of semiconductors 23
2.3 Specifications of a CCD and a PAD 33

4.1 Standard deviations of the untrimmed and trimmed detector 50

Curriculum Vitae

Name:	Gregor Stefan Hülsen–Bollier Pfarrhaus 7278 Davos Monstein/Switzerland
Birth:	16.04.1971 Augsburg
Nationality:	German
	married since 9.Juli 2004 with Claudia Bollier

Academic background:

Ph.D thesis 2001-2005	Synchrotron Radiation Research Department, Paul Scherrer Institut (ETH-Zurich), Switzerland
Diploma thesis 2000-2001	Institut of Biomedical Engineering, University of Erlangen–Nürnberg, Germany
Project assistant 1999 1998	Synchrotron Radiation Research Department, Detector Development, PSI, Switzerland Institut of Biomedical Engineering, University of Erlangen–Nürnberg, Germany
Diploma studies 1995-2001 1997-1998	Friedrich–Alexander–University of Erlangen, Germany (Physics) University of St Andrews, Scotland
University–entrance diploma 1993-1995	Städtische Berufsoberschule Augsburg, Germany
Civilian service 1987-1991	Deutsches Herzzentrum München, Germany
Apprenticeship 1987-1991	Electronics installer - Deutsche Bundesbahn, Germany
School	
1983 - 1987	Staatliche Realschule Friedberg, Germany
1977 - 1983	Grund und Teilhauptschule Ottmaring, Germany

List of Publications

- Protein Crystallography with the PILATUS 1M Detector. **G. Hülsen**, Ch. Brönnimann, E. F. Eikenberry, A. Wagner. *J. Appl. Crystallogr.*, in preparation.
- Distortion Calibration of the PILATUS 1M Detector. **G. Hülsen**, Ch. Brönnimann, E. F. Eikenberry. *Nucl. Instrum. Meth. A*, 548, 540-554.
- The PILATUS 1M Detector. Ch. Broennimann, E. F. Eikenberry, B. Hennrich, R. Horisberger, **G. Hülsen**, E. Pohl, B. Schmitt, C. Schulze-Briese, M. Suzuki, T. Tomizaki, H. Toyokawa, A. Wagner. *J. Synchrotron Radiat.*, in press.
- In situ studies of complex PLD–grown films using hard X–ray surface diffraction. P. R. Willmott, C.M. Schlepütz, B. D. Patterson, R. Herger, M. Lange, D. Meister, D. Maden, Ch. Brönnimann, E. F. Eikenberry, **G. Hülsen**, A. Al-Adwan. *Appl. Surf. Sci.*, 247, 188-196, 2005.
- Improved data acquisition in grazing-incidence x–ray scattering experiments using a pixel detector. C. M. Schlepütz, R. Herger, P. R. Willmott, B. D. Patterson, O. Bunk, Ch. Brönnimann, B. Henrich, **G. Hülsen**, E. F. Eikenberry. *Acta Crystallogr.*, A61, 418-425, 2005.
- Pixel detectors for diffraction experiments at the Swiss Light Source. **G. Hülsen**, E. F. Eikenberry, R. Horisberger, B. Schmitt, C. Schulze-Briese, T. Tomizaki, H. Toyokawa, M. Stampanoni, G. L. Borchert, P. Willmott, B. Patterson, Ch. Brönnimann. *AIP Conference Proceedings*, 705, 1009-1012, 2004.
- First experiments with the PILATUS 1M detector. **G. Hülsen**, Ch. Brönnimann, Ch. Bühler, E. F. Eikenberry, F. Glaus, R. Horisberger, M. Naef, H. Rickert, B. Schmitt, S. Streuli, C. Schulze-Briese, T. Tomizaki, A. Wagner. *PSI Scientific Report*, 7, 2003.
- Continuous sample rotation data collection for protein crystallography with the PILATUS detector. E. F. Eikenberry, Ch. Brönnimann, **G. Hülsen**, H. Toyokawa, R. Horisberger, B. Schmitt, C. Schulze-Briese, T. Tomizaki. *Nucl. Instrum. Meth. A*, 501, 260-266, 2003.
- Die Aktivierung von Prothrombin und Fribrinogen an Zinndioxid durch Elektronen–transferprozesse (The activation of pro–thrombin and fibrinogen on tin–dioxide by electron transfer processes). **G. Hülsen**. *Diploma thesis*, University of Erlangen, Germany, 2001.
- Analyse der Korrelation zwischen Fibrinbildung an Biomaterialen und Elektronentransferprozessen (Analyze of the correlation between fibrin formations on biomaterials and electron transfer processes). **G. Hülsen**, A. Rzany, M. Schaldach. *Proceedings to the 34th meeting of the German, Austrian and Swiss association for biomedical technique*, Lübeck, Germany, 2000.

Acknowledgments

On this point I would like to give credit to all, who supported me in succeeding this work. Special thanks go to

Prof. Dr. F. Winkler and Prof. Dr. R. Eichler for giving me the opportunity for this thesis. I am very thankful for their support and guidance during my thesis.

Dr. C. Brönnimann for his excellent supervision, all the discussions and helpfulness as well as the freedom which he gave me in arranging my work in his group.

Dr. E. F. Eikenberry's enthusiasm was very encouraging. His expert knowledge in detector development and the discussions with him were of great help. The tips and tricks box of how to program detector control and analyze software opened always at the right time.

M. Naef for the development of the electronic circuit boards and his assistance in setting up the detector system; S. Streuli for the construction of the detector mechanic and H. Rickert for his help in the assembly of the detector modules; F. Glaus for all his essential work for the bump bonding performed in the clean room of PSI. Thanks that they all gave their expertise into the fabrication of the detector system.

Dr. C. Schulze–Briese, Dr. T. Tomizaki, C. Pradervand and Dr. A. Wagner for their help in the experimental time at the protein crystallography beamline X06SA of the SLS. Their knowledge and experience was of high importance for this work.

Dr. W. Kabsch for his discussions and help in processing our data with XDS. Without his adaptations of this processing software the detailed analyzes could not be performed.

I very much enjoyed all the discussions, meetings and work at PSI and SPring–8 with our Japanese collaborators Dr. M. Suzuki and Dr. H. Toyokawa.

The Swiss National Science Foundation and the Paul Scherrer Institute financially supported this work. This gave me the opportunity to realize the scientific work of this thesis and the presentation of the results at the Synchrotron Radiation Instrumentation Conference 2005 in San Francisco and at the Japan Synchrotron Radiation Research Institute (SPring–8).

Finally I would like to thank my parents and my wife Mrs C. Bollier Hülsen for the support and concern in my work. Without them this work would not have been realized.